CAPITAL UNIVERSITY OF SCIENCE AND TECHNOLOGY, ISLAMABAD

Magnetohydrodynamic Bio-convective Radiative Flow of Casson and Williamson Nanofluids over a Stretching Surface with Thompson-Troian Slip Conditions

by

Maria Safdar

A thesis submitted in partial fulfillment for the degree of Master of Philosophy

in the

Faculty of Computing
Department of Mathematics

2026

CERTIFICATE OF APPROVAL

Magnetohydrodynamic Bio-convective Radiative Flow of Casson and Williamson Nanofluids over a Stretching Surface with Thompson-Troian Slip Conditions

by

Maria Safdar

(MMT231005)

THESIS EXAMINING COMMITTEE

S No	Examiner	Name	Organization
(a)	External Examiner	Dr. Saqib Zia	CUI, Islamabad
(b)	Internal Examiner	Dr. A. Rehman Kahsif	CUST, Islamabad

Dr. Muhammad Sagheer
Thesis Supervisor
April, 2026

Dr. Muhammad Sagheer
Head
Department of Mathematics
April, 2026

Dr. M. Abdul Qadir
Dean
Faculty of Computing
April, 2026

Author's Declaration

I, **Maria safdar** hereby state that my MPhil thesis titled "**Magnetohydrodynamic Bio-convective Radiative Flow of Casson and Williamson Nano fluids over a Stretching Surface with Thompson-Troian Slip Conditions**" is my own work and has not been submitted previously by me for taking any degree from Capital University of Science and Technology, Islamabad or anywhere else in the country/abroad.

At any time if my statement is found to be incorrect even after my graduation, the University has the right to withdraw my MPhil Degree.

Maria Safdar

Registration No: MMT231005

Plagiarism Undertaking

I solemnly declare that research work presented in this thesis titled "**Magneto-hydrodynamic Bio-convective Radiative Flow of Casson and Williamson Nanofluids over a Stretching Surface with Thompson-Troian Slip Conditions**" is solely my research work with no significant contribution from any other person. Small contribution/help wherever taken has been duly acknowledged and that complete thesis has been written by me.

I understand the zero tolerance policy of the HEC and Capital University of Science and Technology towards plagiarism. Therefore, I as an author of the above titled thesis declare that no portion of my thesis has been plagiarized and any material used as reference is properly referred/cited.

I undertake that if I am found guilty of any formal plagiarism in the above titled thesis even after award of MPhil Degree, the University reserves the right to withdraw/revoke my MPhil degree and that HEC and the University have the right to publish my name on the HEC/University website on which names of students are placed who submitted plagiarized work.

Maria Safdar

Registration No: MMT231005

Acknowledgement

I would like to express my deepest gratitude and appreciation to all those who have contributed to the successful completion of this thesis.

I am profoundly thankful to my supervisor, Dr. Muhammad Sagheer, for his unwavering support and guidance throughout my research. His expertise and valuable insights have been essential in steering this work and enhancing its quality.

I would like to express my sincere gratitude to my respected teachers for their continuous guidance, encouragement, and valuable feedback throughout the course of my research. Their support and insightful suggestions have been instrumental in the successful completion of this thesis.

I am deeply grateful to Mr. Hassan Shahzad for his kind assistance, motivation, and cooperation throughout my thesis work. His constant encouragement and valuable support have been a true source of inspiration for me.

I am profoundly thankful to my parents and siblings for their unwavering love, encouragement, and belief in me. Their constant support and understanding have provided me with strength during the challenging moments of my academic journey. Their sacrifices and motivating words have kept me focused and driven.

A special note of thanks goes to my father, whose boundless love, encouragement, and sacrifices have been the bedrock of my academic journey. His unwavering belief in me has been a driving force behind my achievements, and I am forever grateful for his guidance and wisdom.

In conclusion, this thesis would not have been possible without the collective efforts of all those mentioned above.

Abstract

This research provides a detailed analysis of Williamson nanofluids and Casson fluids under the influence of multiple parameters. The study investigates unsteady flow and heat transfer over a stretching sheet, accounting for Joule heating, thermal radiation, and internal heat generation. Williamson nanofluid behavior is analyzed with viscoelastic and shear-thinning effects, while Casson fluid is studied both over a stretching sheet and within a porous medium to examine yield-stress and non-Newtonian characteristics. The governing equations for both fluids are solved using the shooting method applied to the resulting coupled ordinary differential equations. The results show that an increase in the Casson parameter β, decreases the skin friction by 28.6%, while the heat source parameter He, enhances the heat transfer rate by up to 27.3%. Thermal radiation and internal heat generation are observed to elevate the temperature field, whereas the Eckert number further intensifies heat production through viscous dissipation. The Lorentz force, in contrast, reduces the flow velocity. Overall, the investigation demonstrates that the flow and transport behavior of Williamson nanofluids and Casson fluids is strongly governed by the combined effects of thermal, viscous, slip, and porous medium parameters.

Contents

List of Figures

List of Tables

Abbreviations

BCs	Boundary conditions
IVPs	Initial value problem
MHD	Magnetohydrodynamics
ODEs	Ordinary differential equation
PDEs	Partial differential equation
RK-4	Range kutta method of order 4
WNF	Williamson Nano Fluid

Symbols

u, v	Velocity components
μ	Viscosity
ν	Kinematic viscosity
ρ	Nanofluid density
B_0	Magnetic field strenght
Wi	Williamson parameter
α	Thermal diffusivity
T	Temperature
T_∞	Ambient temperature
T_w	Wall temperature
γ	Angle of inclination
C	Concentration
C_∞	Ambient concentration
C_w	Concentration at wall
M	Magnetic field parameter
Pe	Peclet number
Nu_x	Nusselt number
Pr	Prandtl number
Nn_x	Motile density number
Cf_x	Skin friction coefficient
Sh_x	Sherwood number
Re_x	Reynold number
u_w	Velocity of stretching sheet

Sc	Schmidt number
Sb	Bioconvection schmidt number
Nt	Thermophoresis parameter
Nb	Brownian motion parameter
D_B	Brownian motion diffusivity
D_s	Diffusivity of microorganism
D_T	Thermophoresis diffusivity
H_e	Heat generation parameter
N_R	Radiation parameter
B_i	Biot number
S	Porous medium parameter
β	Casson parameter
ϵ	Unsteady parameter

Chapter 1

Introduction

Fluid flow is central to many natural and industrial processes, including chemical reactors, heat exchangers, and biomedical systems.Although Newtonian fluids exhibit a linear relationship between shear rate and shear stress, many real-world fluids display non-Newtonian behavior, in which this relationship is nonlinear.

Among non-Newtonian fluids, the Williamson fluids exhibit shear-thinning behavior, commonly observed in polymer solutions and lubricants, whereas the Casson model describes fluids with a yield stress, such as blood and printing inks. These fluids are often influenced by magnetic fields, porous media, nanoparticle transport, and bio-convection due to motile microorganisms. The novelty of this thesis lies in investigating unsteady Williamson and Casson fluid flows over stretching sheets, including magnetic field effects, porous medium, and bio-convection, providing new insights into their combined impact on flow, energy, and mass transfer.

1.1 Background

The Williamson fluid flow model is a well-known non-Newtonian fluid model that was introduced by Williamson in 1929 [1]. The Williamson model explains the motion of viscoelastic fluids, which display a mix of both viscous and elastic properties. In this model, the stress is represented as a function of the strain rate

together with the fluid's relaxation time, allowing it to capture the dual nature of such fluids. Because of this, the Williamson formulation is considered appropriate for analyzing materials that cannot be described by purely Newtonian models.

Since its development, this model has been widely explored and applied across many areas of science and engineering for better understanding of complex fluid behavior. Salahuddin et al. [2] investigated the behavior of Williamson fluid model under the joint influence of thermal radiation, activation energy and viscous dissipation within sinusoidal walls, where solutions are obtained using the Dsolve command in Mathematica and validated through a perturbation approach. Shashikumar et al. [3] examined the steady flow of Williamson fluid in a microchannel under the combined effects of viscous dissipation, Joule heating, and magnetic influence, with the governing equations solved by using the finite element method. Kho et al. [4] The behavior of Williamson nanofluid flow over a stretching sheet was examined numerically, incorporating thermal and velocity slip conditions within the framework of the Buongiorno model, and solved the problem by using the shooting method. Hamid et al. [5] carried out a numerical analysis of the unsteady MHD flow of WNF through a permeable channel in the existence4 of a heat source considering buoyancy and thermal radiation effects and solved the governing equation by applying the Crank–Nicolson finite difference scheme. On the Williamson fluid model several researchers have conducted comprehensive reviews, including studies by Bibi et al. [6], Kumar et al. [7], Al-Arabi et al. [8] and Supriya and Pullepu. [9].

The concept of the Casson fluid was introduced by G. Casson in 1959 [10] to describe the flow behavior of certain complex fluids that do not obey Newton's law of viscosity. These fluids, such as blood, inks, and suspensions, exhibit a yield stress, meaning they behave like a solid at very low stresses and start to flow only when a critical stress is exceeded.Once the fluid begins to flow, it exhibits shear-thinning behavior characterized by a reduction in apparent viscosity as the shear rate increases. The Casson model effectively captures the non-Newtonian characteristics of fluids with suspended particles or high viscosity at low shear rates, making it highly useful in both scientific research and industrial applications. Over the

years, it has been applied extensively in biomedical engineering to model blood flow, in industrial processes like printing inks and polymer solutions, and in food technology for materials such as chocolate, ketchup, and pastes. Researchers have further expanded the model to include heat and mass transfer, magnetic effects, porous media, and chemical reactions, allowing for the study of more realistic and complex fluid systems.

The simplicity and versatility of the Casson model have made it a standard choice for analyzing non-Newtonian flows, providing a better understanding of the behavior of fluids that are otherwise difficult to describe using classical Newtonian theory. Oyelakin et al. [11] examined the flow of a Casson nanofluid over an unsteady stretching sheet, considering Dufour and Soret effects on heat and mass transfer. It examined the contribution of partial slip, thermal radiation, heat generation, and nanoparticle diffusion on velocity, temperature, and concentration. The governing equations were solved employing the spectral relaxation method, providing insight into how these factors affect the fluid's transport behavior. Hamid at el. [12] investigated dual solutions for the MHD flow and heat transfer of Casson fluid over a stretching sheet, considering linear thermal radiation and a uniform magnetic field. The governing PDEs reduced to nonlinear ODEs and solved using Maple 2015. Results show that the dual solutions are stable, with upper branch solutions and positive eigenvalues providing more stable flow profiles than lower branch solutions. Das et al. [13] explored the flow, heat, and mass transfer of an unsteady Casson fluid over a stretching surface embedded in a porous medium, considering thermal radiation, variable heat absorption, chemical reaction, Soret effect, and a variable magnetic field. Velocity slip and conjugate heating boundary conditions are also incorporated. The resulting system of ODEs is solved numerically through the shooting method in conjunction with the fourth-order Runge–Kutta scheme.

Reza-E-Rabbi et al. [14] focused on mass and heat transfer in the flow of a Casson nanofluid over a stretching sheet, considering magnetohydrodynamic (MHD) effects, thermal radiation, chemical reactions, Brownian motion, and thermophoresis. Using boundary layer approximations, the governing equations for momentum, energy, and concentration are formulated. The equations are solved numerically

using an explicit finite difference method, and a Compaq Visual Fortran 6.6.a program was developed to simulate the fluid flow system and obtain results. Faraz et al. [15] the study examines how thermo-diffusion, multi-slip and chemical reaction influence the unsteady axisymmetric flow of a Casson fluid over a radially stretching sheet with time-dependent velocity. Appropriate similarity transformations are employed to reduce the governing nonlinear partial differential equations to ordinary differential equations.

The system is solved numerically using the Keller-Box implicit finite difference method, which provides high accuracy and reliability even for simulations over very short time intervals. Srinivasacharya et al. [16] analyzed the Dufour and Soret effects on Casson fluid flow over an unsteady radially stretching sheet. The governing equations are transformed into nonlinear ODEs and solved using a multilayer perceptron neural network optimized with the ADAMS algorithm. The ANN method provides high accuracy, and results for skin friction and heat transfer closely matching those from the Runge-Kutta method. Extensive reviews on the Casson fluid model have been carried out by several researchers, including the work of Abdel-Gawad [17], Ahmed Megahed [18], Raju et al. [19] and Rehman et al. [20].

The function of radiation in fluid flow and heat transfer is particularly important in high-temperature fields such as space technology. Magnetic fields interacting with electrically conducting fluids often give rise to radiative flows observed in electrical power generation, solar technologies, astrophysical systems, nuclear reactors, and other industrial processes. Previous studies have explored viscous as well as non-Newtonian fluids in connection with thermal radiation effects. For instance Kumar et al. [21] investigated two-phase boundary layer flow and associated heat transfer of a Williamson fluid containing suspended particles past a stretching sheet, with numerical solutions obtained through the Runge-Kutta-Fehlberg (RKF45) scheme. Hayat et al. [22] focuses on unsteady two-dimensional boundary layer flow of an incompressible Williamson fluid across a time-dependent permeable stretching surface under the influence of thermal radiation. Megahed [23] study examines the impact of thermal radiation and viscous dissipation on the boundary layer flow

and heat transfer of Williamson fluid over a nonlinearly stretching sheet. Hashim et al. [24] explored a three-dimensional unsteady flow of Williamson nanofluid under the combined influence of thermal radiation and magnetic effects. Rashidi et al. [25] conduct a detailed analysis of MHD mixed convection heat transfer of an incompressible, laminar, electrically conducting viscoelastic fluid over a permeable wedge in the presence of thermal radiation. Balogun et al. [26] investigated MHD behavior of hybrid nanofluids past a stretching sheet influenced by thermal radiation and magnetic field, and applied the MATLAB's bvp4c solver for the numerical solution.

The study of motile microorganisms has gained considerable attention due to their important role in bio-convective fluid flows. Motile microorganisms, such as certain types of algae and bacteria, have the natural ability to swim and move actively in fluid environments. Their motion helps to stabilize the nanofluid suspensions by preventing nanoparticle sedimentation, thereby improving the uniformity of the fluid mixture. In fluid flow models, the presence of motile microorganisms introduces an additional parameter that influences both the mass transport and stability of the system. This concept is widely applied in biotechnology, bioengineering, and environmental sciences, where microorganism activity directly affects processes like nutrient transport, wastewater treatment, and microbial fuel production.

Waqas et al. [27] presented a dynamical analysis of bioconvection in a Jeffrey nanofluid with gyrotactic motile microorganisms over a stretching sheet, influenced by a magnetic dipole and ferromagnetic particles, with numerical solutions obtained using the bvp4c solver in MATLAB. Farooq and Imran [28] worked on the outcome of activation energy and thermal radiation, along with bioconvection and motile microorganisms, on the flow of Casson hybrid nanofluid past a cylinder. The governing equations are analyzed numerically in MATLAB through the bvp4c solver along with the shooting method. Moatimid et al. [29] focused on the non-Newtonian Williamson magnetohydrodynamic (MHD) pulsatile flow of an incompressible nanofluid in the availability of motile microorganisms, within a porous medium confined between two permeable vertical walls. Algehyne and

Saeed [30] examined the bioconvective MHD flow of Williamson nanofluid over a slender stretching surface and examined the numerical results, validated by comparison with the MATLAB bvp4c solver. Nadeem et al. [31] investigated the influence of chemical reaction and bioconvection on the heat transfer characteristics of magnetohydrodynamic Williamson hybrid nanofluid flow over a stretched surface. Muhammad et al. [32] explored a Jeffrey nanofluid flow with motile microorganisms and activation energy over a sheet, and verified the findings through MATLAB's bvp4c function.

Velocity slip describes the relative motion of fluid at the wall, while the thermal slip accounts for a temperature difference between the surface and adjacent fluid layers. Slip conditions are introduced to allow a finite velocity or temperature jump at the boundary surface. These conditions play an essential role in accurately modeling the modern fluid flow problems, where the surface roughness, rarefied gases, and nanofluids exhibit deviations from the classical no-slip behavior.

Gangadhar et al. [33] discussed the impact of Thomson and Troian boundary conditions on Williamson nanofluid flow over a porous stretchable surface with numerical solutions obtained through MATLAB's bvp4c solver.
Amanulla et al. [34] Perform a numerical investigation of two-dimensional MHD Williamson fluid flow along a vertical convective surface, considering the impact of slip boundary conditions. Nagendra et al. [35] examined a mathematical model to investigate the magnetohydrodynamic flow and heat transfer of an electro-conductive polymer over the external surface of a sphere subjected to a radial magnetic field, incorporating the effects of slip parameters in the analysis and graphical results. Ramzan et al. [36] investigated mass and heat transfer in the free convection flow of a Brinkman fluid over a plate within the porous media, incorporating slip effects and chemical reactions to present a more realistic flow scenario. Abbas [37] studied MHD flow of a hybrid nanofluid past an exponentially stretching sheet under the influence of Joule heating and slip boundary conditions, using the spectral collocation method based on Legendre wavelets. Previous studies on Williamson nanofluids and Casson fluids have primarily examined selected aspects of their flow and heat transfer characteristics. The current study extends

the existing research by simultaneously considering multiple governing parameters, thereby providing a more comprehensive understanding of the complex behavior of Williamson nanofluids, characterized by viscoelastic and shear-thinning effects, and Casson fluids, which exhibit non-Newtonian yield-stress behavior. The investigation is formulated to reflect realistic physical conditions relevant to engineering and industrial flow systems. To tackle the strongly nonlinear governing equations, the study employs a numerical approach combining the shooting method combined with the fourth-order Runge–Kutta scheme. This method enables detailed analysis of concentration, velocity, temperature, and motile density distributions, while incorporating the effects of magnetic fields, slip conditions, thermal radiation, internal heat generation, Brownian motion, and thermophoresis.

A comparative evaluation of Williamson and Casson fluids under identical conditions highlights the impact of unsteadiness and boundary-layer development. Heat and mass transfer performance is quantified using Nusselt number, Sherwood number, and skin-friction coefficient, with results presented graphically and numerically for practical engineering insight. Building on these findings, the study addresses the following research questions:

i) How do Williamson and Casson fluids behave differently over a stretching sheet in terms of temperature, velocity, and concentration profiles?

ii) What is the effect of incorporating a porous medium on the flow and transport characteristics of Casson fluid?

iii) How do magnetic field intensity and slip parameters influence the boundary-layer development for both fluids?

iv) How does unsteadiness affect velocity, temperature, and concentration distributions in Williamson and Casson fluids?

v) How does the Casson parameter influence the yield-stress behavior and flow characteristics in porous vs non-porous configurations?

1.2 Thesis Structure

1.2.1 Chapter 2

In this chapter, an analytical study is conducted on Williamson nanofluid flow past a stretching sheet by incorporating Thompson and Troian slip conditions. To resolve the governing nonlinear equations of the flow model, the shooting method in combination with numerical integration is employed, ensuring accurate and reliable results.

1.2.2 Chapter 3

Chapter 3 extends the flow model presented in Chapter 2 by considering the effects of unsteady flow, thermal radiation and internal heat generation. Numerical solutions of the governing equations are acquired through the application of the shooting method.

1.2.3 Chapter 4

The analysis is extended by replacing the Williamson nanofluid with a Casson fluid in a porous medium, incorporating the effects of unsteady flow, thermal radiation, and internal heat generation. The governing equations for the Casson fluid are solved numerically using the shooting method, providing detailed insights into velocity, temperature, and concentration profiles under these additional physical influences.

1.2.4 Chapter 5

Chapter 5 presents the conclusions of the thesis, highlighting the key findings and major contributions of the study.

Chapter 2

Numerical Simulation of Williamson Fluid with Motile Microorganisms and Slip Effects Over a Stretched Sheet

2.1 General Introduction

In this chapter, we discuss the numerical analysis of Williamson nanofluid flow past a stretching sheet. The model incorporates the stabilization of nanoparticles by gyrotactic microorganisms and accounts for the impact of bioconvection, thermophoresis and Brownian motion. The governing nonlinear PDEs are converted into a system of dimensionless ODEs using suitable transformations.

The numerical solution of ODEs is obtained by applying shooting method in MATLAB. At the end of this chapter, the numerical solution for different parameters is analyzed for the dimensionless velocity $f'(\eta)$, concentration distribution $\phi(\eta)$, motile distribution $X(\eta)$ and temperature distribution $\theta(\eta)$. Evaluation of the calculated results are given through tables and graphs. This chapter delivers a detailed review of the work previously performed by Xin et al. [38]

2.2 Physical Model

In the present chapter, an investigation of the 2D flow characteristics of a Williamson nanofluids past a horizontal sheet. The coordinate axis along the stretched sheet is denoted by x and that perpendicular to the sheet is y. Suppose that the sheet has been stretched with velocity $U_w = ax$. Nanoparticles are stabilized by gyrotactic microorganisms, creating bioconvection. The model also includes Brownian motion and thermophoresis of nanoparticles. The sheet has higher temperature, concentration, and microorganism density than the surrounding fluid. The steady flow of Williamson fluid is described by the following equations (2.1)-(2.5) together with the associated boundary conditions (2.6).

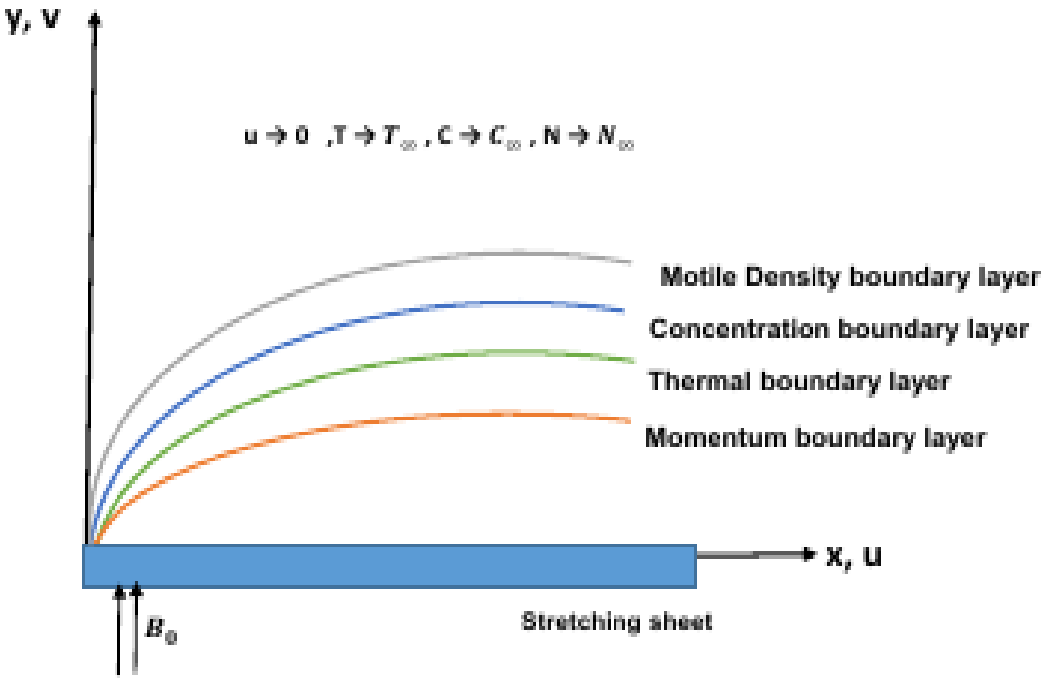

FIGURE 2.1: Methodical Presentation of the system

$$\frac{\partial u}{\partial x} + \frac{\partial v}{\partial y} = 0, \tag{2.1}$$

$$u\frac{\partial u}{\partial x} + v\frac{\partial u}{\partial y} + \frac{\sigma B_o^2}{\rho}u = \nu\left[1 + \sqrt{2}\Gamma\frac{\partial u}{\partial y}\right]\frac{\partial^2 u}{\partial y^2}, \tag{2.2}$$

$$v\frac{\partial T}{\partial y}+u\frac{\partial T}{\partial x}=\alpha\frac{\partial^2 T}{\partial y^2}+\frac{\sigma B_o^2}{(\rho C_p)_f}u^2+\frac{\nu}{(C_p)_f}\left(\frac{\partial u}{\partial y}\right)^2 + \tau\left[D_B\frac{\partial T}{\partial y}\frac{\partial C}{\partial y}+\frac{D_T}{T_\infty}\left(\frac{\partial T}{\partial y}\right)^2\right], \tag{2.3}$$

$$u\frac{\partial C}{\partial x}+v\frac{\partial C}{\partial y}-D_B\frac{\partial^2 C}{\partial y^2}=\frac{D_T}{T_\infty}\left(\frac{\partial^2 T}{\partial y^2}\right), \tag{2.4}$$

$$u\frac{\partial N}{\partial x}+v\frac{\partial N}{\partial y}-D_N\frac{\partial^2 N}{\partial y^2}=\frac{b_c W_c}{(C_w-C_\infty)}\frac{\partial}{\partial y}\left(N\frac{\partial C}{\partial y}\right). \tag{2.5}$$

2.2.1 Boundary Conditions

$$\left.\begin{aligned} &u=u_w+u_\gamma\frac{\partial u}{\partial y}\left(1-u\zeta\frac{\partial u}{\partial y}\right)^{\frac{1}{2}},\ v=0,\ -\kappa\frac{\partial T}{\partial y}=(T_w-T)h_t,\\ &N=N_w,\ C=C_w,\ at\ y=0,\\ &u\longrightarrow 0,\quad N\longleftrightarrow N_\infty,\quad C\longrightarrow C_\infty,\quad T\longrightarrow T_\infty\quad as\ y\longrightarrow\infty. \end{aligned}\right\} \tag{2.6}$$

2.3 Similarity Transformation and Non- dimensionalization of Mathematical Model

In this section, the defining equations of the Williamson nanofluid model are converted into their dimensionless form. This process introduces suitable dimensionless variables and parameters to simplify the original equations. Through the application of the following similarity transformations, the model is reduced to a system of ordinary differential equations (ODEs), enabling efficient numerical analysis.

$$\left.\begin{aligned} &u=axF'(\eta),\ v=-\sqrt{a\nu}F(\eta),\ X(\eta)=\frac{N-N_\infty}{N_w-N_\infty},\\ &\phi(\eta)=\frac{C-C_\infty}{C_w-C_\infty},\ \theta(\eta)=\frac{T-T_\infty}{T_w-T_\infty},\ \eta=y\left(\frac{a}{\nu}\right)^{\frac{1}{2}}. \end{aligned}\right\} \tag{2.7}$$

In order to ensure that the continuity (mass conservation) equation (2.1) is satisfied, the following derivative expressions are required:

$$u=axF'(\eta).$$

$$\Rightarrow \quad \frac{\partial u}{\partial x} = aF'. \tag{2.8}$$

$$v = -\sqrt{a\nu}F$$

$$\Rightarrow \quad \frac{\partial v}{\partial y} = -\sqrt{a\nu}F'.\frac{\partial \eta}{\partial y}$$

$$= -\sqrt{a\nu}F'\frac{\partial}{\partial y}\left(y\sqrt{\frac{a}{\nu}}\right)$$

$$= -aF'. \tag{2.9}$$

Implementation of (2.8) and (2.9) in (2.1) leads to

$$aF'(\eta) - aF'(\eta) = 0.$$

As a result, (2.1) is identically satisfied.

2.3.1 Non-dimensionalization of Momentum Equation

To get the dimensionless form of the momentum equation (2.2), the following derivatives are needed:

$$\frac{\partial u}{\partial y} = \frac{\partial}{\partial y}\left(axF'(\eta)\right)$$

$$= axF''\sqrt{\frac{a}{\nu}}. \tag{2.10}$$

$$\Rightarrow \quad \frac{\partial^2 u}{\partial y^2} = ax\sqrt{\frac{a}{\nu}}F'''\frac{\partial \eta}{\partial y}$$

$$= \frac{a^2 x}{\nu}F'''. \tag{2.11}$$

Inserting the values of all partial derivatives (2.8) , (2.10) and (2.11), along with the velocity components (2.7), into equation (2.2), we get the following:

$$\left(axF'\right)aF' + \frac{\sigma B_o^2}{\rho}\left(axF'\right) + \left(-\sqrt{ax}F\right)\left(axF''\sqrt{\frac{a}{\nu}}\right) =$$
$$\nu\left[1 + \sqrt{2}\Gamma\left(axF''\sqrt{\frac{a}{\nu}}\right)\right]\left(\frac{a^2 x}{\nu}F'''\right).$$

$$\Rightarrow \; a^2x\big(F'\big)^2 - a^2xF''F = \left[1+\sqrt{2}\Gamma axF''\sqrt{\frac{a}{\nu}}\right]\big(a^2xF'''\big) - \frac{\sigma B_o^2}{\rho}axF'.$$

$$\Rightarrow \; \big(F'\big)^2 - F''F = \left[1+\sqrt{2}\Gamma axF''\sqrt{\frac{a}{\nu}}\right]F''' - \frac{\sigma B_o^2}{a\rho}F.'$$

$$\Rightarrow \; F''F + \left[1+\sqrt{2}\Gamma axF''\sqrt{\frac{a}{\nu}}\right]F''' - F'^2 - \frac{\sigma B_o^2}{a\rho}F' = 0.$$

$$\Rightarrow \quad FF'' + \Big[1+WiF''\Big]F''' - F'^2 - F'M = 0. \tag{2.12}$$

2.3.2 Non-dimensionalization of Energy Equation

Here, the detailed process for the non-dimensionalization of the energy equation (2.3) has been carried out

$$\theta = \frac{T-T_\infty}{T_w-T_\infty}$$

$$\Rightarrow \; T = T_\infty + \theta(T_w - T_\infty). \tag{2.13}$$

$$\Rightarrow \quad \frac{\partial T}{\partial x} = 0. \tag{2.14}$$

$$\Rightarrow \quad \frac{\partial T}{\partial y} = \theta'\sqrt{\frac{a}{\nu}}(T_w - T_\infty). \tag{2.15}$$

$$\Rightarrow \quad \frac{\partial^2 T}{\partial y^2} = \theta''\frac{a}{\nu}(T_w - T_\infty). \tag{2.16}$$

$$\phi = \frac{C-C_\infty}{C_w-C_\infty}$$

$$\Rightarrow \; C = \phi(C_w - C_\infty) + C_\infty. \tag{2.17}$$

$$\Rightarrow \quad \frac{\partial C}{\partial y} = \phi'\sqrt{\frac{a}{\nu}}(C_w - C_\infty). \tag{2.18}$$

By substituting equations (2.14), (2.15), (2.16) ,(2.18) and (2.10) and velocity components u and v from (2.7) into equation (2.3), we arrive at

$$\begin{aligned}\big(-\sqrt{a\nu F}\big)\sqrt{\frac{a}{\nu}}\theta'(T_w-T_\infty) &= \theta''\frac{a}{\nu}(T_w-T_\infty)\alpha+\frac{\sigma B_o^2}{(\rho C_p)_f}\big(axF'\big)^2\\ &+\frac{\nu}{(C_p)_f}\left(axF''\sqrt{\frac{a}{\nu}}\right)^2+\tau\left[D_B\left((T_w-T_\infty)\sqrt{\frac{a}{\nu}}\theta'\right)\right.\\ &\left.\left((C_w-C_\infty)\sqrt{\frac{a}{\nu}}\phi'\right)+\frac{D_T}{T_\infty}\left((T_w-T_\infty)\sqrt{\frac{a}{\nu}}\theta'\right)^2\right].\end{aligned}$$

$$\begin{aligned}\Rightarrow\ -aF\theta'\big(T_w-T_\infty\big) &= \tau\frac{aD_T}{\nu T_\infty}\big(T_w-T_\infty\big)^2\theta'^2+\frac{\sigma B_o^2}{(\rho C_p)_f}a^2x^2F'^2\\ &+\frac{a^3x^2}{(C_p)_f}F''^2+\tau D_B\big(T_w-T_\infty\big)\big(C_w-C_\infty\big)\frac{a}{\nu}\theta'\phi'+\frac{a\alpha}{\nu}\big(T_w-T_\infty\big)\theta''.\end{aligned}$$

$$\begin{aligned}\Rightarrow\ -\theta'F &= \tau\frac{D_T}{\nu T_\infty}\big(T_w-T_\infty\big)\theta'^2+\frac{\alpha}{\nu}\theta''+\frac{ax^2\sigma B_o^2}{\big(T_w-T_\infty\big)(\rho C_p)_f}F'^2\\ &+\frac{a^2x^2}{\big(T_w-T_\infty\big)(C_p)_f}F''^2+\tau\frac{D_B}{\nu}\big(C_w-C_\infty\big)\theta'\phi'.\end{aligned}$$

$$\Rightarrow\ -\theta'F = Nt\theta'^2+\frac{1}{Pr}\theta''+(F')^2MEc+EcF''^2+Nb\theta'\phi'.$$

$$\Rightarrow\ \frac{1}{Pr}\theta''+(F')^2MEc+Ec(F'')^2+Nb\theta'\phi'+Nt(\theta')^2+\theta'F=0.$$

$$\Rightarrow\ \theta''+Pr\left[F'^2MEc+F''^2Ec+\theta'\phi'Nb+\theta'^2Nt+\theta'F\right]=0. \tag{2.19}$$

2.3.3 Non-dimensionalization of Concentration Equation

For the non-dimensionalization of the concentration equation (2.4), the derivatives given below will be used:

$$\frac{\partial C}{\partial x}=0. \tag{2.20}$$

$$\frac{\partial^2 C}{\partial y^2}=\frac{a}{\nu}\big(C_w-C_\infty\big)\phi''. \tag{2.21}$$

Using (2.16), (2.18), (2.20), (2.21) in equation(2.4), we have:

$$\big(-\sqrt{a\nu}F\big)\big(C_w-C_\infty\big)\sqrt{\frac{a}{\nu}}\phi'=D_B\phi''\frac{a}{\nu}\big(C_w-C_\infty\big)+\frac{a}{\nu}\theta''\frac{D_T}{T_\infty}\big(T_w-T_\infty\big).$$

$$\Rightarrow -\phi' F\frac{\nu}{D_B} = \phi'' + \theta''\frac{D_T(T_w - T_\infty)}{(C_w - C_\infty)D_B T_\infty}.$$

$$\Rightarrow \phi'' + ScF\phi' + \frac{Nt}{Nb}\theta'' = 0. \tag{2.22}$$

2.3.4 Non-Dimensionalization of Motile Equation

To derive the dimensionless form of the motile equation, the following differential terms will be employed:

$$X = \frac{N - N_\infty}{N_w - N_\infty}$$

$$\Rightarrow N = N_\infty + (N_w - N_\infty)X. \tag{2.23}$$

$$\Rightarrow \frac{\partial N}{\partial x} = 0. \tag{2.24}$$

$$\Rightarrow \frac{\partial N}{\partial y} = \big(N_w - N_\infty\big)\sqrt{\frac{a}{\nu}}X'. \tag{2.25}$$

$$\Rightarrow \frac{\partial^2 N}{\partial y^2} = \frac{a}{\nu}\big(N_w - N_\infty\big)X''. \tag{2.26}$$

Inserting equations (2.24), (2.25), (2.26), and (2.18) into equation (2.5) leads to:

$$\big(-\sqrt{a\nu}F\big)X'\big(N_w - N_\infty\big)\sqrt{\frac{a}{\nu}} = \frac{a}{\nu}D_N X''\big(N_w - N_\infty\big) - \frac{b_c W_c}{(C_w - C_\infty)}\frac{\partial}{\partial y}\left[\left((C_w - C_\infty)\sqrt{\frac{a}{\nu}}\phi'\right)\Big(N_\infty + (N_w - N_\infty)X\Big)\right].$$

$$\Rightarrow = \frac{a}{\nu}D_N\big(N_w - N_\infty\big)X'' - \frac{b_c W_c}{(C_w - C_\infty)}\left[\frac{a}{\nu}\big(N_w - N_\infty\big)\big(C_w - C_\infty\big)\big(X\phi'' + \phi' X'\big) + \frac{a}{\nu}N_\infty(C_w - C_\infty)\phi''\right].$$

$$\Rightarrow -\frac{\nu}{D_N}FX' = X'' - \frac{b_c W_c}{D_N}\left[X\phi'' + \phi' X' + \frac{N_\infty}{N_w - N_\infty}\phi''\right].$$

$$\Rightarrow -SbFX' = X'' - Pe\left[X\phi'' + \phi' X' + \Omega\phi''\right].$$

$$\Rightarrow X'' + SbFX' - Pe\left[X\phi'' + \phi' X' + \Omega\phi''(\eta)\right] = 0. \tag{2.27}$$

2.3.5 Non-dimensionalization of Boundary Conditions

- $u = u_w + u_\gamma \dfrac{\partial u}{\partial y}\left(1 - u_\zeta \dfrac{\partial u}{\partial y}\right)^{-\frac{1}{2}}, \qquad at \quad y = 0.$

$\Rightarrow \quad axF' = ax + \gamma_0\sqrt{x}\left(axF''\sqrt{\dfrac{a}{\nu}}\right)\left(1 - \zeta_0\sqrt{x}axF''\sqrt{\dfrac{a}{\nu}}\right)^{-\frac{1}{2}} \qquad at \quad \eta = 0.$

$\Rightarrow \quad F' = 1 + \gamma_1\left(\dfrac{F''}{\sqrt{1-\zeta_1 F''}}\right) \qquad at \quad \eta = 0.$

- $v = 0 \qquad at \quad y = 0.$

$\Rightarrow \quad -\sqrt{a\nu}F = 0 \qquad at \quad \eta = 0.$

$\Rightarrow \quad F = 0 \qquad at \quad \eta = 0.$

- $-k\dfrac{\partial T}{\partial y} = h_t\big(T_w - T\big) \qquad at \quad y = 0.$

$\Rightarrow \quad -k\big(T_w - T_\infty\big)\theta'\sqrt{\dfrac{a}{\nu}} = h_t\big(T_w - T_\infty - (T_w - T_\infty)\big)\theta \qquad at \quad \eta = 0.$

$\Rightarrow \quad \theta' = \dfrac{h_t}{k}\sqrt{\dfrac{a}{\nu}}\big(1-\theta\big) \qquad at \quad \eta = 0.$

$\Rightarrow \quad \theta' = B_i\big(1 - \theta\big) \qquad at \quad \eta = 0.$

- $C = C_w \qquad at \quad y = 0.$

$\Rightarrow \quad C_\infty + \big(C_w - C_\infty\big)\phi = C_w \qquad at \quad \eta = 0.$

$\Rightarrow \quad \phi = \dfrac{C_w - C_\infty}{C_w - C_\infty} \qquad at \quad \eta = 0.$

$\Rightarrow \quad \phi = 1 \qquad at \quad \eta = 0.$

- $N = N_w \qquad at \quad y = 0.$

$\Rightarrow \quad N_\infty + \big(N_w - N_\infty\big)X = N_w \qquad at \quad \eta = 0.$

$\Rightarrow \quad X = \dfrac{N_w - N_\infty}{N_w - N_\infty} \qquad at \quad \eta = 0.$

$\Rightarrow \quad X = 1 \qquad at \quad \eta = 0.$

- $u \longrightarrow 0 \qquad as \quad y \longrightarrow \infty.$

$$\Rightarrow \quad axF' \longrightarrow 0 \qquad as \quad \eta \longrightarrow \infty.$$

$$\Rightarrow \quad F' \longrightarrow 0 \qquad as \quad \eta \longrightarrow \infty.$$

- $T \longrightarrow T_\infty \qquad as \quad y \longrightarrow \infty.$

$$\Rightarrow \quad T_\infty + \big(T_w - T_\infty\big)\theta \longrightarrow T_\infty \qquad as \quad \eta \longrightarrow \infty.$$

$$\Rightarrow \quad \big(T_w - T_\infty\big)\theta \longrightarrow 0 \qquad as \quad \eta \longrightarrow \infty.$$

$$\Rightarrow \quad \theta \longrightarrow 0 \qquad as \quad \eta \longrightarrow \infty.$$

- $C \longrightarrow C_\infty \qquad as \quad y \longrightarrow \infty.$

$$\Rightarrow \quad C_\infty + \big(C_w - C_\infty\big)\phi \longrightarrow C_\infty \qquad as \quad \eta \longrightarrow \infty.$$

$$\Rightarrow \quad \big(C_w - C_\infty\big)\phi \longrightarrow 0 \qquad as \quad \eta \longrightarrow \infty.$$

$$\Rightarrow \quad \phi(\eta) \longrightarrow 0 \qquad as \quad \eta \longrightarrow \infty.$$

- $N \longrightarrow N_\infty \qquad as \quad y \longrightarrow \infty.$

$$\Rightarrow \quad N_\infty + \big(N_w - N_\infty\big)X \longrightarrow N_\infty \qquad as \quad \eta \longrightarrow \infty.$$

$$\Rightarrow \quad \big(N_w - N_\infty\big)X \longrightarrow 0 \qquad as \quad \eta \longrightarrow \infty.$$

$$\Rightarrow \quad X \longrightarrow 0 \qquad as \quad \eta \longrightarrow \infty.$$

In the above governing equations, the parameters M, Wi, Nb, Nt, Pr, Ec, α, Sc, Sb, Ω and Pe are employed. These quantities are written as below:

$$\left.\begin{aligned}
&Wi = \sqrt{2}\Gamma U_w \sqrt{\frac{a}{\nu}}, \quad M = \frac{\sigma B_0^2}{a\rho}, \quad Nb = \frac{\tau D_B (T_w - T_\infty)}{\nu}, \\
&Nt = \frac{\tau D_T (T_w - T_\infty)}{\nu T_\infty}, \quad Pr = \frac{\nu}{\alpha}, \quad \alpha = \frac{K}{(Cp)_f}, \\
&Ec = \frac{u_w^2}{(T_w - T_\infty)(Cp)_f}, \quad \tau = \frac{(Cp)_p}{(Cp)_f}, \quad U_w = ax, \\
&Sc = \frac{\nu}{D_B}, \quad Sb = \frac{\nu}{D_N}, \quad Pe = \frac{b_c W_c}{D_N}, \quad \Omega = \frac{N_\infty}{(N_w - N_\infty)}.
\end{aligned}\right\}$$

2.3.6 Non-dimensionalization of the Physical Quantities

This segment of the present section focuses on the non-dimensionalization of the Nusselt number, the skin friction, the Sherwood number and motile density number.

2.3.6.1 Skin Friction

$$
\begin{aligned}
C_f &= \frac{\mu\left[\left(\frac{\partial u}{\partial y}\right)_{y=0} + \frac{\Gamma}{\sqrt{2}}\left(\frac{\partial u}{\partial y}\right)^2_{y=0}\right]}{\rho_f u_w^2} \\
&= \frac{\mu\left[axF''(0)\sqrt{\frac{a}{\nu}} + \frac{\Gamma}{\sqrt{2}}\left(axF''(0)\sqrt{\frac{a}{\nu}}\right)^2\right]}{\rho_f a^2x^2} \\
&= \frac{\mu}{\rho_f a^2x^2}\left(axF''(0)\sqrt{\frac{a}{\nu}}\right) + \frac{\mu}{\rho_f a^2x^2}\left(\frac{\sqrt{2}\Gamma}{2}\right)\left(axF''(0)\sqrt{\frac{a}{\nu}}\right)^2 \\
&= \frac{\mu}{\rho_f ax}\left(F''(0)\sqrt{\frac{a}{\nu}}\right) + \frac{\mu}{\rho_f}\left(\frac{a}{\nu}F''(0)^2\right)\left(\frac{\sqrt{2}\Gamma}{2}\right) \\
&= \frac{\nu}{ax}\left(F''(0)\sqrt{\frac{a}{\nu}}\right) + \nu\left(\frac{a}{\nu}F''(0)^2\right)\left(\frac{\sqrt{2}\Gamma}{2}\right) \\
C_f\sqrt{Re_x} &= \frac{\nu}{ax}\left(F''(0)\sqrt{\frac{a}{\nu}}\right)\sqrt{\frac{a}{\nu}}x + \nu x\sqrt{\frac{a}{\nu}}\left(\frac{a}{\nu}F''(0)^2\right)\left(\frac{\sqrt{2}\Gamma}{2}\right) \\
C_f\sqrt{Re_x} &= F''(0) + ax\left(\frac{\sqrt{2}\Gamma}{2}\right)\sqrt{\frac{a}{\nu}}F''(0)^2 \\
C_f\sqrt{Re_x} &= F''(0) + \frac{Wi}{2}F''(0)^2.
\end{aligned}
\tag{2.28}
$$

where Re is defined as $\left(Re\right)^{\frac{1}{2}} = \sqrt{\frac{a}{\nu}}x$.

2.3.6.2 Nusslt Number

$$
Nu_x = \frac{-x\left(\frac{\partial T}{\partial y}\right)_{y=0}}{(T_w - T_\infty)}
$$

$$= \frac{-(T_w - T_\infty)\sqrt{\frac{a}{\nu}}\theta'(0)x}{(T_w - T_\infty)}$$

$$= -\left(\frac{a}{\nu}\right)^{\frac{1}{2}}\theta'(0)x$$

$$\Rightarrow \quad \frac{Nu_x}{x\sqrt{\frac{a}{\nu}}} = -\theta'(0).$$

$$\Rightarrow \quad \frac{Nu_x}{\sqrt{Re_x}} = \theta'(0). \tag{2.29}$$

2.3.6.3 Sherwood Number

$$Sh_x = \frac{-D_B x\left(\frac{\partial C}{\partial y}\right)_{y=0}}{D_B(C_w - C_\infty)}$$

$$Sh_x = \frac{-x(C_w - C_\infty)\sqrt{\frac{a}{\nu}}\phi'(0)}{(C_w - C_\infty)}$$

$$= -x\sqrt{\frac{a}{\nu}}\phi'(0)$$

$$\Rightarrow \quad \frac{Sh_x}{x\sqrt{\frac{a}{\nu}}} = -\phi'(0).$$

$$\Rightarrow \quad \frac{Sh_x}{\sqrt{Re_x}} = \phi'(0). \tag{2.30}$$

2.3.6.4 Motile Density Number

$$Nn_x = \frac{-D_N x\left(\frac{\partial N}{\partial y}\right)_{y=0}}{D_N(N_w - N_\infty)}$$

$$= \frac{-x(N_w - N_\infty)\sqrt{\frac{a}{\nu}}X'(0)}{(N_w - N_\infty)}$$

$$= -x\sqrt{\frac{a}{\nu}}X'(0)$$

$$\Rightarrow \quad \frac{Nn_x}{x\sqrt{\frac{a}{\nu}}} = -X'(0).$$

$$\Rightarrow \quad \frac{Nn_x}{\sqrt{Re_x}} = X'(0). \tag{2.31}$$

2.4 Solution Framework

To find a solution of the momentum equation (2.12), the shooting method has been executed. For this purpose, the following notations have been employed:

$$F = \widetilde{K}_1, \qquad F' = \widetilde{K}_1' = \widetilde{K}_2, \qquad F'' = \widetilde{K}_2' = \widetilde{K}_3.$$

The momentum equation is reformulated as the following system of first-order ODEs:

$$\widetilde{K}_1 = \widetilde{K}_2, \qquad \widetilde{K}_1(0) = 0,$$

$$\widetilde{K}_2 = \widetilde{K}_3, \qquad \widetilde{K}_2(0) = 1+\gamma_1\left[\frac{\widetilde{K}_3(0)}{\sqrt{1-\zeta_1\widetilde{K}_3(0)}}\right],$$

$$\widetilde{K}_3 = \left(\widetilde{K}_2^2 - \widetilde{K}_1\widetilde{K}_3 + M\widetilde{K}_2\right)\frac{1}{1+w_i\widetilde{K}_3}, \qquad \widetilde{K}_3(0) = \mathcal{R}.$$

While using the Runge-Kutta 4th order method for the numerical solution of the above IVP, the missing condition $\mathcal{R}$ should be selected so that

$$\widetilde{K}_2\left(\eta_\infty, \mathcal{R}\right) = 0.$$

Newton's iterative method is applied to compute $\mathcal{R}$. This method follows the iterative scheme given below:

$$\mathcal{R}^{(n+1)} = \mathcal{R}^{(n)} - \frac{\widetilde{K}_2\left(\eta_\infty, \mathcal{R}^{(n)}\right)}{\left(\frac{\partial}{\partial\mathcal{R}}\widetilde{K}_2\left(\eta_\infty, \mathcal{R}\right)\right)^{(n)}}.$$

To apply the above iterative scheme, the following derivatives are needed:

$$\frac{\partial \widetilde{K}_1}{\partial \mathcal{R}} = \widetilde{K}_4, \qquad \frac{\partial \widetilde{K}_2}{\partial \mathcal{R}} = \widetilde{K}_5, \qquad \frac{\partial \widetilde{K}_3}{\partial \mathcal{R}} = \widetilde{K}_6.$$

Accordingly, with the updated notations, Newton's scheme becomes:

$$\mathcal{R}^{(n+1)} = \mathcal{R}^{(n)} - \frac{\widetilde{K}_2\big(\eta_\infty, \mathcal{R}^n\big)}{\widetilde{K}_5\big(\eta_\infty, \mathcal{R}^n\big)}.$$

By differentiating the given system of first-order ODEs with respect to R, we arrive at a new system of ODEs, written below:

$$\widetilde{K}_4 = \widetilde{K}_5, \qquad \widetilde{K}_4(0) = 0,$$

$$\widetilde{K}_5 = \widetilde{K}_6, \qquad \widetilde{K}_5(0) = \frac{\gamma_1}{\sqrt{1-\zeta_1\mathcal{R}}} + \frac{\gamma_1 R\zeta_1}{2\big(1-\zeta_1\mathcal{R}\big)^{\frac{3}{2}}},$$

$$\widetilde{K}_6 = \Bigg(\big(1+w_i\widetilde{K}_3\big)\big(2\widetilde{K}_2\widetilde{K}_5 - \widetilde{K}_1\widetilde{K}_6 - \widetilde{K}_3\widetilde{K}_4 + M\widetilde{K}_5\big) - w_i\widetilde{K}_6\big(\widetilde{K}_2^2 - \widetilde{K}_1\widetilde{K}_3 + M\widetilde{K}_2\big)\Bigg) \frac{1}{\big(1+w_i\widetilde{K}_3\big)^2} \qquad \widetilde{K}_6(0) = 1.$$

The iterative process terminates when the following condition is met:

$$\left|\widetilde{K}_2\big(\eta_\infty, \mathcal{R}^n\big)\right| < \epsilon_1.$$

Here, ε_1 is an arbitrarily small positive number. From now onward, the tolerance is set as $\varepsilon = 10^{-9}$ for all computations. Now, we solve (2.19) and (2.22) numerically using the shooting method,treating F, F' and F'' as the known functions. The following notations will be used for this purpose:

$$\theta = \widetilde{\mathcal{L}}_1, \qquad \theta' = \widetilde{\mathcal{L}}_1' = \widetilde{\mathcal{L}}_2, \qquad \phi = \widetilde{\mathcal{L}}_3, \qquad \phi' = \widetilde{\mathcal{L}}_3' = \widetilde{\mathcal{L}}_4.$$

The equations (2.19) and (2.22) are transformed into the following first order coupled ODEs;

$$\widetilde{\mathcal{L}}_1' = \widetilde{\mathcal{L}}_2, \qquad \widetilde{\mathcal{L}}_1(0) = c,$$

$$\widetilde{\mathcal{L}}_2' = -Pr\left[F\widetilde{\mathcal{L}}_2 + EcF''^2 + MEcF'^2 + Nb\widetilde{\mathcal{L}}_2\widetilde{\mathcal{L}}_4 + Nt\widetilde{\mathcal{L}}_2^2\right], \qquad \widetilde{\mathcal{L}}_2(0) = -Bi(1-\widetilde{\mathcal{L}}_1),$$

$$\widetilde{\mathcal{L}}_3' = \widetilde{\mathcal{L}}_4, \qquad \widetilde{\mathcal{L}}_3(0) = 1,$$

$$\widetilde{\mathcal{L}}_4' = -ScF\widetilde{\mathcal{L}}_4 - \frac{Nt}{Nb}\left[-Pr\big(F\widetilde{\mathcal{L}}_2 + EcF''^2 + MEcF'^2 + Nb\widetilde{\mathcal{L}}_2\widetilde{\mathcal{L}}_4 + Nt\widetilde{\mathcal{L}}_2^2\big)\right], \quad \widetilde{\mathcal{L}}_4(0) = d.$$

The RK-4 method has been applied to solve the above IVP. The missing conditions c and d should be chosen such that:

$$\widetilde{\mathcal{L}}_1\big(\eta_\infty, c, d\big) = 0, \qquad \widetilde{\mathcal{L}}_3\big(\eta_\infty, c, d\big) = 0.$$

To determine the missing conditions c and d, Newton's method is employed, using the following iterative scheme:

$$\begin{bmatrix} c \\ d \end{bmatrix}^{(n+1)} = \begin{bmatrix} c \\ d \end{bmatrix}^{(n)} - \left(\begin{bmatrix} \frac{\partial\widetilde{\mathcal{L}}_1}{\partial c} & \frac{\partial\widetilde{\mathcal{L}}_1}{\partial d} \\ \frac{\partial\widetilde{\mathcal{L}}_3}{\partial c} & \frac{\partial\widetilde{\mathcal{L}}_3}{\partial d} \end{bmatrix}^{-1}\right)^{(n)} \begin{bmatrix} \widetilde{\mathcal{L}}_1 \\ \widetilde{\mathcal{L}}_3 \end{bmatrix}^{(n)}$$

Now, introduce the following notations:

$$\frac{\partial\widetilde{\mathcal{L}}_1}{\partial c} = \widetilde{\mathcal{L}}_5, \quad \frac{\partial\widetilde{\mathcal{L}}_2}{\partial c} = \widetilde{\mathcal{L}}_6, \quad \frac{\partial\widetilde{\mathcal{L}}_3}{\partial c} = \widetilde{\mathcal{L}}_7, \quad \frac{\partial\widetilde{\mathcal{L}}_4}{\partial c} = \widetilde{\mathcal{L}}_8,$$
$$\frac{\partial\widetilde{\mathcal{L}}_1}{\partial d} = \widetilde{\mathcal{L}}_9, \quad \frac{\partial\widetilde{\mathcal{L}}_2}{\partial d} = \widetilde{\mathcal{L}}_{10}, \quad \frac{\partial\widetilde{\mathcal{L}}_3}{\partial d} = \widetilde{\mathcal{L}}_{11}, \quad \frac{\partial\widetilde{\mathcal{L}}_4}{\partial d} = \widetilde{\mathcal{L}}_{12}.$$

With these new notations, Newton's iterative scheme can be expressed as:

$$\begin{bmatrix} c \\ d \end{bmatrix}^{(n+1)} = \begin{bmatrix} c \\ d \end{bmatrix}^{(n)} - \left(\begin{bmatrix} \widetilde{\mathcal{L}}_5 & \widetilde{\mathcal{L}}_9 \\ \widetilde{\mathcal{L}}_7 & \widetilde{\mathcal{L}}_{11} \end{bmatrix}^{-1}\right)^{(n)} \begin{bmatrix} \widetilde{\mathcal{L}}_1 \\ \widetilde{\mathcal{L}}_3 \end{bmatrix}^{(n)}$$

Differentiation of the last system of four first-order ODEs with respect to c and d yields another system of ODEs, as shown below:

$$\widetilde{\mathcal{L}}_5' = \widetilde{\mathcal{L}}_6, \qquad \widetilde{\mathcal{L}}_5(0) = 1,$$

$$\widetilde{\mathcal{L}}_6' = -Pr\left[F\widetilde{\mathcal{L}}_6 + Nb\big(\widetilde{\mathcal{L}}_6\widetilde{\mathcal{L}}_4 + \widetilde{\mathcal{L}}_2\widetilde{\mathcal{L}}_8\big) + 2Nt\widetilde{\mathcal{L}}_2\widetilde{\mathcal{L}}_6\right], \qquad \widetilde{\mathcal{L}}_6(0) = -Bi\widetilde{\mathcal{L}}_5,$$

$$\widetilde{\mathcal{L}}_7' = \widetilde{\mathcal{L}}_8, \qquad \widetilde{\mathcal{L}}_7(0) = 0,$$

$$\widetilde{\mathcal{L}}_8' = -ScF\widetilde{\mathcal{L}}_8 - \frac{Nt}{Nb}\Big[- Pr\big(F\widetilde{\mathcal{L}}_6 + Nb\big(\widetilde{\mathcal{L}}_6\widetilde{\mathcal{L}}_4 + \widetilde{\mathcal{L}}_2\widetilde{\mathcal{L}}_8\big) + 2Nt\widetilde{\mathcal{L}}_2\widetilde{\mathcal{L}}_6\big)\Big], \quad \widetilde{\mathcal{L}}_8(0) = 0,$$

$$\widetilde{\mathcal{L}}_9' = \widetilde{\mathcal{L}}_{10}, \qquad \widetilde{\mathcal{L}}_9(0) = 0,$$

$$\widetilde{\mathcal{L}}_{10}' = -Pr\Big[F\widetilde{\mathcal{L}}_{10}+Nb\big(\widetilde{\mathcal{L}}_{10}\widetilde{\mathcal{L}}_4+\widetilde{\mathcal{L}}_2\widetilde{\mathcal{L}}_{12}\big)+2Nt\widetilde{\mathcal{L}}_2\widetilde{\mathcal{L}}_{10}\Big], \qquad \widetilde{\mathcal{L}}_{10}(0) = -Bi\widetilde{\mathcal{L}}_9,$$

$$\widetilde{\mathcal{L}}_{11}' = \widetilde{\mathcal{L}}_{12}, \qquad \widetilde{\mathcal{L}}_{11}(0) = 0,$$

$$\widetilde{\mathcal{L}}_{12}' = -ScF\widetilde{\mathcal{L}}_{12}-\frac{Nt}{Nb}\Big[-Pr\big(F\widetilde{\mathcal{L}}_{10}+Nb\big(\widetilde{\mathcal{L}}_{10}\widetilde{\mathcal{L}}_4+\widetilde{\mathcal{L}}_2\widetilde{\mathcal{L}}_{12}\big)+2Nt\widetilde{\mathcal{L}}_2\widetilde{\mathcal{L}}_{12}\big)\Big], \quad \widetilde{\mathcal{L}}_{12}(0) = 1.$$

The stopping criterion for Newton's method is set as:

$$max\Big\{\big|\widetilde{\mathcal{L}}_1\big(\eta_\infty, c^n, d^n\big)\big|, \big|\widetilde{\mathcal{L}}_3\big(\eta_\infty, c^n, d^n\big)\big|\Big\} < \epsilon_1.$$

Now, find a solution to the Motile equation (2.15) by using shooting method where θ, θ', ϕ, ϕ', F, F' and F'' are assumed to be known functions. The following notations will be considered for applying the shooting method:

$$X = \widetilde{J}_1, \qquad X' = \widetilde{J}_1' = \widetilde{J}_2.$$

The Motile equation can be expressed as the following system of ODE:

$$\widetilde{J}_1' = \widetilde{J}_2, \qquad \widetilde{J}_1(0) = 1,$$

$$\widetilde{J}_2' = - SbF\widetilde{J}_2 - Pe\Big(ScF(\widetilde{J}_1 - \Omega) - \widetilde{J}_2\Big)\phi' - Pe\big(\widetilde{J}_1 - \Omega\big)\frac{Nt}{Nb}$$
$$\Big(- Pr\big(Nt\theta'^2 + F\theta' + EcF''^2 + MEcF' + Nb\theta'\phi'\big)\Big), \qquad \widetilde{J}_2(0) = \mathcal{D}.$$

To numerically solve the above-mentioned initial value problem (IVP) using the Runge–Kutta method, the missing condition $\mathcal{D}$ in the system of equations requires careful selection. This condition $\mathcal{D}$ should be adjusted so that the solution satisfies the required boundary conditions. The missing condition $\mathcal{D}$ should be chosen such that:

$$\Big|\widetilde{J}_1\big(\eta_\infty, \mathcal{D}\big)\Big| = 0.$$

Newton's method will be applied to determine $\mathcal{D}$ with the iterative method outlined below:

$$\widetilde{J}_1^{(n+1)} = \widetilde{J}_1^{(n)} - \frac{\widetilde{J}_1\big(\eta_\infty, \mathcal{D}^{(n)}\big)}{\frac{\partial}{\partial \mathcal{D}}\big(\widetilde{J}_1(\eta_\infty, \mathcal{D})\big)^{(n)}}.$$

We now introduce the following notations:

$$\frac{\partial \widetilde{J}_1}{\partial \mathcal{D}} = \widetilde{J}_3, \qquad \frac{\partial \widetilde{J}_2}{\partial \mathcal{D}} = \widetilde{J}_4.$$

With these new notations, the Newton's iteration scheme can be described as follows:

$$\widetilde{J}_1^{(n+1)} = \widetilde{J}_1^{(n)} - \frac{\widetilde{J}_1\big(\eta_\infty, \mathcal{D}^{(n)}\big)}{\widetilde{J}_3\big(\eta_\infty, \mathcal{D}^{(n)}\big)}.$$

Now, by differentiating the system of two first-order ODEs with respect to $\mathcal{D}$, we obtain another system of ODEs, as follows:

$$\widetilde{J}_3' = \widetilde{J}_4, \qquad \widetilde{J}_3(0) = 0.$$

$$\widetilde{J}_4' = - SbF\widetilde{J}_4 - Pe\Big(ScF\widetilde{J}_3 - \widetilde{J}_4\Big)\phi' - Pe\widetilde{J}_3\frac{Nt}{Nb}\Big[- Pr\big(F\theta' + EcF''^2 + MEcF' + Nb\theta'\phi' + Nt\theta'^2\big)\Big], \quad \widetilde{J}_4(0) = 1.$$

The stopping criterion for the iterative scheme is established as:

$$\Big|\widetilde{J}_1\big(\eta_\infty, \mathcal{D}\big)\Big| < \epsilon_1.$$

2.5 Results Interpretation

This section focuses on the physical behavior of the velocity, temperature, concentration and motile profiles in response to variations in the key physical parameters, including the Williamson parameter (Wi), Prandtl number (Pr), slip parameter (γ_1), Eckert number (Ec) Biot number (Bi), Reynolds number (Re) and magnetic field parameter (M). The evaluation is performed through graphs showing velocity, temperature, motile density and concentration profiles.

Moreover, by updating the values of the dimensionless parameters, the effects of these parameters on physical quantities such as Nusselt number, skin friction, motile number and Sherwood number are examined and presented in tabular form. The concentration, velocity, temperature, and motile profiles, graphs illustrate how the system responds to changes in the physical parameters. By analyzing the trends in these profiles, a better understanding of the system's physical characteristics and energy distribution can be achieved. The graphical representations allow for the analysis of how changes in M, Wi, γ_1, Pr, Ec, Bi, and Re affect the concentration, velocity, energy and motile profiles.

2.5.1 Analysis of Computational Results

Table 2.1 presents the calculated numerical values of the skin friction coefficient for various physical parameters listed in the table.

TABLE 2.1: Skin friction coefficient $C_f\sqrt{Re_x}$ for values of Wi, M, γ_1 and ξ_1.

Wi	M	γ_1	ξ_1	$C_f\sqrt{Re_x}$
0.3	0.2	0.3	0.1	-0.71731
0.5				-0.67683
0.7				-0.62776
0.9				-0.55532
	0.4			-0.76302
	0.6			-0.80336
	0.8			-0.83943
		0.5		-0.60652
		0.6		-0.80336
		0.7		-0.83943
			0.2	-0.72467
			0.3	-0.73157
			0.4	-0.73805

Skin friction $C_f\sqrt{Re_x}$ is increasing by raising the values of the Williamson parameter Wi. For the rising values of M, γ_1 and ξ_1, the skin friction coefficient $C_f\sqrt{Re_x}$ decreases. In Table 2.2, the effect of key parameters on $\frac{Nu_x}{\sqrt{Re_x}}$ as well as $\frac{Sh_x}{\sqrt{Re_x}}$ is addressed. An increasing trend is observed in Nusselt number $\frac{Nu_x}{\sqrt{Re_x}}$ and decreasing behavior noticed in Sherwood number $\frac{Sh_x}{\sqrt{Re_x}}$ as the values of Nt, Ec, Nb and Sc increase. In Table 2.3, we discuss the effect of significant characteristics of the motile number $\frac{Nn_x}{\sqrt{Re_x}}$. The motile number decreases with increasing Peclet number (Pe) and increases with rising motile density parameter (Ω) and bio-convection Schmidt number (Sb).

TABLE 2.2: The $\frac{Nu_x}{\sqrt{Re_x}}$ and $\frac{Sh_x}{\sqrt{Re_x}}$ for different values of Nb,Nt, Sc, EC and Bi when $M = 0.2$,$Wi = 0.3$, $\gamma_1 = 0.3$ and $\xi_1 = 0.1$.

Ec	Nb	Nt	Sc	B_i	$\frac{Nu_x}{\sqrt{Re_x}}$	$\frac{Sh_x}{\sqrt{Re_x}}$
0.3	0.5	0.5	1.2	0.1	0.06180	0.56761
0.5					0.04036	0.63350
0.7					0.01841	0.70056
0.9					-0.00407	0.76886
	1				0.05809	0.56026
	1.5				0.05380	0.55832
	2				0.04881	0.55785
		1			0.06092	0.59635
		1.5			0.05998	0.62977
		2			0.05896	0.66839
			1.4		0.06143	0.63553
			1.6		0.06111	0.69875
			1.8		0.06081	0.75801
				0.2	0.11522	0.52650
				0.3	0.16179	0.49070
				0.4	0.20271	0.45929

TABLE 2.3: The motile number $\frac{Nn_x}{\sqrt{Re_x}}$ for different values of Sb, Pe and ω when $M = 0.2$, $Wi = \gamma_1 = Ec = 0.3$, $Nb = Nt = 0.5$, $Sc = 1.2$, $Bi = \xi_1 = 0.1$ and $Pr = 6.2$.

Sb	Pe	Ω	$\frac{Nn_x}{\sqrt{Re_x}}$
0.6	0.1	0.3	0.32112
0.8			0.40307
1.2			0.54618
1.6			0.66769
	0.2		0.30652
	0.3		0.28749
	0.4		0.26283
		0.6	0.33671
		0.9	0.35231
		1.2	0.36791

2.5.2 Velocity Profile

Figures 2.2 to 2.4 provide insights into the nature of the velocity profile, denoted as $F'(\zeta)$, with respect to several physical parameters including the Wi, M, and the slip parameter (γ_1) on velocity $F'(\eta)$. Figure 2.2 illustrates the impact of the magnetic parameter (M) on the dimensionless velocity profile $F'(\eta)$.

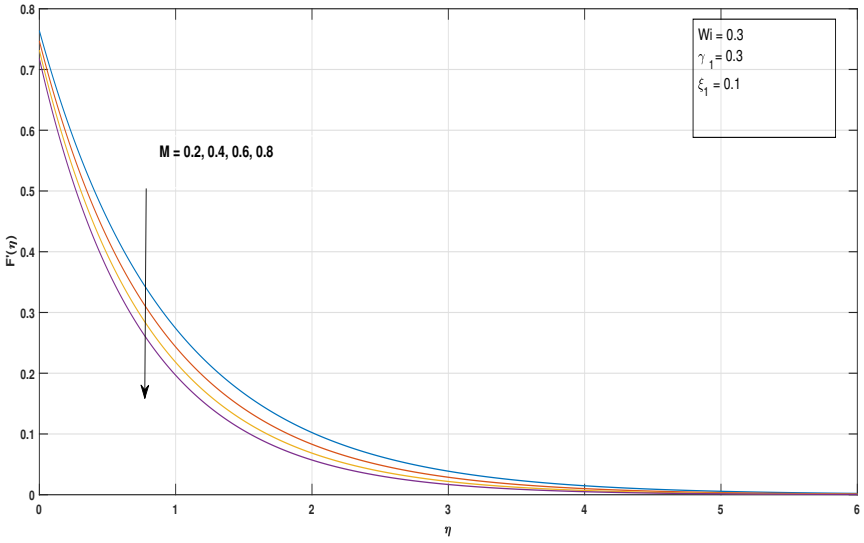

FIGURE 2.2: Influence of M on velocity profile $F'(\eta)$

It is evident that the flow velocity decreases noticeably as the value of the magnetic parameter increases across the entire flow domain. This mehanism occurs due to the Lorentz force, which acts perpendicular to the applied magnetic field and resists the fluid's motion. Figure 2.3 illustrates the influence of the Williamson parameter (Wi) on the dimensionless $F'(\eta)$. As Wi increases, a noticeable reduction in flow velocity is observed. This happens because a larger Wi means the fluid offers more resistance to movement, which slows it down. As a result, the velocity profile becomes smaller across the whole flow region. Figure 2.4 shows the impact of the slip parameter (γ_1)on the dimensionless velocity profile $F'(\eta)$. It is observed that as the slip parameter increases, the velocity near the boundary increases due to more slip at the surface. However, the overall velocity profile tends to decrease because of changes in the flow structure due to the non-Newtonian behavior of the Williamson fluid.

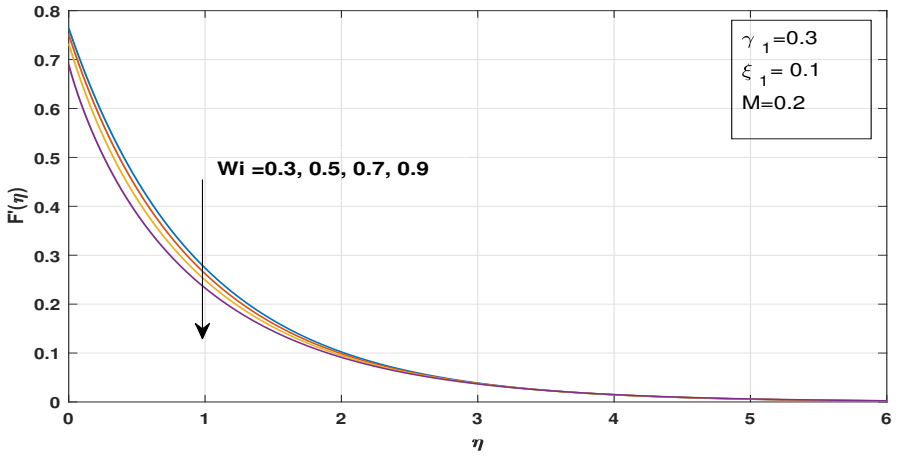

FIGURE 2.3: Influence of Wi on velocity profile $F'(\eta)$

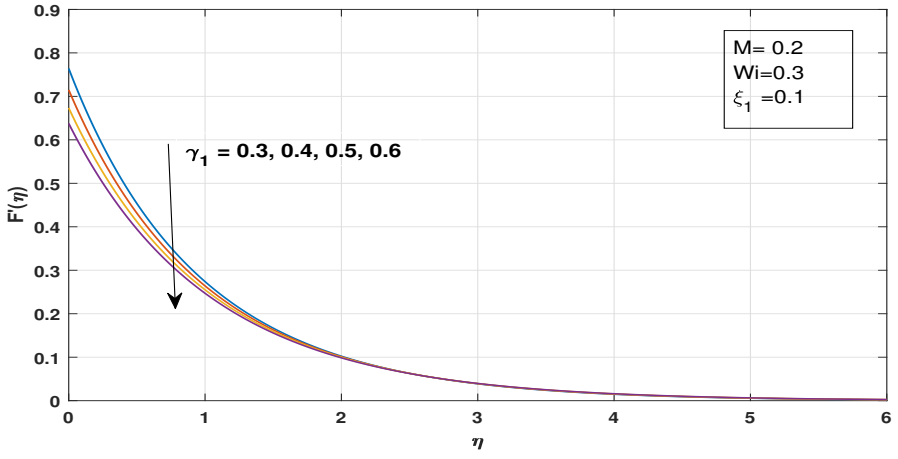

FIGURE 2.4: Influence of γ on velocity profile $F'(\eta)$

2.5.3 Temperature Profile

Figures 2.5 to 2.9 analyze the characteristics of the thermal profile $\theta(\eta)$ with respect to multiple parameters, including the thermophoresis parameter (Nt), Brownian motion parameter (Nb), Eckert number (Ec), magnetic parameter(M) and Biot number (Bi). Figures 2.5 and 2.6 illustrate the influence of the thermophoresis parameter (Nt) and the Brownian motion parameter (Nb) on the temperature profile $\theta(\eta)$ within the boundary layer. It is noted that as the values of (Nt) and (Nb) increase, the temperature profile also increases noticeably.

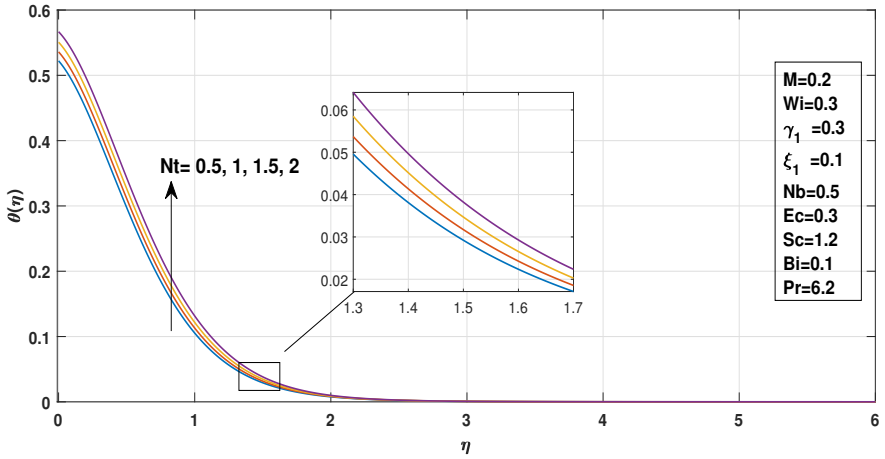

FIGURE 2.5: Influence of Nt on temperature profile $\theta(\eta)$

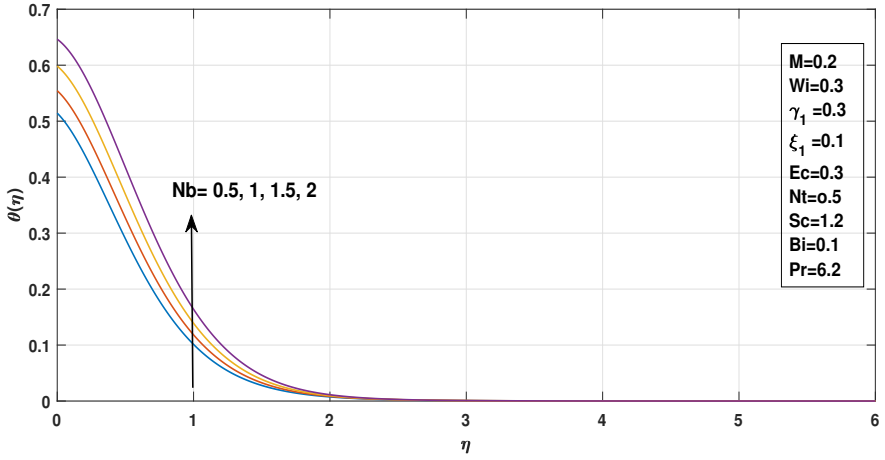

FIGURE 2.6: Impact of Nb on temperature profile $\theta(\eta)$

An increase in Nb enhances the random motion of nanoparticles, which improves thermal diffusion and leads to more uniform heat distribution in the fluid. Similarly, a

higher thermophoresis parameter (Nt) causes nanoparticles to migrate from hotter to cooler regions, which adds to the heat transfer and results in elevated fluid temperature. Therefore, both parameters play a key role in intensifying the heat transfer rate in the Williamson nanofluids.

The combined effect of stronger Brownian motion and thermophoresis leads to an overall rise in temperature within the boundary layer. The effect of the magnetic parameter (M) and the Eckert number (Ec) on the temperature profile $\theta(\eta)$ is shown in figures 2.7 and 2.8. It can be seen that when the values of M and Ec increase, the temperature of the fluid also rises.

This happens because the magnetic field creates a resisting force that slows down the fluid. When the fluid slows down, some of its motion energy changes into heat, which makes the fluid warmer.

When the value of Ec increases, more energy is lost due to friction inside the fluid. This extra friction adds to the fluid's internal energy, which makes the fluid warmer and increases its temperature throughout the flow.

Figure 2.9 illustrates the impact of the Biot number (Bi) on the temperature distribution. As Bi grows, the temperature profile $\theta(\eta)$ also rises. A higher Biot number means more heat is transferred from the surface into the fluid, which makes the thermal boundary layer thicker.

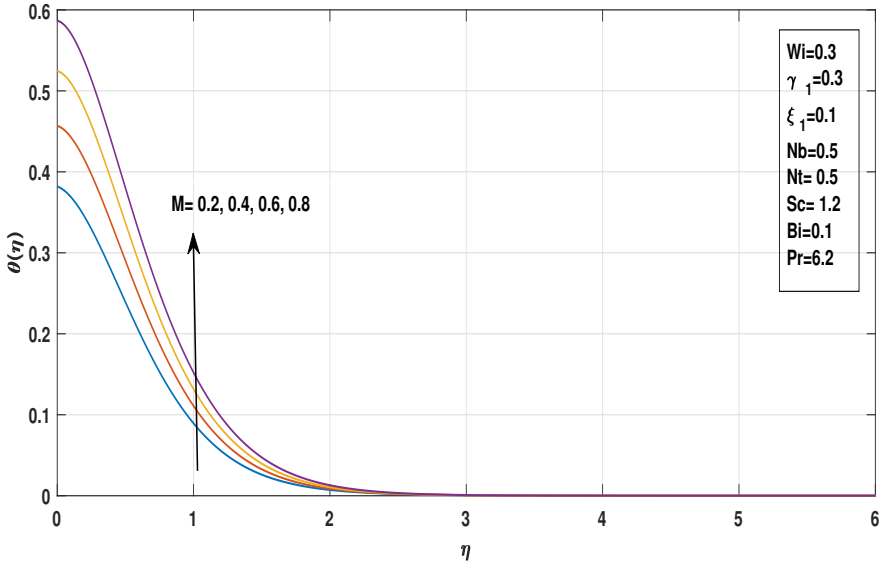

FIGURE 2.7: Impact of M on temperature profile $\theta(\eta)$

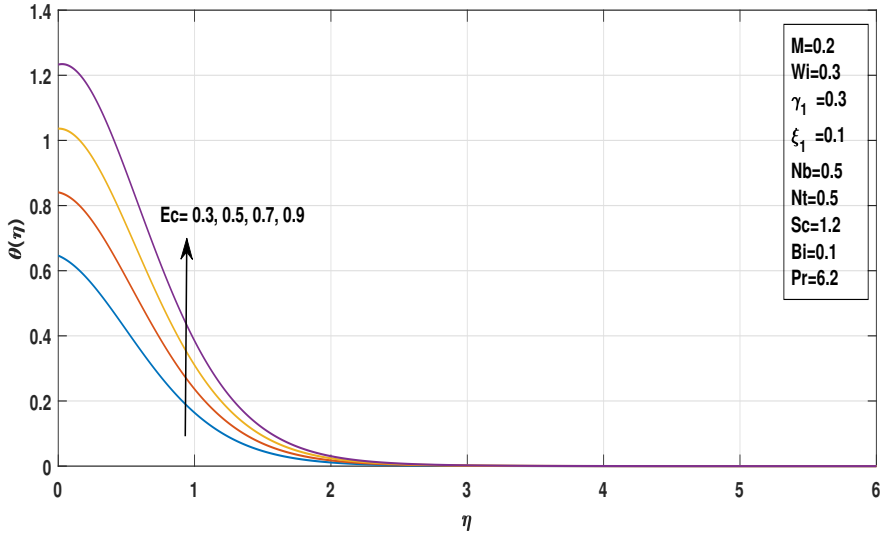

FIGURE 2.8: Influence of EC on temperature profile $\theta(\eta)$

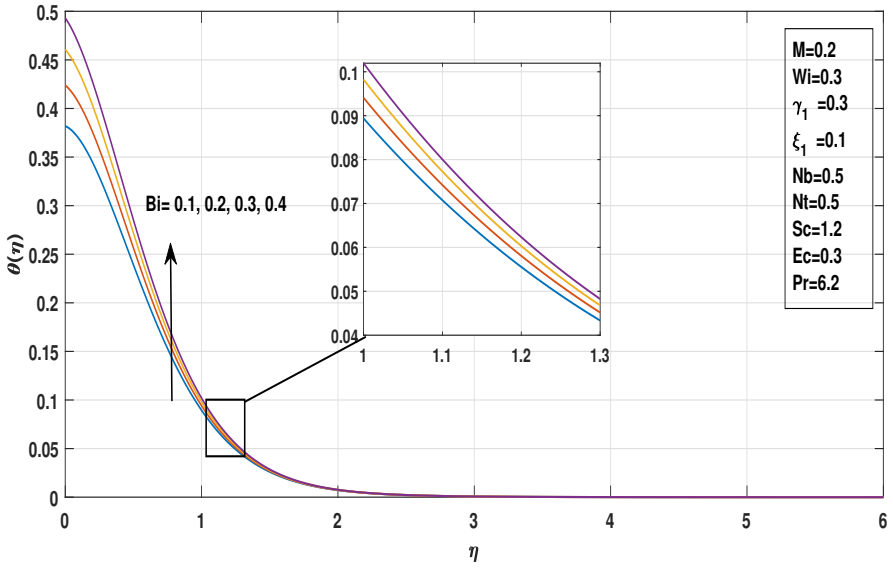

FIGURE 2.9: Influence of Bi on temperature profile $\theta(\eta)$

2.5.4 Concentration Profile

Figures 2.10 to 2.12 depict how the concentration profile $\phi(\eta)$ is affected by variations in the Schmidt number (Sc), Brownian motion parameter (Nb) and thermophoresis parameter (Nt). Figure 2.10 shows how the Nt affects the concentration profile $\phi(\eta)$. When the value of Nt increases, the concentration in the fluid also increases. This

happens because a larger Nt means more nanoparticles move from the hot area to the cold area. Therefore more particles gather in the fluid, which increases the concentration close to the surface. So, higher values of Nt make the concentration profile stronger and increase the depth of the concentration boundary layer.

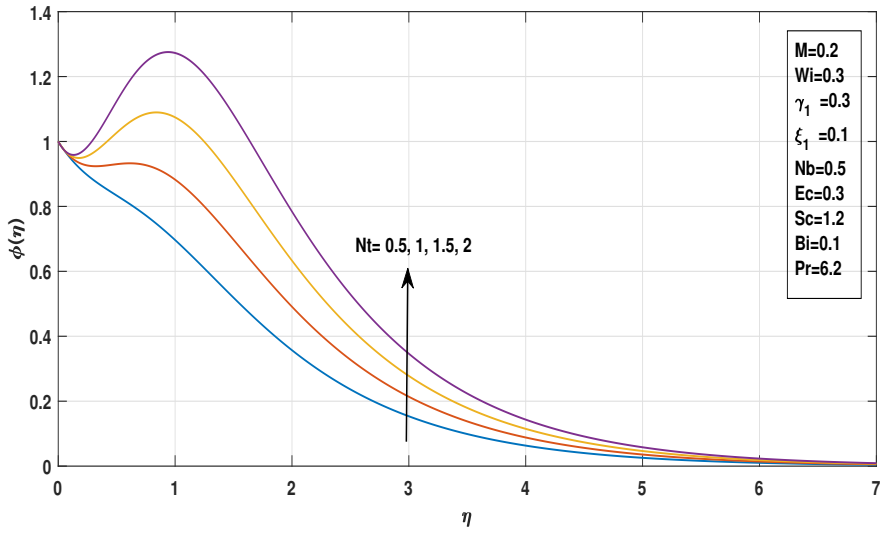

FIGURE 2.10: Outcome of Nt on concentration profile $\phi(\eta)$

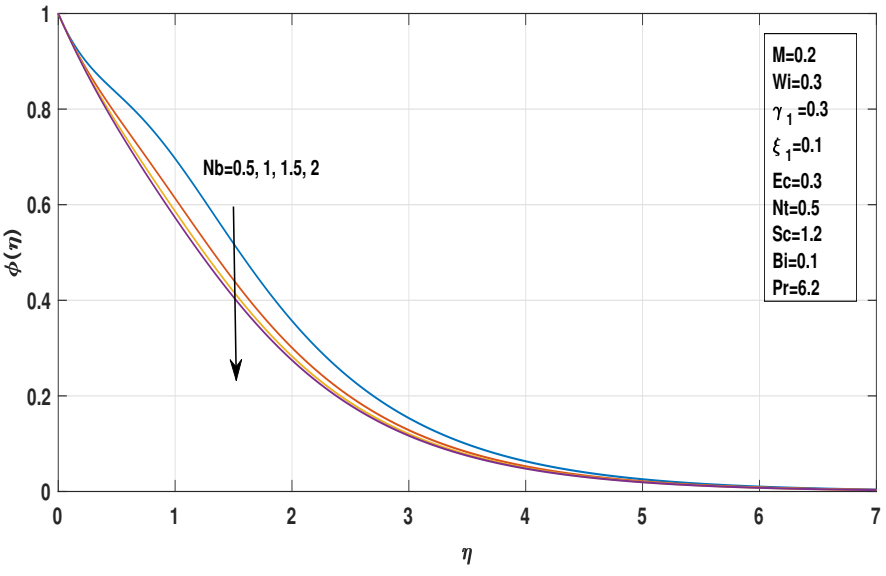

FIGURE 2.11: Outcome of Nb on concentration profile $\phi(\eta)$

Figure 2.11 and 2.12 show how the Brownian motion parameter (Nb) and Schmidt number (Sc) affect the concentration profile $\phi(\eta)$. It is recorded that when the values of Nb and Sc increase, the concentration in the fluid decreases. A larger Nb means the

nanoparticles move around more randomly, which spreads them out and lowers their concentration near the surface. Likewise, a higher Sc means the particles spread more slowly through the fluid, also reducing their concentration. Therefore, increasing Nb and Sc decreases the concentration profile and reduces concentration levels throughout the fluid.

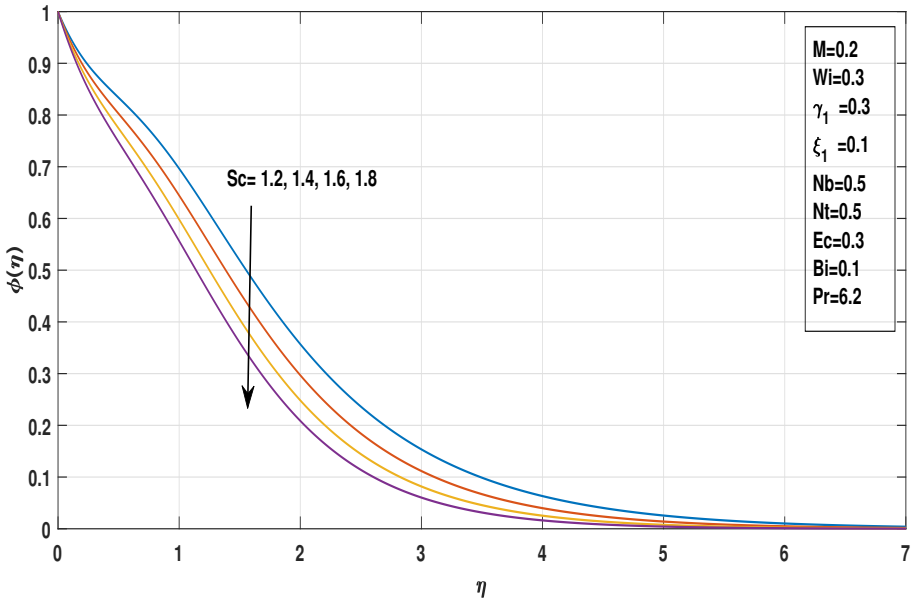

FIGURE 2.12: Influence of Sc on concentration profile $\phi(\eta)$

2.5.5 Motile Microorganism Profile

Figures 2.13 to 2.15 illustrate the effect of changes in the motile density parameter (Ω), Peclet number (Pe), and bio-convection Schmidt number (Sb) on the motile profile $X(\eta)$.

Figure 2.13 shows that the motile microorganism profile decrease when the motile density parameter (Ω) increases. This happens because a larger Ω means there are more microorganisms in the fluid. When their number increases, their upward swimming creates stronger fluid motion, which pushes some microorganisms away from the surface and spreads them more evenly in the fluid.

Figure 2.14 shows that as the Peclet number (Pe) increases, the motile profile becomes larger. This is because higher Pe values indicate that microorganism movement is mainly driven by their swimming activity, which enhances their upward transport and raises

the motile profile. Figure 2.15 shows that as the bio-convection Schmidt number (Sb) increases, the motile profile becomes smaller.

This happens because a larger Sb means the microorganisms spread more slowly in the fluid, which reduces the strength of their movement pattern and lowers the motile profile values.

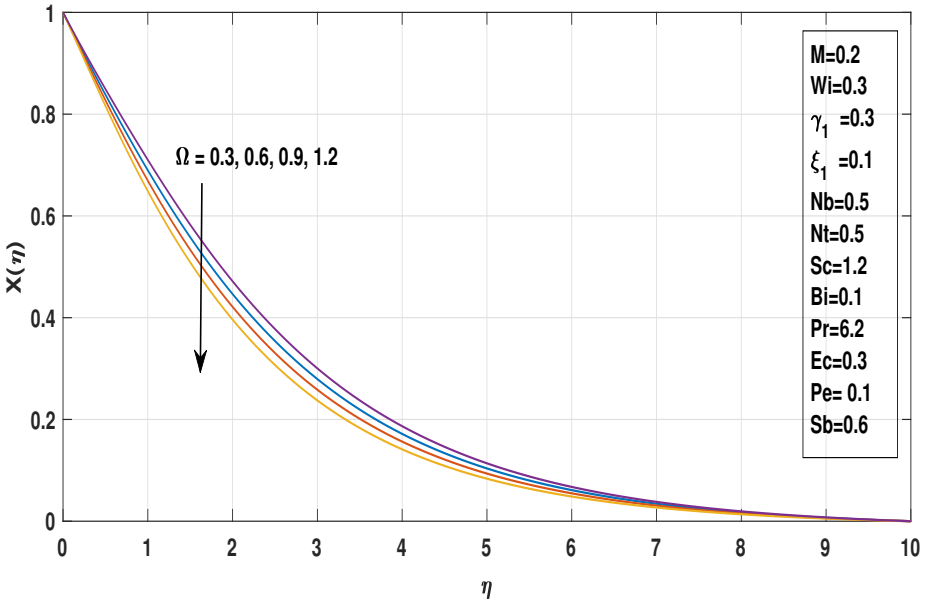

FIGURE 2.13: Influence of Ω on motile profile $X(\eta)$

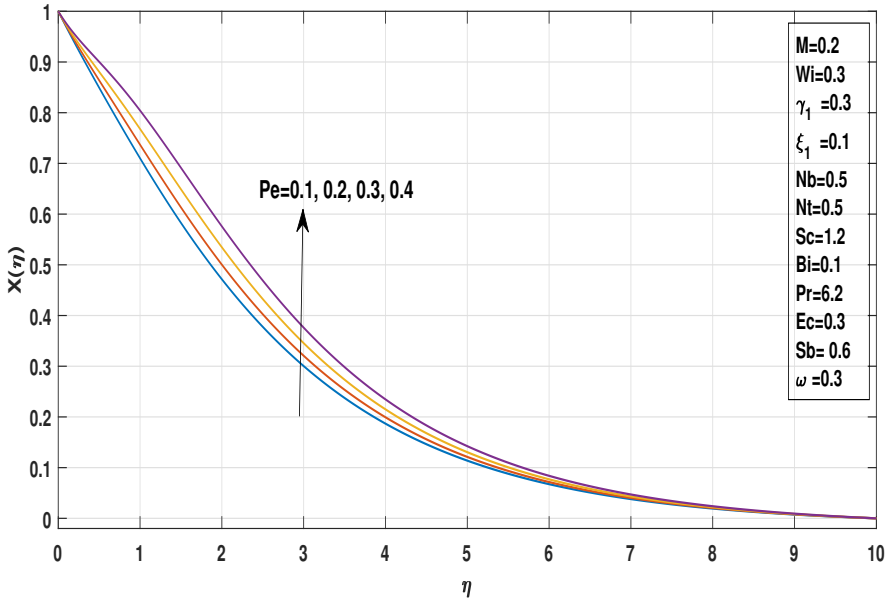

FIGURE 2.14: Influence of Pe on motile profile $X(\eta)$

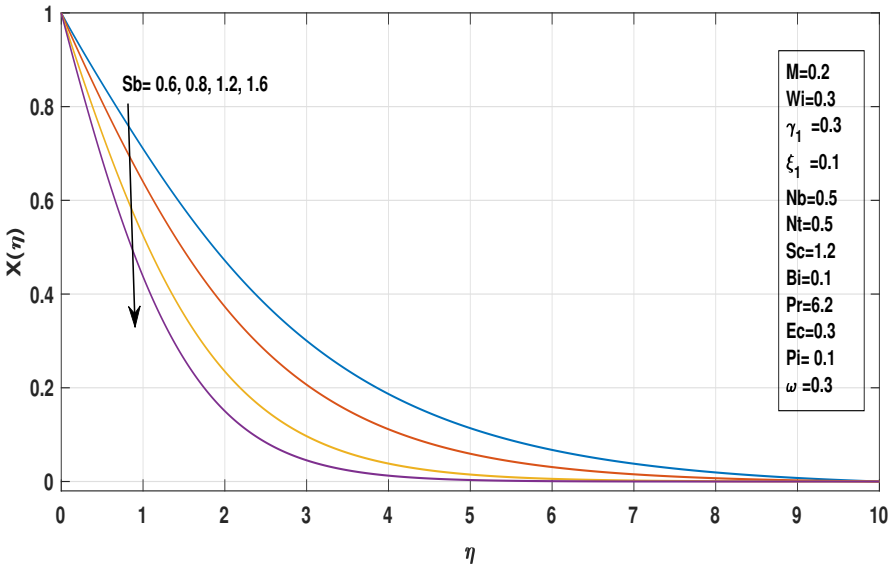

FIGURE 2.15: Influence of Sb on motile profile $X(\eta)$

Chapter 3

Radiative Effects and Motile Microorganism in Williamson Fluid Flow under Slip Boundary Conditions

3.1 Introduction

The previous chapter described the steady Williamson nanofluid flow over a stretching sheet. In this chapter, the investigation is broadened to consider unsteady flow, accounting for time-dependent variations in velocity and analyzing their effects on the nanofluid's behavior.

The impact of radiation and heat generation have been included in the temperature equation. In this chapter, a numerical analysis of the unsteady Williamson fluid flow is carried out. By applying appropriate transformations, the nonlinear PDEs are reduced to dimensionless ODEs. The resulting system is numerically solved using the shooting method.

3.2 Mathematical Modeling

This investigation focuses on the flow characteristics of a Williamson nanofluid over a stretching sheet, considering a two-dimensional, unsteady boundary layer flow. The coordinate system is defined such that the x-axis lies along the direction of the stretching sheet, while the y-axis is oriented perpendicular to the sheet, as illustrated in Figure 2.1.

The sheet is assumed to be stretched with a velocity of the form $U_w = ax/(1-ct)$, where a and c are constants. In addition, the model has been extended to include thermal radiation effects, which influence the heat transfer within the nanofluid. The governing equations now account for the combined impact of fluid motion, bioconvection and thermal radiation. The unsteady flow of the Williamson fluid is described by the following equations:

$$\frac{\partial v}{\partial y} + \frac{\partial u}{\partial x} = 0, \tag{3.1}$$

$$\frac{\partial u}{\partial t} + u\frac{\partial u}{\partial x} + \frac{\sigma B_o^2}{\rho(1-ct)}u + v\frac{\partial u}{\partial y} = \nu\left[1 + \sqrt{2}\Gamma\frac{\partial u}{\partial y}\right]\frac{\partial^2 u}{\partial y^2}, \tag{3.2}$$

$$\begin{aligned}\frac{\partial T}{\partial t} + u\frac{\partial T}{\partial x} - \frac{\sigma B_o^2}{(\rho C_p)_f}\frac{u^2}{(1-ct)} + v\frac{\partial T}{\partial y} = \frac{\nu}{(C_p)_f}\left(\frac{\partial u}{\partial y}\right)^2 + \alpha\frac{\partial^2 T}{\partial y^2} \\ + \tau\left[\frac{\partial T}{\partial y}\frac{\partial C}{\partial y}D_B + \frac{D_T}{T_\infty}\left(\frac{\partial T}{\partial y}\right)^2\right] - \frac{1}{\rho C_p}\frac{\partial q_r}{\partial y} + \frac{Q_0}{\rho C_p}(T - T_\infty),\end{aligned} \tag{3.3}$$

$$u\frac{\partial C}{\partial x} - \frac{D_T}{T_\infty}\frac{\partial^2 T}{\partial y^2} + v\frac{\partial C}{\partial y} + \frac{\partial C}{\partial t} = D_B\frac{\partial^2 C}{\partial y^2}, \tag{3.4}$$

$$\frac{\partial N}{\partial t} + v\frac{\partial N}{\partial y} + u\frac{\partial N}{\partial x} - D_N\frac{\partial^2 N}{\partial y^2} = -\frac{b_c W_c}{(C_w - C_\infty)}\frac{\partial}{\partial y}\left[N\frac{\partial C}{\partial y}\right]. \tag{3.5}$$

3.2.1 Boundary Condition

$$\left.\begin{aligned}&u = u_w + u_\gamma\frac{\partial u}{\partial y}\left(1 - u\zeta\frac{\partial u}{\partial y}\right)^{\frac{1}{2}},\ v = 0,\ -\kappa\frac{\partial T}{\partial y} = h_t(T_w - T),\\ &C = C_w,\ N = N_w,\ at\ y = 0,\\ &u \longrightarrow 0,\quad T \longrightarrow T_\infty,\quad C \longrightarrow C_\infty\quad N \longleftrightarrow N_\infty\quad as\ \ y \longrightarrow \infty.\end{aligned}\right\} \tag{3.6}$$

The radiation heat flux q_r is written as :

$$q_r = -\frac{4\tilde{\sigma}^*}{3\tilde{k}^*}\frac{\partial T^4}{\partial y}. \tag{3.7}$$

The Stefan-Boltzman constant is expressed by $\tilde{\sigma}^*$, and the absorption coefficient is expressed by $\tilde{k}^*$. In the case of a small temperature difference, the Taylor series expansion is applied to express the temperature T^4 around T_∞ as follows

$$T^4 = T_\infty^4 + 4T_\infty^3\big(T - T_\infty\big) + 6T_\infty^2\big(T - T_\infty\big)^2 + ...$$

The higher-order terms are neglected, resulting in the following expression:

$$\begin{aligned} T^4 &= T_\infty^4 + 4T_\infty^3\big(T - T_\infty\big) \\ &= 4T_\infty^3 T - 3T_\infty^4. \end{aligned}$$

By inserting the above expression into equation (3.7), we obtain:

$$\begin{aligned} q_r &= -\frac{4\tilde{\sigma}^*}{3\tilde{k}^*}\frac{\partial T^4}{\partial y} \\ &= -\frac{16T_\infty^3\tilde{\sigma}^*}{3\tilde{k}^*}\frac{\partial T}{\partial y}. \end{aligned} \tag{3.8}$$

3.3 Similarity Transformation and Non-dimensionalization of Mathematical Model

This section presents the simplification of the original mathematical model for Williamson nanofluid flow through the introduction of dimensionless variables and parameters. This transformation not only enhances our understanding of the physical behavior of the system but also facilitates the process of solving the governing equations. Using similarity transformations, the governing equations

are converted into a system of ordinary differential equations.

$$\left.\begin{aligned} \eta = y\sqrt{\frac{a}{\nu(1-ct)}},\ \ u = \frac{ax}{1-ct}F'(\eta),\ \ v = -\sqrt{\frac{a\nu}{1-ct}}F(\eta), \\ \theta(\eta) = \frac{T-T_\infty}{T_w-T_\infty},\ \ \phi(\eta) = \frac{C-C_\infty}{C_w-C_\infty},\ \ X(\eta) = \frac{N-N_\infty}{N_w-N_\infty}. \end{aligned}\right\} \tag{3.9}$$

The symbol η denotes the similarity variable. The symbols u and v are used to represent the velocity components in the x and y directions. Additionally F, θ, ϕ and x correspond to the dimensionless velocity, temperature, concentration and motile profiles, respectively. The formulation of various parameters utilized in the forthcoming ordinary differential equations (ODEs) and their boundary conditions (BCs) is shown in TABLE 3.1.

TABLE 3.1: Various dimensionless parameters considered in the governing ODEs

Symbols	**Name**	**Appearance**
Pe	Peclet number	$Pe = \frac{b_c W_c}{D_N}$
Wi	Williamson parameter	$Wi = \sqrt{2}\Gamma U_w\sqrt{\frac{a}{\nu(1-ct)}}$
He	Heat generation parameter	$He = \frac{Q}{a\rho C_p}$
Pr	Prandtl number	$Pr = \frac{\nu}{\alpha}$
N_R	Radiation parameter	$N_R = \frac{16\tilde{\sigma}^*\ T_\infty^3}{3\tilde{k}^*\nu\rho C_p K_0}$
Nt	Thermophoresis parameter	$Nt = \frac{\tau D_T(T_w-T_\infty)}{\nu T_\infty}$
Sc	Schmidt number	$Sc = \frac{\nu}{D_B}$
Ω	Motile density parameter	$\Omega = \frac{N_\infty}{(N_w-N_\infty)}$
Ec	Eckert number	$Ec = \frac{U_w^2}{(T_w-T_\infty)(Cp)_f}$
M	Magnetic field	$M = \frac{\sigma B_0^2}{a\rho}$
Sc	Schmidt number	$Sc = \frac{\nu}{D_B}$
Sb	Bioconvection parameter	$Sb = \frac{\nu}{D_N}$
Nb	Brownian motion parameter	$Nb = \frac{\tau D_B(T_w-T_\infty)}{\nu}$

3.3.1 Non-dimensionalization of Momentum Equation

In this subsection, the governing momentum equation (3.2) is transformed into a non-dimensional form. For this purpose, following partial derivatives will be

needed:

$$\frac{\partial u}{\partial x} = \frac{\partial}{\partial x}\left(F'(\eta)\frac{ax}{1-ct}\right)$$

$$\frac{\partial u}{\partial x} = \frac{a}{1-ct}F'. \tag{3.10}$$

$$\Rightarrow \quad \frac{\partial u}{\partial y} = \frac{\partial}{\partial y}\left(\frac{ax}{1-ct}F'\right)$$

$$= \frac{ax}{1-ct}F''\left(\sqrt{\frac{a}{\nu(1-ct)}}\right). \tag{3.11}$$

$$\Rightarrow \quad \frac{\partial^2 u}{\partial y^2} = \frac{\partial}{\partial y}\left(F''\frac{ax}{1-ct}\sqrt{\frac{a}{\nu(1-ct)}}\right)$$

$$= F'''\frac{a^2x}{\nu(1-ct)^2}. \tag{3.12}$$

$$\frac{\partial u}{\partial t} = \frac{\partial}{\partial t}\left(F'\frac{ax}{1-ct}\right)$$

$$= \frac{axc}{(1-ct)^2}F' + \frac{axc\eta}{2(1-ct)^2}F''. \tag{3.13}$$

Putting the values of all partial derivatives (3.10) , (3.11), (3.12) and (3.13), along with the velocity components (3.9), into equation (3.2), we get the following:

$$\frac{a^2x}{(1-ct)^2}F'^2\frac{axc}{(1-ct)^2}F' + \frac{axc\eta}{2(1-ct)^2}F'' + \frac{a^2x}{(1-ct)^2}FF''$$
$$= -\left(F'\frac{ax}{(1-ct)}\right)\frac{\sigma B_o^2}{\rho(1-ct)}$$
$$+ \nu\left[1+\sqrt{2}\Gamma\left(F''\sqrt{\frac{a}{\nu(1-ct)}}\frac{ax}{(1-ct)}\right)\right]$$
$$\left(F'''\frac{a^2x}{\nu(1-ct)^2}\right).$$

$$\Rightarrow \quad \frac{c}{a}F' + \frac{\eta c}{2a}F'' + \left(F'\right)^2 - F''F = \left[1+\sqrt{2}\Gamma\frac{ax}{(1-ct)}F''(\eta)\sqrt{\frac{a}{\nu(1-ct)}}\right]F''' - \frac{\sigma B_o^2}{a\rho}F.'$$

$$\Rightarrow \quad \epsilon F' + \frac{\eta}{2}\epsilon F'' + \left(F'\right)^2 - F''F$$

$$\Rightarrow \quad \left[1+w_iF''\right]F''' - F'^2 + F''F - MF' - \epsilon F' - \frac{\eta}{2}\epsilon F'' = 0. \tag{3.14}$$

3.3.2 Non-dimensionalization of Energy Equation

The energy equation (3.3) is transformed into a non-dimensional form for the Williamson nanofluid model. This transformation requires consideration of the following derivatives:

$$\Rightarrow \quad T = T_\infty + (T_w - T_\infty)\theta. \tag{3.15}$$

$$\Rightarrow \quad \frac{\partial T}{\partial x} = 0. \tag{3.16}$$

$$\Rightarrow \quad \frac{\partial T}{\partial t} = (T_w - T_\infty)\theta'\Big(\frac{\eta c}{2(1-ct)}\Big). \tag{3.17}$$

$$\Rightarrow \quad \frac{\partial T}{\partial y} = (T_w - T_\infty)\theta'\sqrt{\frac{a}{\nu(1-ct)}}. \tag{3.18}$$

$$\Rightarrow \quad \frac{\partial^2 T}{\partial y^2} = \frac{a}{\nu(1-ct)}(T_w - T_\infty)\theta''. \tag{3.19}$$

$$\Rightarrow \quad C = C_\infty + \phi(\eta)(C_w - C_\infty). \tag{3.20}$$

$$\Rightarrow \quad \frac{\partial C}{\partial y} = (C_w - C_\infty)\phi'\sqrt{\frac{a}{\nu(1-ct)}}. \tag{3.21}$$

$$\frac{\partial q_r}{\partial y} = -\frac{16\sigma T_\infty^3}{3K*}\left((T_w - T_\infty)\sqrt{\frac{a}{\nu(1-ct)}}\theta''\right). \tag{3.22}$$

Through the use of equations (3.17), (3.16), (3.18) ,(3.18), (3.19), (3.11) and (3.12) and velocity components u and v from (3.9) into equation (3.3), we arrive at

$$\begin{aligned}
&(T_w - T_\infty)\frac{\eta c}{2(1-ct)}\theta' + \big[-(T_w - T_\infty)\frac{a}{(1-ct)}F\theta'\big] \\
&= \alpha\left(\frac{a}{\nu(1-ct)}(T_w - T_\infty)\theta''\right) + \frac{\sigma B_o^2}{(\rho C_p)_f(1-ct)}\Big(\frac{ax}{(1-ct)}F'\Big)^2 + \frac{\nu}{C_p\nu_f}\Big(\frac{a^3x^2}{(1-ct)^3}F''\Big)^2 \\
&+ \tau\left[D_B\left((T_w - T_\infty)\sqrt{\frac{a}{\nu(1-ct)}}\theta'\right)\left((C_w - C_\infty)\sqrt{\frac{a}{\nu(1-ct)}}\phi'\right)\right. \\
&+ \frac{Q_0}{\rho C_p}(T_w - T_\infty)\theta \\
&\left.+ \frac{D_T}{T_\infty}\left((T_w - T_\infty)\sqrt{\frac{a}{\nu(1-ct)}}\theta'\right)^2\right] - \frac{1}{\rho C_p}\left[-\frac{16\sigma T_\infty^3}{3K*}(T_w - T_\infty)\theta''\frac{a}{\nu(1-ct)}\right].
\end{aligned}$$

$$\Rightarrow (T_w - T_\infty)\frac{\eta c}{2(1-ct)}\theta' - \frac{a}{(1-ct)}\big(T_w - T_\infty\big)F\theta' = \frac{a\alpha}{\nu(1-ct)}\big(T_w - T_\infty\big)\theta''$$
$$+ \frac{\sigma B_o^2 a^2 x^2}{(\rho C_p)_f (1-ct)^3}F'^2 + \frac{a^3x^2}{(C_p)_f(1-ct)^3}F''^2 + \tau\Bigg[\big(T_w - T_\infty\big)\big(C_w - C_\infty\big)\frac{aD_B}{\nu(1-ct)}\theta'\phi'$$
$$+ \frac{Q_0}{\rho C_p}(T_w - T_\infty)\theta + \frac{aD_T}{\nu T_\infty(1-ct)}\big(T_w - T_\infty\big)^2\theta'^2\Bigg] + \frac{16\sigma T_\infty^3}{3\rho C_p K^*}(T_w - T_\infty)\frac{a}{\nu(1-ct)}\theta''.$$

$$\Rightarrow \frac{\eta c}{2a}\theta' - F\theta' = \frac{\alpha}{\nu}\theta'' + \frac{ax^2\sigma B_o^2}{\big(T_w - T_\infty\big)(\rho C_p)_f(1-ct)^2}F'^2 + \frac{Q_0(1-ct)}{a\rho c_p}\theta + \frac{16\sigma T_\infty^3}{3\rho c_p K*}\theta''$$
$$+ \frac{a^2x^2}{\big(T_w - T_\infty\big)(C_p)_f(1-ct)^2}F''^2 + \tau\Bigg[\frac{D_B}{\nu}\big(C_w - C_\infty\big)\theta'\phi' + \frac{D_T}{\nu T_\infty}\big(T_w - T_\infty\big)\theta'^2\Bigg].$$

$$\Rightarrow \frac{\eta}{2}\epsilon\theta' - F\theta' = \frac{1}{Pr}\theta'' + MEc(F')^2 + Ec(F'')^2 + Nb\theta'\phi' + Nt(\theta')^2 + \frac{N_r}{P_r}\theta'' + H_e\theta.$$

$$\Rightarrow \theta'' + N_R\theta'' + Pr\Bigg[MEcF'^2 + EcF''^2 + Nb\theta'\phi' + Nt\theta'^2 + F\theta' + H_e\theta - \frac{\eta}{2}\epsilon\theta'\Bigg] = 0. \tag{3.23}$$

3.3.3 Non-dimensionalization of Concentration Equation

In this sub-section, we concentrate on the non-dimensionalization process specifically applied to the concentration equation (3.4) within our Williamson nanofluid model. To achieve this, we will also need to consider the following derivatives:

$$\frac{\partial C}{\partial x} = 0. \tag{3.24}$$

$$\frac{\partial^2 C}{\partial y^2} = \phi''\frac{a}{\nu(1-ct)}\big(C_w - C_\infty\big). \tag{3.25}$$

$$\frac{\partial C}{\partial t} = \phi'\big(C_w - C_\infty\big)\frac{\eta c}{2(1-ct)}. \tag{3.26}$$

Utilizing (3.24), (3.25), (3.21), (3.19) and (3.26) in equation(3.4), we obtain:

$$\Rightarrow \frac{\eta c}{2(1-ct)}\big(C_w - C_\infty\big)\phi' - \frac{a}{(1-ct)}\big(C_w - C_\infty\big)\phi' F = D_B$$
$$\Bigg(\frac{a}{\nu(1-ct)}\big(C_w - C_\infty\big)\phi''\Bigg) + \frac{D_T}{T_\infty}\Bigg(\big(T_w - T_\infty\big)\frac{a}{\nu(1-ct)}\theta''\Bigg).$$

$$\Rightarrow \frac{\eta}{s}S_c\epsilon\phi' - S_c\phi' F = \phi'' + \frac{N_t}{N_b}\theta''.$$

$$\Rightarrow \phi'' + (F - \frac{\eta}{2}\epsilon)S_c\phi' + \frac{N_t}{N_b}\theta'' = 0. \tag{3.27}$$

3.3.4 Non-dimensionalization of Motile Equation

To derive the dimensionless form of the motile equation, the following differential terms will be utilized:

$$\Rightarrow \quad N = N_\infty + (N_w - N_\infty)X. \tag{3.28}$$

$$\Rightarrow \quad \frac{\partial N}{\partial x} = 0. \tag{3.29}$$

$$\Rightarrow \quad \frac{\partial N}{\partial y} = \big(N_w - N_\infty\big)\sqrt{\frac{a}{\nu(1-ct)}}X'. \tag{3.30}$$

$$\Rightarrow \quad \frac{\partial^2 N}{\partial y^2} = \frac{a}{\nu(1-ct)}\big(N_w - N_\infty\big)X''. \tag{3.31}$$

$$\Rightarrow \quad \frac{\partial N}{\partial t} = \big(N_w - N_\infty\big)\frac{\eta c}{2(1-ct)}X'. \tag{3.32}$$

Inserting equations (3.21), (3.29), (3.30), (3.32) and (3.31) into equation (3.5) leads to:

$$\begin{aligned}
&\big(N_w - N_\infty\big)\frac{\eta c}{2(1-ct)}X' + \left[\left(- \sqrt{\frac{a\nu}{(1-ct)}}F\right)\left(N_w - N_\infty\right)\sqrt{\frac{a}{\nu(1-ct)}}X'\right] \\
&= \frac{a}{\nu(1-ct)}D_N\big(N_w - N_\infty\big)X'' - \frac{b_c W_c}{(C_w - C_\infty)} \\
&\frac{\partial}{\partial y}\left[\left(N_\infty + (N_w - N_\infty)X\right)\left((C_w - C_\infty)\sqrt{\frac{a}{\nu(1-ct)}}\phi'\right)\right].
\end{aligned}$$

$$\begin{aligned}
\Rightarrow\ &\big(N_w - N_\infty\big)\frac{\eta c}{2(1-ct)}X' - \big(N_w - N_\infty\big)\frac{a}{(1-ct)}X'F = \frac{a}{\nu(1-ct)}D_N \\
&\big(N_w - N_\infty\big)X'' - \frac{b_c W_c}{(C_w - C_\infty)}\left[\frac{a}{\nu(1-ct)}\big(N_w - N_\infty\big)\big(C_w - C_\infty\big)\right. \\
&\left.\big(X\phi'' + \phi'X'\big) + \frac{a}{\nu(1-ct)}N_\infty(C_w - C_\infty)\phi''\right].
\end{aligned}$$

$$\Rightarrow \quad \frac{\eta\nu c}{2aD_N}X' - \frac{\nu}{D_N}F(\eta)X' = X'' - \frac{b_c W_c}{D_N}\left[X\phi'' + \phi'X' + \frac{N_\infty}{N_w - N_\infty}\phi''\right].$$

$$\Rightarrow \quad \frac{\eta}{2}\epsilon S_b X' - S_b F X' = X'' - Pe\left[X\phi'' + \phi'X' + \Omega\phi''\right].$$

$$\Rightarrow \quad X'' + S_b F X' - \frac{\eta}{2}\epsilon S_b X' - Pe\left[(\Omega + X)\phi'' + \phi' X'\right] = 0. \tag{3.33}$$

3.3.5 Dimensionless form of Boundary Conditions

The corresponding boundary conditions are transformed into a non-dimensional format through the following method:

- $u = u_w + u_\gamma \dfrac{\partial u}{\partial y}\left(1 - u_\zeta \dfrac{\partial u}{\partial y}\right)^{-\frac{1}{2}}, \qquad at \quad y = 0.$

$$\Rightarrow \quad \frac{ax}{1-ct}F' = \frac{ax}{1-ct} + \gamma_0\sqrt{x}\left(\frac{ax}{1-ct}F''\sqrt{\frac{a}{\nu}}\right)\left(1 - \zeta_0\sqrt{x}\frac{ax}{1-ct}F''\sqrt{\frac{a}{\nu}}\right)^{-\frac{1}{2}}, \quad at \quad \eta = 0.$$

$$\Rightarrow \quad F' = 1 + \gamma_1 \left(\frac{F''}{\sqrt{1 - F''_1}}, \right) \qquad at \quad \eta = 0.$$

- $v = 0, \qquad at \quad y = 0.$

$$\Rightarrow \quad -\sqrt{\frac{a\nu}{(1-ct)}}F = 0, \qquad at \quad \eta = 0.$$

$$\Rightarrow \quad F = 0, \qquad at \quad \eta = 0.$$

- $-k\dfrac{\partial T}{\partial y} = h_t\big(T_w - T\big), \qquad at \quad y = 0.$

$$\Rightarrow \quad -k\big(T_w - T_\infty\big)\theta'\sqrt{\frac{a}{\nu(1-ct)}} = h_t\big(T_w - T_\infty - (T_w - T_\infty)\big)\theta, \qquad at \quad \eta = 0.$$

$$\Rightarrow \quad \theta' = \frac{h_t}{k}\sqrt{\frac{a}{\nu(1-ct)}}\big(1-\theta\big), \qquad at \quad \eta = 0.$$

$$\Rightarrow \quad \theta' = B_i\big(1-\theta\big), \qquad at \quad \eta = 0.$$

- $C = C_w, \qquad at \quad y = 0.$

$$\Rightarrow \quad \big(C_w - C_\infty\big)\phi + C_\infty = C_w, \qquad at \quad \eta = 0.$$

$$\Rightarrow \quad \phi = \frac{C_w - C_\infty}{C_w - C_\infty}, \qquad at \quad \eta = 0.$$

$$\Rightarrow \quad \phi = 1, \qquad at \quad \eta = 0.$$

- $N = N_w, \qquad at \quad y = 0.$

$$\Rightarrow \quad \big(N_w - N_\infty\big)X + N_\infty = N_w, \qquad at \quad \eta = 0.$$

$$\Rightarrow \quad X = \frac{N_w - N_\infty}{N_w - N_\infty}, \qquad at \quad \eta = 0.$$

$$\Rightarrow \quad X = 1, \qquad at \quad \eta = 0.$$

- $u \longrightarrow 0, \qquad as \quad y \longrightarrow \infty.$

$$\Rightarrow \quad F' \frac{ax}{(1-ct)}, \longrightarrow 0 \qquad as \quad \eta \longrightarrow \infty.$$

$$\Rightarrow \quad F' \longrightarrow 0, \qquad as \quad \eta \longrightarrow \infty.$$

- $T \longrightarrow T_\infty, \qquad as \quad y \longrightarrow \infty.$

$$\Rightarrow \quad \big(T_w - T_\infty\big)\theta + T_\infty \longrightarrow T_\infty, \qquad as \quad \eta \longrightarrow \infty.$$

$$\Rightarrow \quad \theta\big(T_w - T_\infty\big) \longrightarrow 0, \qquad as \quad \eta \longrightarrow \infty.$$

$$\Rightarrow \quad \theta \longrightarrow 0, \qquad as \quad \eta \longrightarrow \infty.$$

- $C \longrightarrow C_\infty, \qquad as \quad y \longrightarrow \infty.$

$$\Rightarrow \quad \big(C_w - C_\infty\big)\phi(\eta) + C_\infty \longrightarrow C_\infty, \qquad as \quad \eta \longrightarrow \infty.$$

$$\Rightarrow \quad \big(C_w - C_\infty\big)\phi \longrightarrow 0, \qquad as \quad \eta \longrightarrow \infty.$$

$$\Rightarrow \quad \phi \longrightarrow 0, \qquad as \quad \eta \longrightarrow \infty.$$

- $N \longrightarrow N_\infty, \qquad as \quad y \longrightarrow \infty.$

$$\Rightarrow \quad X\big(N_w - N_\infty\big) + N_\infty \longrightarrow N_\infty, \qquad as \quad \eta \longrightarrow \infty.$$

$$\Rightarrow \quad X\big(N_w - N_\infty\big) \longrightarrow 0, \qquad as \quad \eta \longrightarrow \infty.$$

$$\Rightarrow \quad X \longrightarrow 0, \qquad as \quad \eta \longrightarrow \infty.$$

3.3.6 Non-dimensionalization of Physical Quantities

The present sub-section of this thesis highlights four key parameters: the skin friction, the Nusselt number, the motile density number and the Sherwood number. This section offers an overview of these dimensionless quantities along with their

mathematical formulations.

3.3.6.1 Skin Friction

$$C_f = \frac{\mu\left[\left(\frac{\partial u}{\partial y}\right)_{y=0} + \frac{\Gamma}{\sqrt{2}}\left(\frac{\partial u}{\partial y}\right)^2_{y=0}\right]}{\rho_f u_w^2}$$

$$= \frac{\mu\left[\frac{ax}{(1-ct)}F''(0)\sqrt{\frac{a}{\nu(1-ct)}} + \frac{\Gamma}{\sqrt{2}}\left(F''(0)\frac{ax}{(1-ct)}\sqrt{\frac{a}{\nu(1-ct)}}\right)^2\right]}{\rho_f\left(\frac{ax}{(1-ct)}\right)^2}$$

$$= \frac{\mu\sqrt{\frac{a}{\nu(1-ct)}}\left[\frac{\Gamma\sqrt{2}}{2}\frac{ax}{(1-ct)}F''(0)^2\sqrt{\frac{a}{\nu(1-ct)}} + F''(0)\right]}{\rho_f\frac{ax}{(1-ct)}}$$

$$= \frac{\mu\sqrt{\frac{a}{\nu(1-ct)}}\left[F''(0) + \frac{Wi}{2}F''(0)^2\right]}{\rho_f\frac{ax}{(1-ct)}}$$

$$= \frac{\frac{\nu(1-ct)}{ax}\left[F''(0) + \frac{Wi}{2}F''(0)^2\right]\sqrt{\frac{a}{\nu(1-ct)}}}{\rho_f ax}$$

$$C_f\sqrt{Re_x} = F''(0) + \frac{Wi}{2}F''(0)^2. \tag{3.34}$$

where the Re_x is defined as $\left(Re_x\right)^{\frac{1}{2}} = \sqrt{\frac{a}{\nu(1-ct)}}x$.

3.3.6.2 Nusslt Number

$$Nu_x = \frac{-kx\left(\frac{\partial T}{\partial y}\right)_{y=0}}{k(T_w - T_\infty)}$$

$$= \frac{-x(T_w - T_\infty)\sqrt{\frac{a}{\nu(1-ct)}}\theta'(0)}{(T_w - T_\infty)}$$

$$= -x\sqrt{\frac{a}{\nu(1-ct)}}\theta'(0).$$

$$\Rightarrow \frac{Nu_x}{x\sqrt{\frac{a}{\nu(1-ct)}}} = -\theta'(0).$$

$$\Rightarrow \frac{Nu_x}{\sqrt{Re_x}} = \theta'(0). \tag{3.35}$$

3.3.6.3 Sherwood Number

$$Sh_x = \frac{-D_B x\left(\frac{\partial C}{\partial y}\right)_{y=0}}{D_B(C_w - C_\infty)}$$

$$= \frac{-x(C_w - C_\infty)\sqrt{\frac{a}{\nu(1-ct)}}\phi'(0)}{(C_w - C_\infty)}$$

$$= -x\phi'(0)\sqrt{\frac{a}{\nu(1-ct)}}.$$

$$\Rightarrow \frac{Sh_x}{x\sqrt{\frac{a}{\nu(1-ct)}}} = -\phi'(0).$$

$$\Rightarrow \quad \frac{Sh_x}{\sqrt{Re_x}} = \phi'(0). \tag{3.36}$$

3.3.6.4 Motile Density Number

$$Nn_x = \frac{-D_N x\left(\frac{\partial N}{\partial y}\right)_{y=0}}{D_N(N_w - N_\infty)}$$

$$= \frac{-x(N_w - N_\infty)\sqrt{\frac{a}{\nu(1-ct)}}X'(0)}{(N_w - N_\infty)}$$

$$= -x\sqrt{\frac{a}{\nu(1-ct)}}X'(0).$$

$$\Rightarrow \frac{Nn_x}{x\sqrt{\frac{a}{\nu(1-ct)}}} = -X'(0).$$

$$\Rightarrow \quad \frac{Nn_x}{\sqrt{Re_x}} = X'(0). \tag{3.37}$$

3.4 Solution Framework

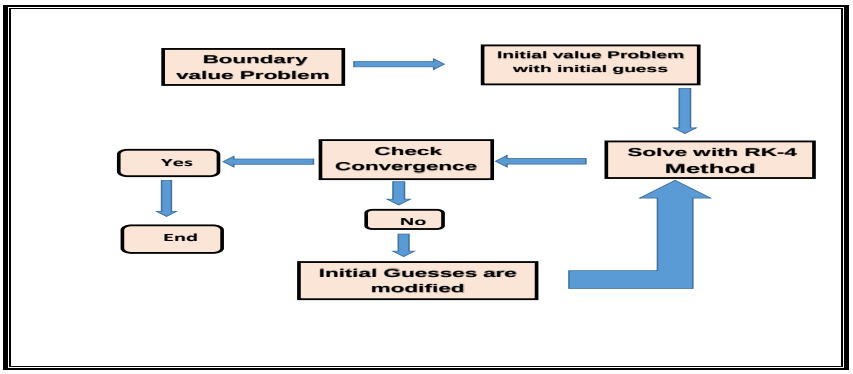

FIGURE 3.1: The shooting methods methodological framework

To compute the numerical solutions, the shooting method is applied, involving the use of the RK4 method. The solution algorithm of the shooting method, is explained and shown in Figure 3.2. In order to solve the ODE of the momentum equation (3.14), the listed notations are adopted, as an initial step:

$$F = \widetilde{K}_1, \qquad F' = \widetilde{K}_1' = \widetilde{K}_2, \qquad F'' = \widetilde{K}_2' = \widetilde{K}_3.$$

The momentum equation is reformulated as the following system of first-order ODEs:

$$\widetilde{K}_1 = \widetilde{K}_2, \qquad \widetilde{K}_1(0) = 0.$$

$$\widetilde{K}_2 = \widetilde{K}_3, \qquad \widetilde{K}_2(0) = 1+\gamma_1\left[\frac{\widetilde{K}_3(0)}{\sqrt{1-\zeta_1\widetilde{K}_3(0)}}\right].$$

$$\widetilde{K}_3 = \left(\widetilde{K}_2^2-\widetilde{K}_1\widetilde{K}_3+(M+\epsilon)\widetilde{K}_2+\frac{\eta}{2}\epsilon\widetilde{K}_3\right)\frac{1}{1+Wi\widetilde{K}_3}, \qquad \widetilde{K}_3(0) = \mathcal{U}.$$

Use the Runge-Kutta 4th order method for the numerical solution of above IVP. The missing condition U must be chosen such that:

$$\widetilde{K}_2\big(\eta_\infty, \mathcal{U}\big) = 0.$$

The value of $\mathcal{U}$ is determined through Newton's method, which proceeds according to the iterative scheme given below:

$$\mathcal{U}^{(n+1)} = \mathcal{U}^{(n)} - \frac{\widetilde{K}_2\big(\eta_\infty, \mathcal{U}^{(n)}\big)}{\left(\frac{\partial}{\partial \mathcal{U}}\widetilde{K}_2\big(\eta_\infty, \mathcal{U}\big)\right)^{(n)}}.$$

The following derivatives are required to implement the iterative scheme described above:

$$\frac{\partial \widetilde{K}_1}{\partial \mathcal{U}} = \widetilde{K}_4, \qquad \frac{\partial \widetilde{K}_2}{\partial \mathcal{U}} = \widetilde{K}_5, \qquad \frac{\partial \widetilde{K}_3}{\partial \mathcal{U}} = \widetilde{K}_6.$$

Thus, with these new notations, the Newton's iterative scheme can be expressed as:

$$\mathcal{U}^{(n+1)} = \mathcal{U}^{(n)} - \frac{\widetilde{K}_2\big(\eta_\infty, \mathcal{U}^{(n)}\big)}{\widetilde{K}_5\big(\eta_\infty, \mathcal{U}^{(n)}\big)}.$$

Next, the system of first-order ODEs is differentiated with respect to $\mathcal{U}$, resulting in a new system of ODEs, as shown below:

$$\widetilde{K}_4 = \widetilde{K}_5, \qquad \widetilde{K}_4(0) = 0.$$

$$\widetilde{K}_5 = \widetilde{K}_6, \qquad \widetilde{K}_5(0) = \frac{\gamma_1}{\sqrt{1-\zeta_1 \mathcal{U}}} + \frac{\gamma_1 \mathcal{U} \zeta_1}{2\big(1-\zeta_1 \mathcal{U}\big)^{\frac{3}{2}}}.$$

$$\widetilde{K}_6 = \Big[\big(1+Wi\widetilde{K}_3\big)\big(2\widetilde{K}_2\widetilde{K}_5 - \widetilde{K}_1\widetilde{K}_6 - \widetilde{K}_3\widetilde{K}_4 + M\widetilde{K}_5\big) - Wi\widetilde{K}_6\big(\widetilde{K}_2^2 - \widetilde{K}_1\widetilde{K}_3 + M\widetilde{K}_2\big)\Big]\frac{1}{\big(1+Wi\widetilde{K}_3\big)^2}, \qquad \widetilde{K}_6(0) = 1.$$

Newton's iterative scheme terminates when the following condition is met:

$$\left|\widetilde{K}_2\big(\eta_\infty, \mathcal{U}^n\big)\right| < \epsilon_1.$$

Now, we solve (3.23) and (3.27) numerically via the shooting method assuming F, F' and F'' as a specified functions. The notations employed in the implementation are listed below:

$$\theta = \widetilde{L}_1, \qquad \theta' = \widetilde{L}_1' = \widetilde{L}_2, \qquad \phi = \widetilde{L}_3, \qquad \phi' = \widetilde{L}_3' = \widetilde{L}_4.$$

The equations (3.23) and (3.27) are transformed into the following first order ODEs system:

$$\widetilde{L}_1' = \widetilde{L}_2, \qquad \widetilde{L}_1(0) = V,$$

$$\widetilde{L}_2' = -Pr\Big[F\widetilde{L}_2 + EcF''^2 + MEcF'^2 + Nb\widetilde{L}_2\widetilde{L}_4 + Nt\widetilde{L}_2^2 + He\widetilde{L}_1 - \frac{\eta}{2}\epsilon\widetilde{L}_2\Big]\frac{1}{1+N_R}, \qquad \widetilde{L}_2(0) = -Bi(1-\widetilde{L}_1),$$

$$\widetilde{L}_3' = \widetilde{L}_4, \qquad \widetilde{L}_3(0) = 1,$$

$$\widetilde{L}_4' = -(F-\frac{\eta}{2})Sc\widetilde{L}_4 + Pr\frac{Nt}{Nb}\Big[F\widetilde{L}_2 + EcF''^2 + MEcF'^2 + Nb\widetilde{L}_2\widetilde{L}_4 + Nt\widetilde{L}_2^2 + He\widetilde{L}_1 - \frac{\eta}{2}\epsilon\widetilde{L}_2\Big]\frac{1}{1+N_R}, \qquad \widetilde{L}_4(0) = W.$$

The RK-4 method has been applied to solve the above IVP. The missing conditions V and W should be chosen such that .

$$\widetilde{L}_1\big(\eta_\infty, V, W\big) = 0, \qquad \widetilde{L}_3\big(\eta_\infty, V, W\big) = 0.$$

The unknowns V and W, are determined using Newton's method via the following iterative scheme:

$$\begin{bmatrix} V \\ W \end{bmatrix}^{(n+1)} = \begin{bmatrix} V \\ W \end{bmatrix}^{(n)} - \left(\begin{bmatrix} \frac{\partial \widetilde{L}_1}{\partial V} & \frac{\partial \widetilde{L}_1}{\partial W} \\ \frac{\partial \widetilde{L}_3}{\partial V} & \frac{\partial \widetilde{L}_3}{\partial W} \end{bmatrix}^{-1}\right)^{(n)} \begin{bmatrix} \widetilde{L}_1 \\ \widetilde{L}_3 \end{bmatrix}^{(n)}$$

Let us introduce the following notation:

$$\frac{\partial \widetilde{L}_1}{\partial V} = \widetilde{L}_5, \quad \frac{\partial \widetilde{L}_2}{\partial V} = \widetilde{L}_6, \quad \frac{\partial \widetilde{L}_3}{\partial V} = \widetilde{L}_7, \quad \frac{\partial \widetilde{L}_4}{\partial V} = \widetilde{L}_8,$$
$$\frac{\partial \widetilde{L}_1}{\partial W} = \widetilde{L}_9, \quad \frac{\partial \widetilde{L}_2}{\partial W} = \widetilde{L}_{10}, \quad \frac{\partial \widetilde{L}_3}{\partial W} = \widetilde{L}_{11}, \quad \frac{\partial \widetilde{L}_4}{\partial W} = \widetilde{L}_{12}.$$

Rewriting the Newton's iterative scheme with the new notation, we get:

$$\begin{bmatrix} V \\ W \end{bmatrix}^{(n+1)} = \begin{bmatrix} V \\ W \end{bmatrix}^{(n)} - \left(\begin{bmatrix} \widetilde{L}_5 & \widetilde{L}_9 \\ \widetilde{L}_7 & \widetilde{L}_{11} \end{bmatrix}^{-1} \right)^{(n)} \begin{bmatrix} \widetilde{L}_1 \\ \widetilde{L}_3 \end{bmatrix}^{(n)}$$

By differentiating the system of last four first-order ODEs with respect to V and W, we obtain another system of ODEs, as shown below:

$$\begin{aligned}
\widetilde{L}_5' =& \widetilde{L}_6, && \widetilde{L}_5(0) = 1,\\
\widetilde{L}_6' =& - Pr\Big[F\widetilde{L}_6 + Nb\big(\widetilde{L}_6\widetilde{L}_4 + \widetilde{L}_2\widetilde{L}_8\big) + 2Nt\widetilde{L}_2\widetilde{L}_6 \\
&+ He\widetilde{L}_5 - \frac{\eta}{2}\epsilon\widetilde{L}_6\Big]\frac{1}{1+N_R}, && \widetilde{L}_6(0) = -Bi\widetilde{L}_5,\\
\widetilde{L}_7' =& \widetilde{L}_8, && \widetilde{L}_7(0) = 0,\\
\widetilde{L}_8' =& - (F - \frac{\eta}{2})Sc\widetilde{L}_8 + Pr\frac{Nt}{Nb}\Big[F\widetilde{L}_6 + Nb\big(\widetilde{L}_6\widetilde{L}_4 + \widetilde{L}_2\widetilde{L}_8\big) \\
&+ 2Nt\widetilde{L}_2\widetilde{L}_6 + He\widetilde{L}_5 - \frac{\eta}{2}\epsilon\widetilde{L}_6\Big]\frac{1}{1+N_R}, && \widetilde{L}_8(0) = 0,\\
\widetilde{L}_9' =& \widetilde{L}_{10}, && \widetilde{L}_9(0) = 0,\\
\widetilde{L}_{10}' =& \Big[F\widetilde{L}_{10} + Nb\big(\widetilde{L}_{10}\widetilde{L}_4 + \widetilde{L}_2\widetilde{L}_{12}\big)\Big] + \\
&- \frac{Pr}{1+N_R}\Big[2Nt\widetilde{L}_2\widetilde{L}_{10} + He\widetilde{L}_9 - \frac{\eta}{2}\epsilon\widetilde{L}_{10}\Big], && \widetilde{L}_{10}(0) = -Bi\widetilde{L}_9,\\
\widetilde{L}_{11}' =& \widetilde{L}_{12}, && \widetilde{L}_{11}(0) = 0,\\
\widetilde{L}_{12}' =& - (F - \frac{\eta}{2}\epsilon)Sc\widetilde{L}_{12} + \frac{Nt}{Nb}Pr\Big[F\widetilde{L}_{10} + Nb\big(\widetilde{L}_{10}\widetilde{L}_4 + \widetilde{L}_2\widetilde{L}_{12}\big) + 2Nt\widetilde{L}_2\widetilde{L}_{10} \\
&+ He\widetilde{L}_9 - \frac{\eta}{2}\epsilon\widetilde{L}_{10}\Big]\frac{1}{1+N_R}, && \widetilde{L}_{12}(0) = 1.
\end{aligned}$$

The stopping criterion for Newton's method is set as:

$$max\Big\{\big|\widetilde{L}_1\big(\eta_\infty, V^n, W^n\big)\big|, \big|\widetilde{L}_3\big(\eta_\infty, V^n, W^n\big)\big|\Big\} < \epsilon_1,$$

Now solve the Motile equation (3.33) using the shooting method, assuming that θ, θ', ϕ, ϕ', F, F' and F'' are known functions. The shooting method is applied

using the following notation:

$$X(\eta) = \widetilde{j}_1, \qquad X'(\eta) = \widetilde{j}_1' = \widetilde{J}_2.$$

The motile equation is expressed below as a system of ODE:

$$\widetilde{j}_1' = \widetilde{j}_2, \qquad \widetilde{j}_1(0) = 1,$$

$$\widetilde{j}_2' = -SbF\widetilde{j}_2 - \frac{\eta}{2}\epsilon Sb\widetilde{j}_2 + P_e\phi'\widetilde{j}_2 - P_e(\Omega + \widetilde{j}_1)(F - \frac{\eta}{2}\epsilon)Sc\phi' + Pe\big(\widetilde{j}_1 + \Omega\big)\frac{Nt}{Nb}$$

$$\left[- Pr\big(Nt\theta'^2 + F\theta' + EcF''^2 + He\theta + MEcF' + Nb\theta'\phi' - \frac{\eta}{2}\epsilon\theta'\big)\right], \quad \widetilde{j}_2(0) = G.$$

To numerically solve the previously mentioned initial value problem (IVP) using the Runge–Kutta (RK-4) method, it is essential to carefully select the missing condition G in the system of equations. This condition G must be adjusted to ensure that the solution meets the specified boundary conditions:

$$\left|\widetilde{j}_1\big(\eta_\infty, G\big)\right| = 0.$$

Newton's method will be utilized to compute G through the following iterative process:

$$\widetilde{j}_1^{(n+1)} = \widetilde{j}_1^{(n)} - \frac{\widetilde{j}_1\big(\eta_\infty, G^{(n)}\big)}{\frac{\partial}{\partial G}\big(\widetilde{j}_1(\eta_\infty, G)\big)^{(n)}}.$$

Now introduce the following notations:

$$\frac{\partial\widetilde{j}_1}{\partial G} = \widetilde{j}_3, \qquad \frac{\partial\widetilde{j}_2}{\partial G} = \widetilde{j}_4.$$

Using these new notations, the iteration scheme for Newton's method can be formulated as follows:

$$\widetilde{j}_1^{(n+1)} = \widetilde{j}_1^{(n)} - \frac{\widetilde{j}_1\big(\eta_\infty, G^{(n)}\big)}{\widetilde{j}_3\big(\eta_\infty, G^{(n)}\big)}.$$

By taking the derivative of the system of two first-order ODEs with respect to G,

we derive a new system of ODEs, which is presented as follows:

$$\widetilde{j}_3' = \widetilde{j}_4, \qquad \widetilde{j}_3(0) = 0,$$

$$\widetilde{j}_4' = -SbF\widetilde{j}_4 + \frac{\eta}{2}\epsilon SbF\widetilde{j}_4 + P_e\phi'\widetilde{j}_4 - Pe\widetilde{j}_3\frac{Nt}{Nb}\Bigg[-Pr\big(F\theta' + EcF''^2 + MEcF' + Nb\theta'\phi' + Nt\theta'^2 + He\theta - \frac{\eta}{2}\epsilon\theta'\big)\Bigg]\frac{1}{1+N_R} - P_e\widetilde{j}_3 Sc\phi'(F - \frac{\eta}{2}\epsilon),\ \widetilde{j}_4(0) = 1.$$

The stopping criterion for the iterative scheme is established as:

$$\left|\widetilde{j}_1\big(\eta_\infty, G\big)\right| < \epsilon_1.$$

3.5 Result Interpretation

Once the fluid flow PDEs are transformed into ODEs, various important parameters become apparent. The effects of these physical parameters on the distributions of $F'(\eta)$, $\theta(\eta)$, $\phi(\eta)$ and $X(\eta)$ are thoroughly examined using the graphical representations. A detailed exploration of the importance and interpretations of each parameter is included, along with a comprehensive overview of the results obtained from the study.

3.5.1 Analysis of Computational Results

In this investigation, the influence of different physical parameters on the coefficient of skin friction, local Nusselt number, local Sherwood number and motile density number is examined. Table 3.2 shows that for an increase in the Williamson parameter Wi up to 66.6% leads to an increase of 6.9% in $C_f\sqrt{Re_x}$, whereas an increase in the unsteady parameter ϵ up to 2.6%, the skin friction coefficient $C_f\sqrt{Re_x}$ decreases. In table 3.3, the impact of key parameters on the $\frac{Nu_x}{\sqrt{Re_x}}$ and the $\frac{Sh_x}{\sqrt{Re_x}}$ is analyzed. An increasing trend is observed in the $\frac{Nu_x}{\sqrt{Re_x}}$, while a decreasing trend is noticed in the $\frac{Sh_x}{\sqrt{Re_x}}$ as the values of Nb and Nr increase. When the M increases by 50%, the $\frac{Nu_x}{\sqrt{Re_x}}$ and $\frac{Sh_x}{\sqrt{Re_x}}$ increase by 19.5% and 1.6%, respectively,

due to the Lorentz force enhancing heat and mass transfer near the surface. Table 3.4 shows the effect of Sb, Pe and Ω on motile microorganism $\frac{Nn_x}{\sqrt{Re_x}}$. The motile density number decreases from 4.6 to 3.9% as the Peclet number Pe increases from 14.2 to 20%. With an increase in the motile density parameter Ω up to 16.7%, the motile number decreases by 3.9%. Additionally, increasing the bio-convection Schmidt number Sb up to 50% results in a decrease in the motile number from 23.7 to 18.3%.

TABLE 3.2: The numerical results of $C_f\sqrt{Re_x}$ for various values of Wi, M, γ_1 , ϵ and ξ_1.

Wi	M	γ_1	ξ_1	ϵ	$C_f\sqrt{Re_x}$
0.3	0.2	0.1	0.1	0.1	-0.91231
0.2					-0.93801
0.5					-0.84886
0.6					-0.80668
	0.4				-0.97171
	0.5				-0.99917
	0.6				-1.02534
		0.2			-0.81214
		0.3			-0.73446
		0.4			-0.67196
			0.3		-0.92245
			0.5		-0.93067
			0.7		-0.93750
				0.2	-0.93472
				0.3	-0.95659
				0.05	-0.90092

TABLE 3.3: The results of the $\frac{Nu_x}{\sqrt{Re_x}}$ and $\frac{Sh_x}{\sqrt{Re_x}}$ for various values of Ec, Nb, Sc, Nt and Bi when $Pr = 6$,$Wi = 0.3$, $\gamma_1 = 0.1$ and $\xi_1 = 0.4$.

ϵ	H_e	M	Ec	Nb	Nt	N_R	Sc	B_i	$\frac{Nu_x}{\sqrt{Re_x}}$	$\frac{Sh_x}{\sqrt{Re_x}}$
0.05	0.1	0.2	0.3	0.05	0.01	0.2	1.2	0.3	0.11030	0.56906
0.1									0.10099	0.53475
0.15									0.09005	0.49082
0.17									0.08524	0.46871
	1.5								0.09057	0.57502
	0.2								0.06490	0.58273
	0.25								0.02991	0.59318
		0.3							0.09424	0.55983
		0.4							0.07857	0.55093
		0.5							0.06322	0.54233
			0.6						-0.01777	0.60985
			0.9						-0.14654	0.65082
			1.2						-0.27599	0.69195
				0.1					0.10007	0.56826
				0.15					0.08899	0.56806
				0.2					0.07698	0.56802
					0.03				0.10868	0.57937
					0.06				0.10617	0.59821
					0.09				0.10354	0.62130
						0.4			0.11263	0.56694
						0.6			0.11399	0.56532
						0.8			0.11468	0.56404
							1.3		0.10984	0.60354
							1.4		0.10941	0.63678
							1.5		0.10901	0.66889
								0.6	0.18243	0.55812
								0.8	0.21807	0.55272
								0.9	0.23325	0.55042

TABLE 3.4: The results of $\frac{Nn_x}{\sqrt{Re_x}}$ for values of Sb, ϵ, Pe and ω when $M = 0.2$, $Wi = \gamma_1 = Ec = Bi = 0.3$, $Nb = 0.05$, $Nr = 0.2$, $He = 0.1$, $Nt = 0.01$, $Sc = 1.2$, $Pr = 6.$ and $\xi_1 = 0.4$.

Sb	ϵ	Pe	Ω	$\frac{Nn_x}{\sqrt{Re_x}}$
0.5	0.05	0.2	0.6	0.98807
0.6				1.03315
0.7				1.07663
0.8				1.11824
	0.1			1.32059
	0.13			1.49829
	0.15			1.60818
		0.3		1.31365
		0.4		1.62523
		0.5		1.92260
			0.7	1.02950
			0.8	1.07092
			0.9	1.11234

3.5.2 Velocity Profile

Analyzing the velocity distributions is fundamental to exploring the characteristics and complexities of fluid flow. The motion of fluids is subject to the effect of external forces, among which magnetic fields play a significant role. In Figure 3.2, effect of M on the velocity profile is illustrated. A negative effect was observed for Williamson nanofluid, indicating that velocity distribution decreases as the magnetic field strength increases. It occurs when a magnetic field interacts with a moving fluid, causing the particles to experience a resistive force that opposes and slows the flow known as the Lorentz force.

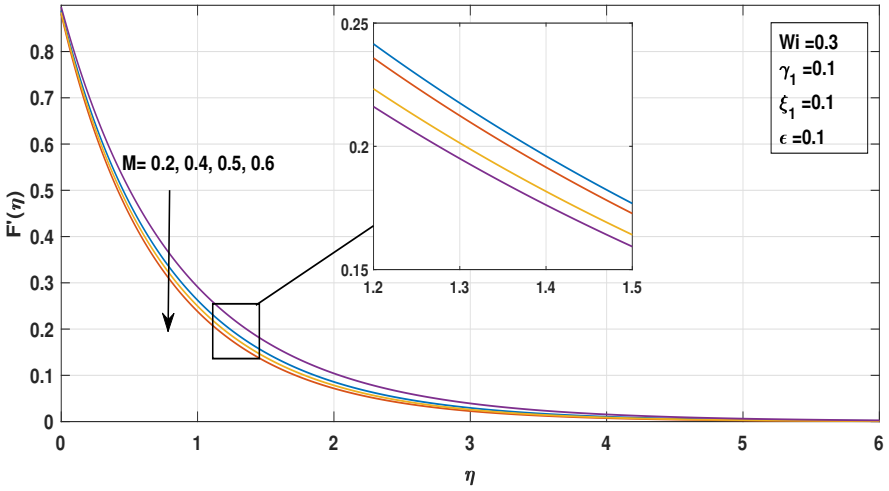

FIGURE 3.2: Impact of M on velocity profile $F'(\eta)$

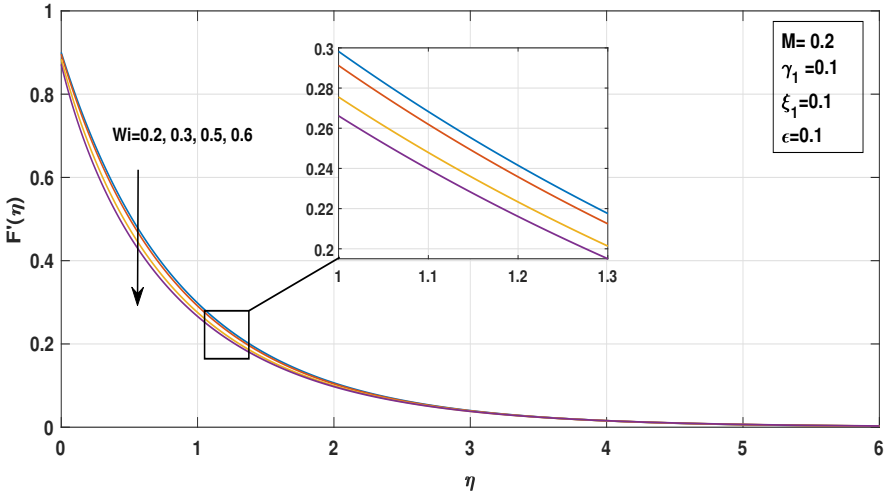

FIGURE 3.3: Effect of Wi on the velocity profile $F'(\eta)$

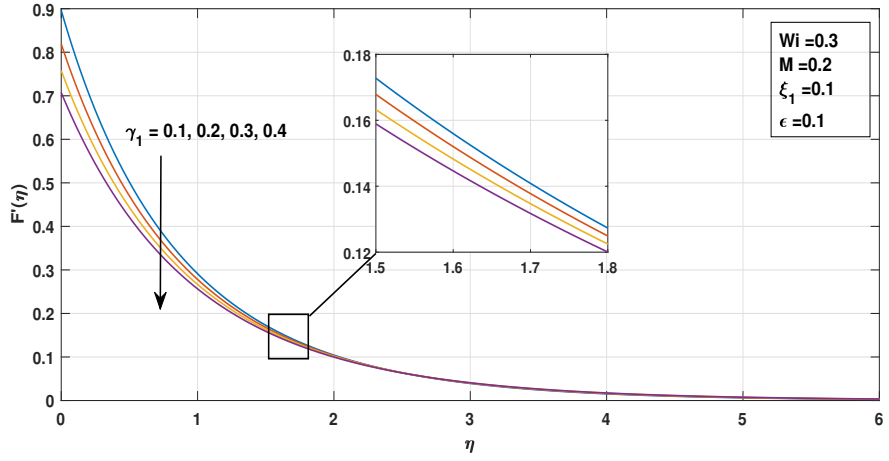

FIGURE 3.4: Effect of γ_1 on velocity profile $F'(\eta)$

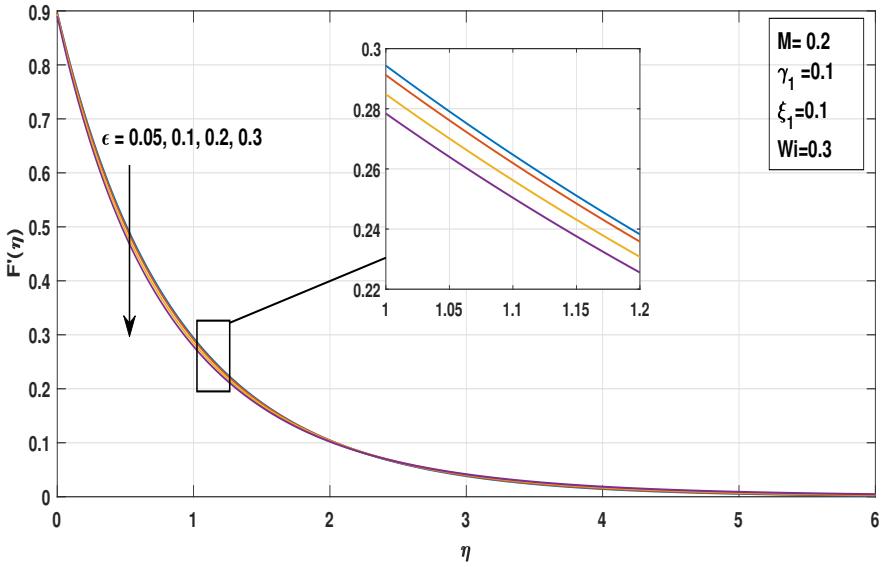

FIGURE 3.5: Effect of ϵ on velocity profile $F'(\eta)$

A view of Figure **??** clearly shows that by growing the Williamson parameter Wi, the velocity $F'(\eta)$ of the fluid drops. This happens because the Williamson parameter has direct relation with relaxation time(the time after being deformed, the fluid particles take to return to equilibrium). As a result, a stronger resistance reduces the flow of the fluid, so the velocity decreases, thats why the velocity profile drops as the Williamson parameter Wi grows. Figure 3.4 is sketched to check the result of the slip parameter on the velocity profile. The velocity decreases upon an increase in the slip parameter γ_1. This happens because a higher slip parameter reduces the ability to drag the fluid. As a result, less momentum is transferred into the fluid which decreases the velocity profile Figure 3.5 highlights the relationship between unsteady parameter ϵ and the fluid velocity. As a result, indicate a significant decline in the fluid velocity occurs as the unsteady parameter increases. The elastic nature of Williamson fluid, responds slowly to sudden changes, leading to a decline in the velocity profile.

3.5.3 Temperature Profile

In this section, the influence of different physical parameters on the $\theta(\eta)$, is examined. In Figures 3.6 and 3.7, we study the impact of the M and Eckert number Ec

on the temperature profile. Temperature profile augments when the M increases. When the magnetic field is applied, it generates a resistive force designated as the Lorentz force. The Lorentz force directly resists the fluid motion, allowing greater heat retention within the boundary layer, resulting in a higher temperature. Similarly, we observe that an increase in the Ec leads to a higher fluid temperature. The high Eckert number enhances the conversion of the fluid kinetic energy into the thermal energy. As a result of this phenomenon, heat is generated within the fluid, causing its temperature to increase.

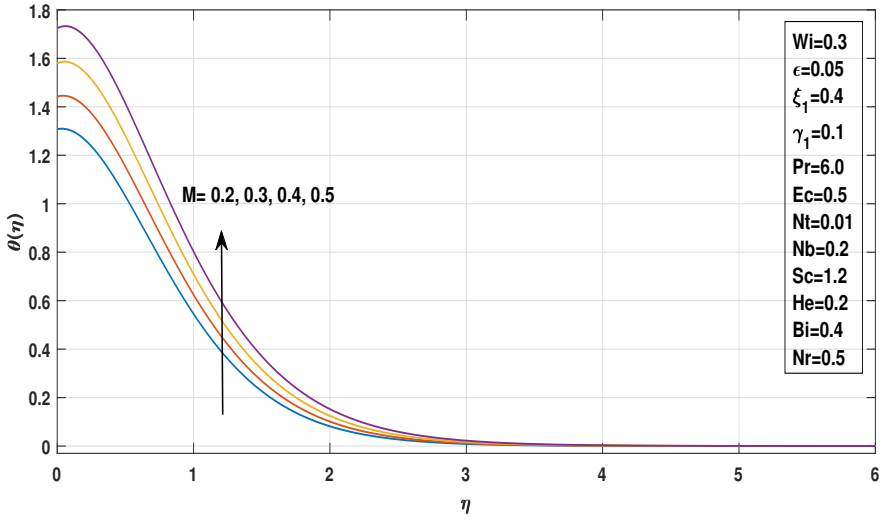

FIGURE 3.6: Outcome of M on temperature profile $\theta(\eta)$

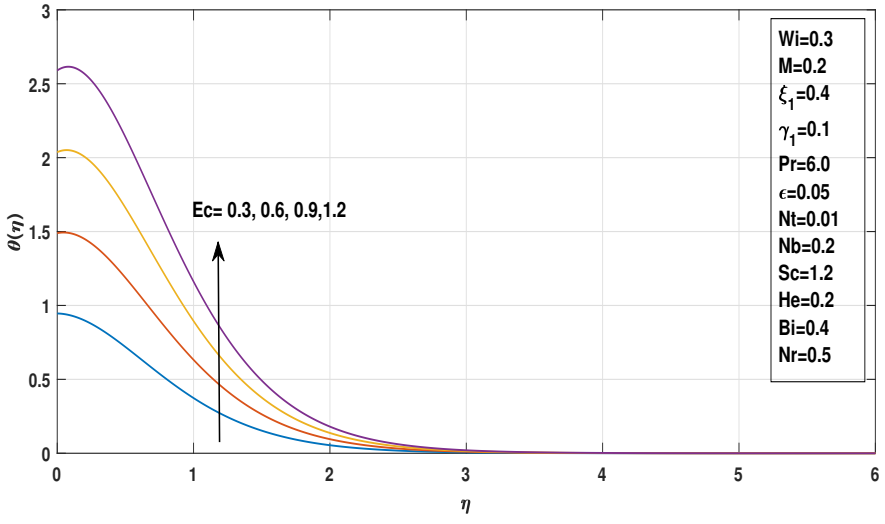

FIGURE 3.7: Impact of Ec on temperature profile $\theta(\eta)$

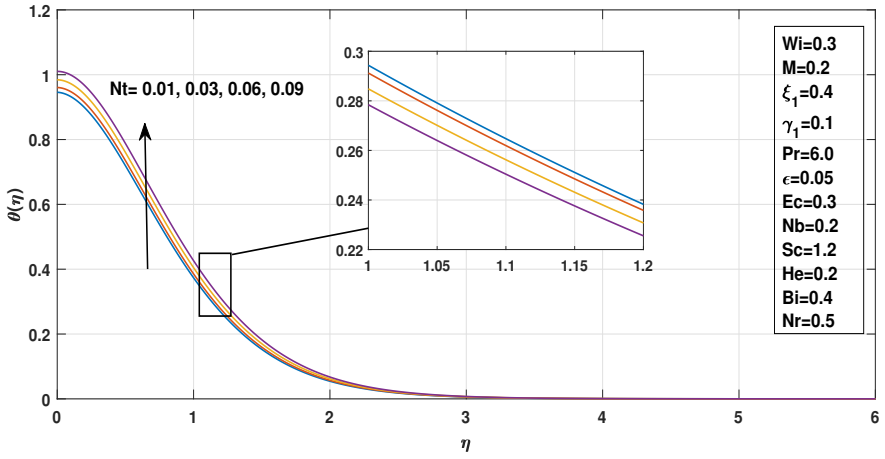

FIGURE 3.8: Effect of Nt on temperature profile $\theta(\eta)$

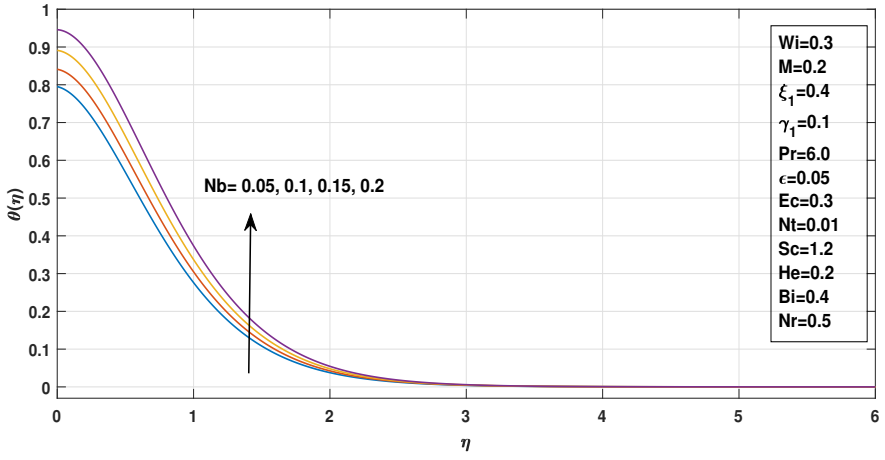

FIGURE 3.9: Effect of Nb on temperature profile $\theta(\eta)$

The influence of the Nt and Nb on the temperature distribution has been notices through Figure 3.8 and 3.9. An increase in values of Nt and Nb directly increases the fluid temperature distribution. When thermophoresis parameter increases, it enhances the migration of the nanoparticles from a hotter region toward a cooler one due to a temperature gradient. Similarly, the Brownian motion parameter (Nb) represents the random collision of nanoparticles in the fluid molecules. As Nb increases, nanoparticles transfer more thermal energy within the fluid. As a result of this dual mechanism, the fluid temperature rises, leading to an increase in the thickness of the thermal boundary layer.

Figure 3.10 explores the relationship between the radiation parameter (Nr) and

the temperature distribution. An increase in the radiation parameter (Nr) enhances the amount of heat transported by radiation into fluid from the stretching sheet. As a result, the fluid absorbs more thermal energy, which increases its the temperature profile and thermal boundary layer becomes thicker.

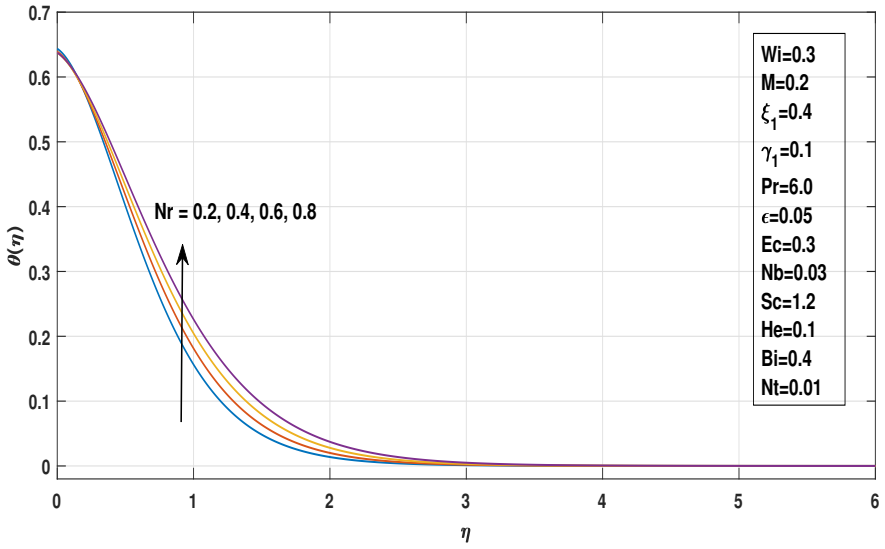

FIGURE 3.10: Effect of Nr on temperature profile $\theta(\eta)$

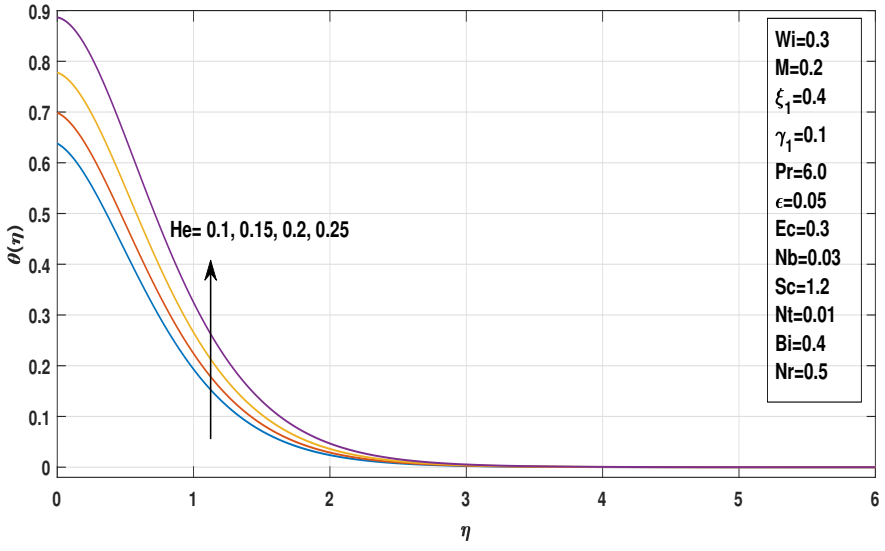

FIGURE 3.11: Effect of He on temperature profile $\theta(\eta)$

In Figure 3.11 we noticed that increasing the heat generation parameter (He) lead to a higher fluid temperature. More heat is produced inside the fluid when He increases, as a result enhancing its thermal energy. Consequently, the temperature

profile rises and the thermal boundary layer becomes thicker by increasing the heat generation parameter He. Moving forward , Figure 3.12 depicts the impact of the Biot number Bi on the temperature distribution. A the value of Biot number increases, the temperature distribution is enhanced. Due to an increase in the Biot number, the fluid gains more heat from the surface. This leads to an increase in the thermal energy leading to a higher temperature profile and a thicker thermal boundary layer of the Williamson nanofluid.

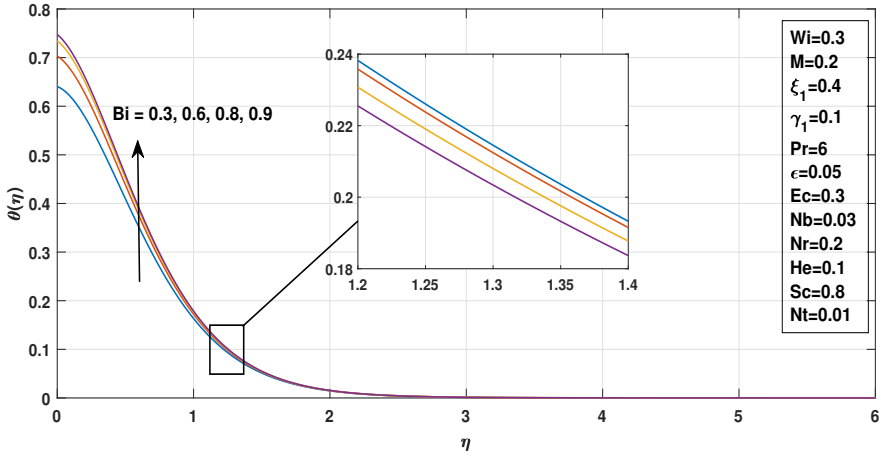

FIGURE 3.12: Effect of Bi on temperature profile $\theta(\eta)$

3.5.4 Concentration Profile

The concentration profile within a fluid plays a significant role in its transport behavior. The thermal conductivity of a fluid is related to the concentration located in it. In this regard, Figures 3.13, 3.14 and 3.15 demonstrate the influence of M, Ec and Bi on the concentration profile. As the M increases, the concentration distribution rises due to generating a Lorentz force that resists its motion. The (Ec) Eckert number measures the ratio of the thermal energy to the kinetic energy and reflects viscous dissipation, which enhances nanoparticle transport and raises the concentration profile. In Figure 3.15 illustrates the role of the thermophoresis parameter Nt on the concentration profile. When parameter Nt increases, there is a subsequent increase in the concentration profile.Mechanically, thermophoresis describes the motion of nanoparticles migrate more strongly from hot to cold area

due to temperature gradient in the fluid, leading to a higher concentration profile near the stretching sheet. Conversely, in figures 3.16 and 3.17 demonstrate the effect of the Nb and Nr on concentration distribution. Increasing both of the parameter leads to a reduction in the concentration. Physically, Nb enhances the random motion of the fluid. When Nb increases, the movement of nanoparticles spread more uniformly into the fluid in all directions. Therefore, the concentration profile decreases as Nb increase. Similarly, a higher (Nr) radiation parameter increases the fluid temperature, which enhances nanoparticles diffusion through thermophoresis and Brownian motion. Consequently, nanoparticles accumulate less near the stretching sheet. Therefore, the concentration profile decreases with increasing Nr.

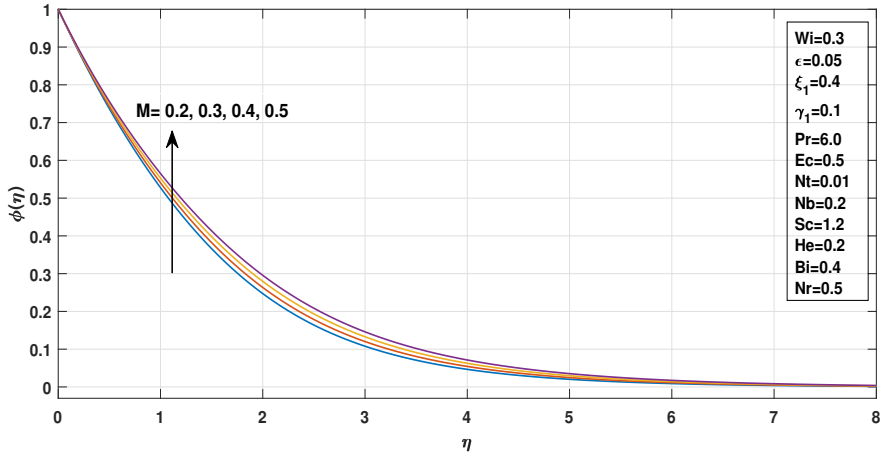

FIGURE 3.13: Effect of M on concentration profile $\phi(\eta)$

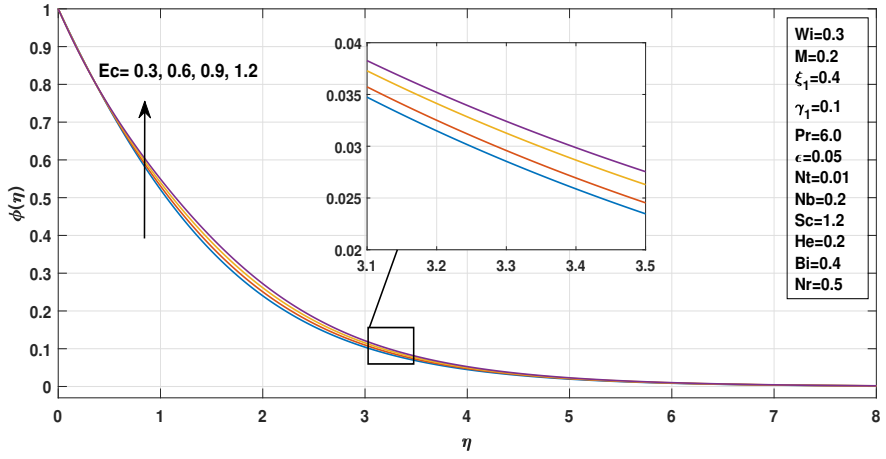

FIGURE 3.14: Effect of Ec on concentration profile $\phi(\eta)$

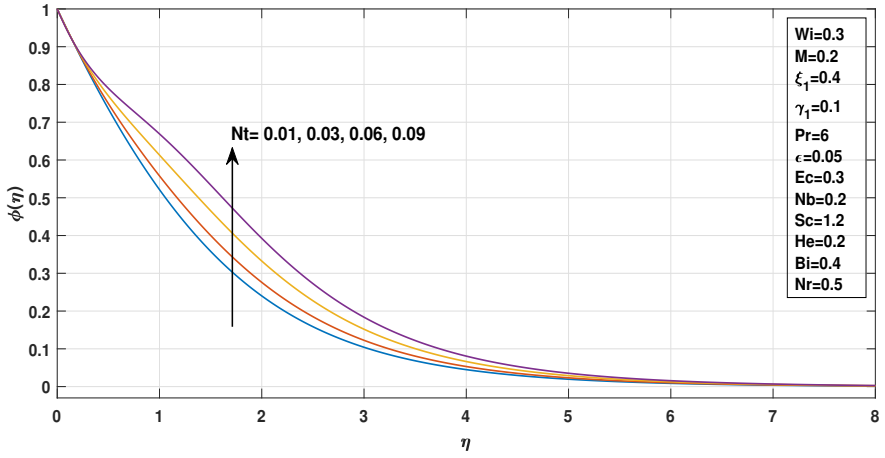

FIGURE 3.15: Effect of Nt on concentration profile $\phi(\eta)$

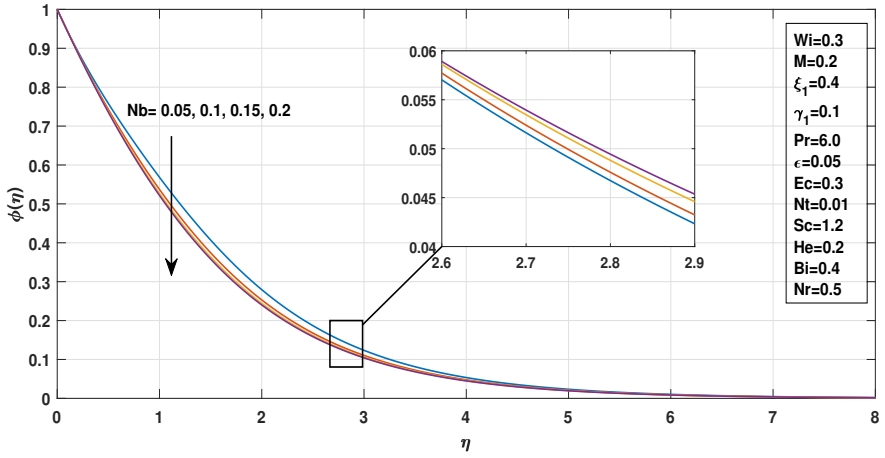

FIGURE 3.16: Effect of Nb on concentration profile $\phi(\eta)$

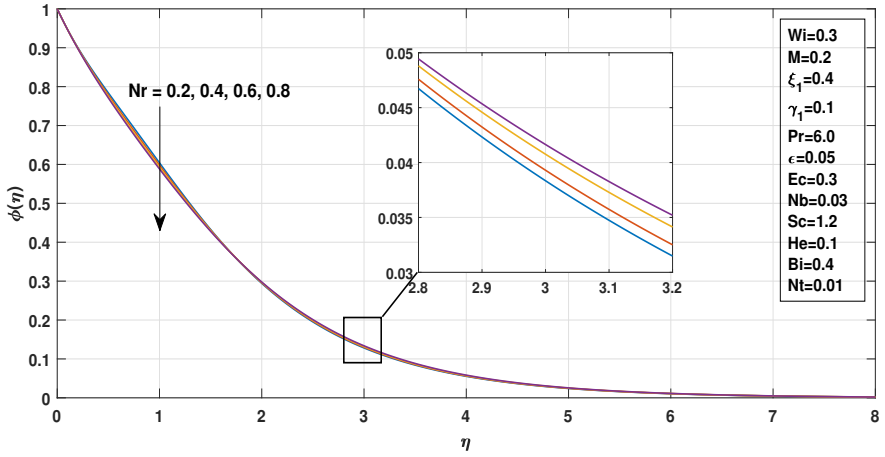

FIGURE 3.17: Impact of Nr on concentration profile $\phi(\eta)$

Figure 3.18 illustrates the influence of heat generation (He) on $\phi(\eta)$. As the value of He increases, an increases in the concentration $\phi(\eta)$ is observed. Physically, the heat generation parameter (He) refers to the internal heat being added into the fluid. When heat generation parameter (He) increases the fluid temperature throughout the boundary layer is increased. This leads to an increases in the concentration profile.

Figure 3.19 illustrates the impact of (Sc) Schmidt number on the concentration profile $\phi(\eta)$. As the parameter Sc increases, there is inverse relationship resulting is a subsequent decrease in the concentration profile. Physically, the Schmidt Number(Sb) refers the ratio of momentum diffusivity to mass diffusivity in the fluid. Higher Sc reduces the ability of the nanoparticles to diffuse near the stretching sheet. As a result, more particles are carried along the flow, lowering the concentration near the surface. Therefore, the concentration decreases with increasing Sc in the Williamson nanofluid.

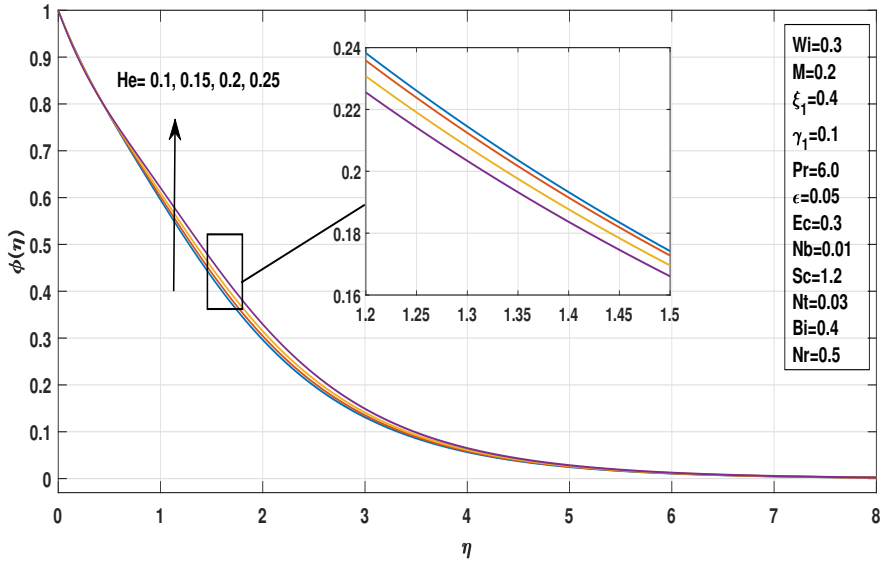

FIGURE 3.18: Impact of He on concentration profile $\phi(\eta)$

3.5.5 Motile Density Profile

Figure 3.20 an increase in the bioconvection Schmidt number Sb leads to a noticeable decrease in the motile microorganism density profile. Physically, a higher Sb

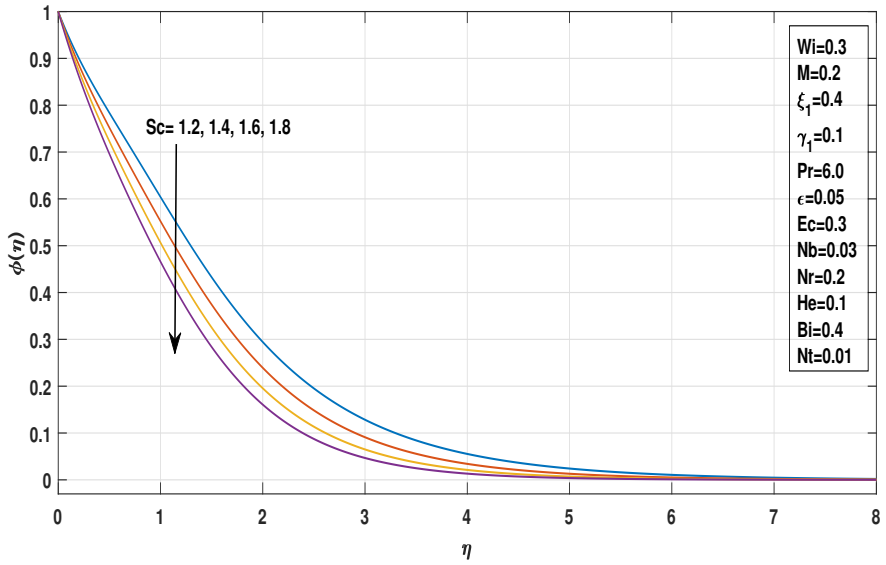

FIGURE 3.19: Outcome of Sc on concentration profile $\phi(\eta)$

represents lower microorganism diffusivity relative to viscous effects. This reduction in diffusivity weakens the ability of motile microorganisms to spread within the boundary layer. Consequently, bio convective transport is suppressed, resulting in a thinner motile microorganism distribution within the flow region.

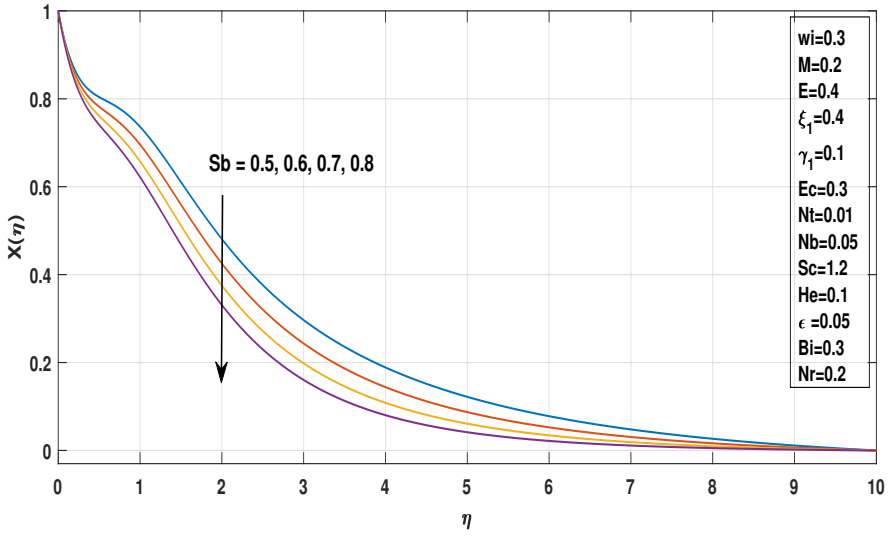

FIGURE 3.20: Result of Sb on motile density profile $\phi(\eta)$

Figure 3.21 demonstrates the influence of Peclet number (Pe) on the motile microorganisms. Higher values of this parameter decrease the motile microorganism

$X(\eta)$. Increasing the Peclet number (Pe) enhances advective transport, causing motile microorganisms to move away from the stretching sheet and reducing their density.

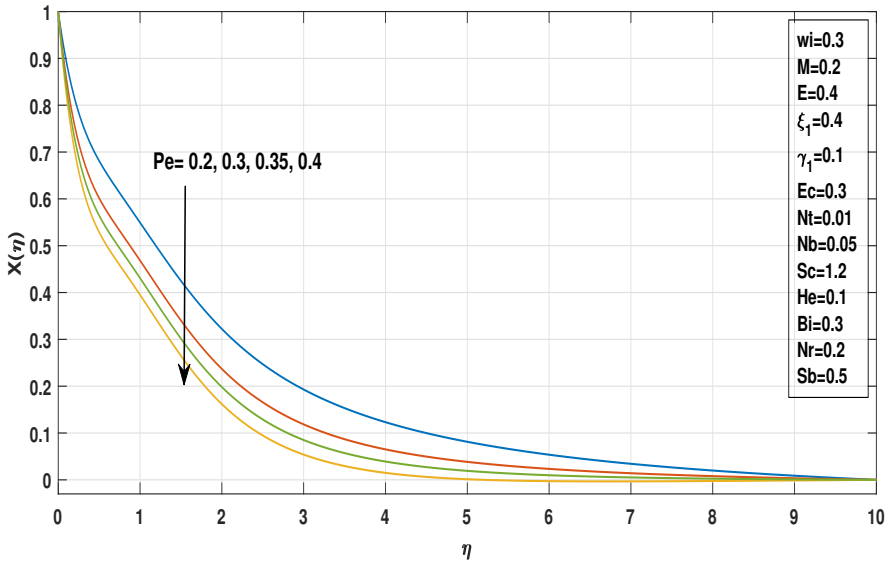

FIGURE 3.21: Outcome of Pe on motile density profile $\phi(\eta)$

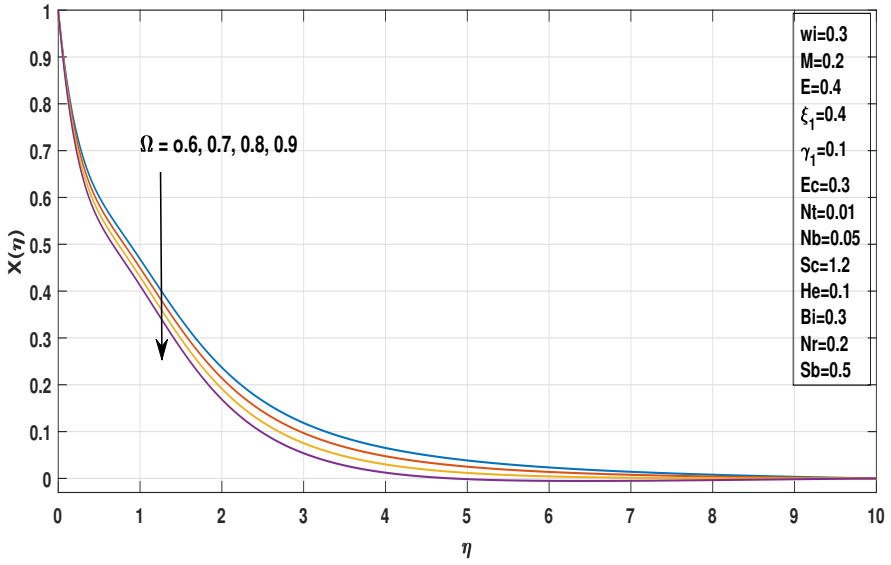

FIGURE 3.22: Impact of Ω on motile density profile $\phi(\eta)$

Figure 3.22 show that increasing the motile density parameter (Ω) reduces the motile microorganism density $X(\eta)$, because a smaller wall to ambient concentration difference weakens the microorganism accumulation near the surface. This

leads to a thinner motile density layer across the boundary layer. Consequently, the overall motile number decreases, indicating a reduced bioconvection effect in the system.

Chapter 4

Numerical Analysis of Time-Dependent Casson Fluid Bio Convection in a Porous Medium with Thompson–Troian Slip

4.1 Introduction

In the previous chapter, the unsteady Williamson nanofluid flow over a stretching sheet was investigated numerically. In this chapter, the analysis is extended to examine the unsteady flow of a Casson fluid over a stretching sheet in the existence of a porous medium. The porous medium effect is incorporated into the momentum equation through an appropriate resistance term, accounting for the influence of permeability on the flow characteristics. By employing suitable similarity transformations, the governing nonlinear partial differential equations are reduced to a system of dimensionless ordinary differential equations. The resulting

system is solved numerically using the shooting method to analyze the effects of various physical parameters on the flow behavior.

4.2 Mathematical Modeling

This chapter investigates the unsteady flow of a Casson fluid on a stretching sheet embedded in a porous medium, under two-dimensional boundary layer assumptions. The coordinate system is defined such that the x-axis is oriented across the stretching sheet, representing the flow direction, while the y-axis is perpendicular to the sheet, representing the distance from the surface, as shown in Figure 4.1. The sheet stretches with a velocity $U_w = \frac{ax}{(1-ct)}$. At the sheet surface, the fluid velocity matches the stretching velocity, while the temperature, nanoparticle concentration, and microorganism density are prescribed at their wall values. Far from the sheet where $y \longrightarrow \infty$, the velocity approaches zero, and the temperature, concentration, and microorganism density attain ambient fluid values. The porous medium impact is included through a Darcy resistance term in the momentum equation, and the magnetic field impact is incorporated in the momentum equation as well. The unsteady flow of the Casson fluid is governed by the following equations (4.1)–(4.5), alongside the boundary conditions (4.6).

$$\frac{\partial u}{\partial x} + \frac{\partial v}{\partial y} = 0, \tag{4.1}$$

$$v\frac{\partial u}{\partial y} + u\frac{\partial u}{\partial x} + \frac{\partial u}{\partial t} + \frac{\sigma B_o^2}{\rho(1-ct)}u = \nu\left[1+\frac{1}{\beta}\right]\frac{\partial^2 u}{\partial y^2} - \frac{\mu}{\rho K_p}u, \tag{4.2}$$

$$\begin{aligned} v\frac{\partial T}{\partial y} + u\frac{\partial T}{\partial x} + \frac{\partial T}{\partial t} &= \frac{\sigma B_o^2}{(\rho C_p)_f}\frac{u^2}{(1-ct)} + \frac{\nu}{(C_p)_f}\left[1+\frac{1}{\beta}\right]\left(\frac{\partial u}{\partial y}\right)^2 + \alpha\frac{\partial^2 T}{\partial y^2} \\ &+ \frac{\mu}{\rho K_p C_p}u^2 + \tau\left[\frac{D_T}{T_\infty}\left(\frac{\partial T}{\partial y}\right)^2 + \frac{\partial T}{\partial y}\frac{\partial C}{\partial y}D_B\right] - \frac{\partial q_r}{\partial y}\frac{1}{\rho C_p} + (T-T_\infty)\frac{Q_0}{\rho C_p}, \end{aligned} \tag{4.3}$$

$$v\frac{\partial C}{\partial y} + u\frac{\partial C}{\partial x} + \frac{\partial C}{\partial t} - \frac{D_T}{T_\infty}\frac{\partial^2 T}{\partial y^2} = \frac{\partial^2 C}{\partial y^2}D_B, \tag{4.4}$$

$$v\frac{\partial N}{\partial y} + u\frac{\partial N}{\partial x} + \frac{\partial}{\partial y}\left[N\frac{\partial C}{\partial y}\right]\frac{b_c W_c}{(C_w - C_\infty)} + \frac{\partial N}{\partial t} = \frac{\partial^2 N}{\partial y^2}D_N. \tag{4.5}$$

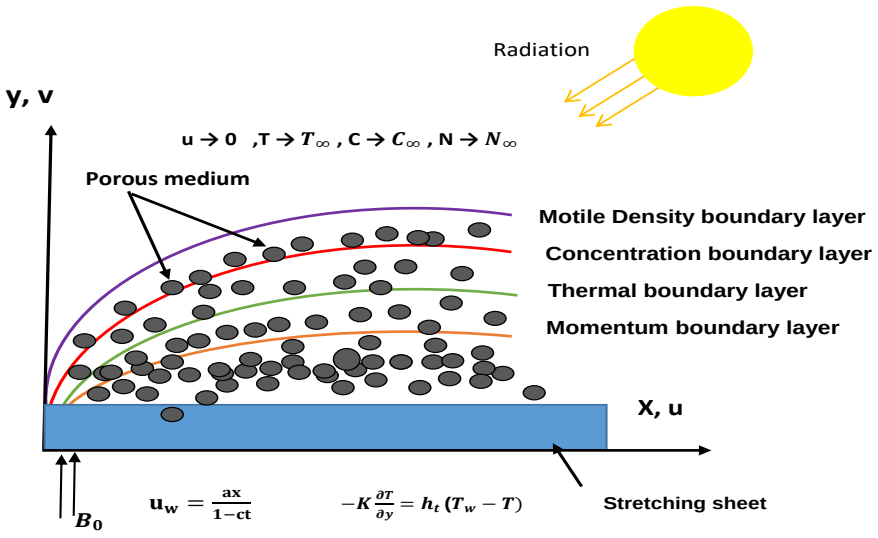

FIGURE 4.1: Flowchart

4.2.1 Boundary Conditions

The boundary conditions applied here are identical to those presented in Chapter 3, as given in Eq. (3.6).

4.3 Similarity Transformation and Non-dimensionalization of Mathematical Model

This section presents the non-dimensionalization of the governing equations for the Casson fluid model. The relevant dimensionless variables and parameters are introduced to simplify the mathematical formulation of the problem.

By employing the similarity transformations defined in Chapter 3(see Eqs. (3.9)), the governing PDEs are transformed into a system of ODEs for numerical computation.

4.3.1 Non-dimensionalization of Momentum Equation

In this subsection, the governing momentum equation (4.2) is non-dimensionalized using the partial derivatives defined in Eqs (3.10)–(3.13). Substituting these derivatives together with the velocity component given in (3.9), we obtain the following equation.

$$\frac{axc}{(1-ct)^2}F' + \frac{axc\eta}{2(1-ct)^2}F'' + \frac{a^2x}{(1-ct)^2}F'^2 - \frac{a^2x}{(1-ct)^2}FF'' = \nu\left[1+\frac{1}{\beta}\right]\left(\frac{a^2x}{\nu(1-ct)^2}F'''\right) - \left(\frac{\sigma B_o}{\rho(1-ct)}\right)\left(\frac{ax}{(1-ct)}F'\right) - \frac{\mu ax}{\rho K_p(1-ct)}F'.$$

$$\Rightarrow \quad \left(F'\right)^2 - F''F + \frac{c}{a}F' + \frac{\eta c}{2a}F'' = F'''\left[1+\frac{1}{\beta}\right] - \frac{\sigma B_o^2}{a\rho}F' - \frac{\mu(1-ct)}{\rho K_p a}F'.$$

$$\Rightarrow \quad -F''F + \epsilon F' + \frac{\eta}{2}\epsilon F'' + \left(F'\right)^2 = F'''\left[1+\frac{1}{\beta}\right] - MF' - SF'.$$

$$\Rightarrow \quad \left[1+\frac{1}{\beta}\right]F''' + F''F - (M+\epsilon+S)F' - \frac{\eta}{2}\epsilon F'' - F'^2 = 0. \tag{4.6}$$

4.3.2 Non-dimensionalization of Energy Equation

For the Casson fluid model, the energy equation (4.3) is converted into its non-dimensional form. Upon substituting the derivatives given in Eqs (3.15)–(3.22) and the velocity component defined in (3.9), the following expression is obtained:

$$\begin{aligned}
&\theta'(T_w - T_\infty)\frac{\eta c}{2(1-ct)} - \frac{a}{(1-ct)}\left(T_w - T_\infty\right)F\theta' \\
&= \theta''\frac{a\alpha}{\nu(1-ct)}\left(T_w - T_\infty\right) + \frac{\sigma B_o^2 a^2 x^2}{(\rho C_p)_f(1-ct)^3}F'^2 + \frac{a^3x^2}{(C_p)_f(1-ct)^3}\left(1+\frac{1}{\beta}\right)F''^2 \\
&+ \tau\left[D_B\left(T_w - T_\infty\right)\theta'\phi'\left(C_w - C_\infty\right)\frac{a}{\nu(1-ct)} + \theta'^2\frac{aD_T}{\nu T_\infty(1-ct)}\left(T_w - T_\infty\right)^2\right] \\
&+ \frac{16\sigma T_\infty^3}{3\rho C_p K^*}(T_w - T_\infty)\frac{a}{\nu(1-ct)}\theta'' + \frac{Q_0}{\rho C_p}(T_w - T_\infty)\theta.
\end{aligned}$$

$$
\begin{aligned}
&\Rightarrow \frac{\eta c}{2a}\theta' - F\theta' = \frac{\alpha}{\nu}\theta'' + \frac{ax^2\sigma B_o^2}{\big(T_w - T_\infty\big)(\rho C_p)_f(1-ct)^2}F'^2 + \frac{Q_0(1-ct)}{a\rho C_p}\theta \\
&\quad + \frac{a^2x^2}{\big(T_w - T_\infty\big)(C_p)_f(1-ct)^2}\big(1+\frac{1}{\beta}\big)F''^2 + \tau\Bigg[\frac{D_B}{\nu}\big(C_w - C_\infty\big)\theta'\phi' \\
&\quad + \frac{D_T}{\nu T_\infty}\big(T_w - T_\infty\big)\theta'^2\Bigg] + \frac{16\sigma T_\infty^3}{3\rho c_p K^*}\theta'' + \frac{\mu a x^2}{\rho C_p K_p(1-ct)(T_w - T_\infty)}. \\
\Rightarrow\ &\frac{\eta}{2}\epsilon\theta' - F\theta' = \frac{1}{Pr}\theta'' + MEcF'^2 + Ec\big(1+\frac{1}{\beta}\big)F''^2 + Nb\theta'\phi' + Nt\theta'^2 \\
&\quad + \frac{N_r}{P_r}\theta'' + H_e\theta + EcSF'^2. \\
\Rightarrow\ &\theta'' + N_R\theta'' + Pr\Bigg[MEcF'^2 + Ec(1+\frac{1}{\beta})F''^2 + EcSF'^2 + Nb\theta'\phi' + Nt\theta'^2 \\
&\quad + F\theta' + H_e\theta - \frac{\eta}{2}\epsilon\theta'\Bigg] = 0.
\end{aligned}
\tag{4.7}
$$

The non-dimensional forms of the concentration and motile microorganism equations have already been derived in Chapter 3 (see Eqs. (3.27) and (3.33)). In the present chapter, these dimensionless equations are directly employed for the analysis. Moreover, the corresponding non-dimensional boundary conditions derived in Chapter 3 are used here without modification. The dimensionless parameters incorporated in the equations are introduced in Chapter 3, and the remaining one is presented below:

$$S = \frac{\nu(1-ct)}{aK}.$$

4.3.3 Non-dimensionalization of Physical Quantities

The dimensionless physical quantities relevant to the present study are presented below. The skin friction coefficient is derived here, whereas the other parameters are taken from Chapter 3 (Eqs. (3.35)–(3.37)). Their definitions and mathematical expressions are provided for clarity.

Skin friction:

$$C_f = \frac{\mu\Big(1+\frac{1}{\beta}\Big)\Big[\Big(\frac{\partial u}{\partial y}\Big)_{y=0}\Big]}{\rho U_w^2}$$

$$= \frac{\mu\left(1+\frac{1}{\beta}\right)\sqrt{\frac{a}{\nu(1-ct)}}U_w F''(0)}{\rho U_w^2}$$

$$= \left(1+\frac{1}{\beta}\right)\sqrt{\frac{a}{\nu(1-ct)}}\frac{\mu}{\rho U_w}F''(0)$$

$$C_f\sqrt{Re_x} = \big(1+\frac{1}{\beta}\big)F''(0). \tag{4.8}$$

where the Re_x is defined as $\big(Re_x\big)^{\frac{1}{2}} = x\sqrt{\frac{a}{\nu(1-ct)}}$.

4.4 Solution Framework

The numerical solutions are obtained via the shooting method based on the RK4 method. As the first step in solving the ODE for the momentum equation (4.6), the following notations are defined:

$$F = \widetilde{K}_1, \qquad F' = \widetilde{K}_1' = \widetilde{K}_2, \qquad F'' = \widetilde{K}_2' = \widetilde{K}_3.$$

The momentum equation is formulated in the following form as a system of first-order ODEs:

$$\widetilde{K}_1 = \widetilde{K}_2, \qquad \widetilde{K}_1(0) = 0,$$

$$\widetilde{K}_2 = \widetilde{K}_3, \qquad \widetilde{K}_2(0) = 1+\gamma_1\left[\frac{\widetilde{K}_3(0)}{\sqrt{1-\zeta_1\widetilde{K}_3(0)}}\right],$$

$$\widetilde{K}_3 = \big(\widetilde{K}_2^2-\widetilde{K}_1\widetilde{K}_3+\big(M+\epsilon+S\big)\widetilde{K}_2+\frac{\eta}{2}\epsilon\widetilde{K}_3\big)\frac{1}{\big(1+\frac{1}{\beta}\big)}, \qquad \widetilde{K}_3(0) = \widetilde{b}.$$

To numerically solve the above IVP, the 4th order Runge-Kutta method is applied. The unknown initial condition $\widetilde{b}$ is determined by ensuring that:

$$\widetilde{K}_2\big(\eta_\infty, \widetilde{b}\big) = 0.$$

The value of b is computed using Newton's method, following the iterative scheme outlined below:

$$\widetilde{b}^{(n+1)} = \widetilde{b}^{(n)} - \frac{\widetilde{K}_2\big(\eta_\infty \widetilde{b}^{(n)}\big)}{\left(\frac{\partial}{\partial \widetilde{b}}\widetilde{K}_2\big(\eta_\infty, \widetilde{b}\big)\right)^{(n)}}.$$

The following derivatives are required to implement the iterative scheme described above:

$$\frac{\partial \widetilde{K}_1}{\partial \widetilde{b}} = \widetilde{K}_4; \qquad \frac{\partial \widetilde{K}_2}{\partial \widetilde{b}} = \widetilde{K}_5; \qquad \frac{\partial \widetilde{K}_3}{\partial \widetilde{b}} = \widetilde{K}_6.$$

Thus, with these new notations, the Newton's iterative scheme can be represented as:

$$\widetilde{b}^{(n+1)} = \widetilde{b}^{(n)} - \frac{\widetilde{K}_2\big(\eta_\infty, \widetilde{b}^{(n)}\big)}{\widetilde{K}_5\big(\eta_\infty, \widetilde{b}^{(n)}\big)}.$$

Next, the system of first-order ODEs is differentiated with respect to $\widetilde{b}$, resulting in a new system of ODEs, as shown below:

$$\widetilde{K}_4 = \widetilde{K}_5, \qquad \widetilde{K}_4(0) = 0,$$

$$\widetilde{K}_5 = \widetilde{K}_6, \qquad \widetilde{K}_5(0) = \frac{\gamma_1}{\sqrt{1-\zeta_1\widetilde{b}}} + \frac{\gamma_1 \widetilde{b}\zeta_1}{2\big(1-\zeta_1\widetilde{b}\big)^{\frac{3}{2}}},$$

$$\widetilde{K}_6 = 2\widetilde{K}_2\widetilde{K}_5 - \widetilde{K}_1\widetilde{K}_6 - \widetilde{K}_3\widetilde{K}_4 + \big(M+\epsilon+S\big)\widetilde{K}_5 + \frac{\eta}{2}\epsilon\widetilde{K}_6\left(\frac{1}{1+\frac{1}{\beta}}\right), \qquad \widetilde{K}_6(0) = 1.$$

Newton's iterative scheme terminates when the following condition is met:

$$\left|\widetilde{K}_2\big(\eta_\infty, \widetilde{b}^n\big)\right| < \epsilon_1,$$

Equations (4.3) and (4.4) are solved numerically via the shooting method, with F, F', and F'' assumed known. The following notations are adopted for the implementation:

$$\theta = \widetilde{L}_1, \qquad \theta' = \widetilde{L}_1' = \widetilde{L}_2, \qquad \phi = \widetilde{L}_3, \qquad \phi' = \widetilde{L}_3' = \widetilde{L}_4.$$

The equations (4.3) and (4.4) are transformed into the following first order coupled ODEs:

$$\widetilde{L}_1' = \widetilde{L}_2, \qquad \widetilde{L}_1(0) = \widetilde{V},$$

$$\widetilde{L}_2' = -Pr\Big[EcSF''^2 + F\widetilde{L}_2 + Ec\big(1+\frac{1}{\beta}\big)F''^2 + MEcF'^2 + Nb\widetilde{L}_2\widetilde{L}_4 + Nt\widetilde{L}_2^2 + He\widetilde{L}_1 - \frac{\eta}{2}\epsilon\widetilde{L}_2\Big]\frac{1}{1+N_R}, \qquad \widetilde{L}_2(0) = -Bi(1-\widetilde{L}_1),$$

$$\widetilde{L}_3' = \widetilde{L}_4, \qquad \widetilde{L}_3(0) = 1,$$

$$\widetilde{L}_4' = -(F-\frac{\eta}{2})Sc\widetilde{L}_4 + Pr\frac{Nt}{Nb}\Big[EcSF''^2 + F\widetilde{L}_2 + Ec\big(1+\frac{1}{\beta}\big)F''^2 + MEcF'^2 + Nb\widetilde{L}_2\widetilde{L}_4 + Nt\widetilde{L}_2^2 + He\widetilde{L}_1 - \frac{\eta}{2}\epsilon\widetilde{L}_2\Big]\frac{1}{1+N_R}, \qquad \widetilde{L}_4(0) = \widetilde{W}.$$

The RK-4 method has been applied to solve the above IVP. The missing conditions $\widetilde{V}$ and $\widetilde{W}$ should be chosen such that:

$$\widetilde{L}_1\big(\eta_\infty, \widetilde{V}, \widetilde{W}\big) = 0, \qquad \widetilde{L}_3\big(\eta_\infty, \widetilde{V}, \widetilde{W}\big) = 0.$$

Newton's method is employed to solve for $\widetilde{V}$ and $\widetilde{W}$, via the following iterative procedure:

$$\begin{bmatrix}\widetilde{V}\\ \widetilde{W}\end{bmatrix}^{(n+1)} = \begin{bmatrix}\widetilde{V}\\ \widetilde{W}\end{bmatrix}^{(n)} - \left(\begin{bmatrix}\frac{\partial\widetilde{L}_1}{\partial\widetilde{V}} & \frac{\partial\widetilde{L}_1}{\partial\widetilde{W}}\\ \frac{\partial\widetilde{L}_3}{\partial\widetilde{V}} & \frac{\partial\widetilde{L}_3}{\partial\widetilde{W}}\end{bmatrix}^{-1}\right)^{(n)} \begin{bmatrix}\widetilde{L}_1\\ \widetilde{L}_3\end{bmatrix}^{(n)}$$

Let us introduce the following notation:

$$\frac{\partial\widetilde{L}_1}{\partial\widetilde{V}} = \widetilde{L}_5, \quad \frac{\partial\widetilde{L}_2}{\partial\widetilde{V}} = \widetilde{L}_6, \quad \frac{\partial\widetilde{L}_3}{\partial\widetilde{V}} = \widetilde{L}_7, \quad \frac{\partial\widetilde{L}_4}{\partial\widetilde{V}} = \widetilde{L}_8,$$
$$\frac{\partial\widetilde{L}_1}{\partial\widetilde{W}} = \widetilde{L}_9, \quad \frac{\partial\widetilde{L}_2}{\partial\widetilde{W}} = \widetilde{L}_{10}, \quad \frac{\partial\widetilde{L}_3}{\partial\widetilde{W}} = \widetilde{L}_{11}, \quad \frac{\partial\widetilde{L}_4}{\partial\widetilde{W}} = \widetilde{L}_{12}.$$

Rewriting the Newton's iterative scheme with the new notation gives:

$$\begin{bmatrix}\widetilde{V}\\ \widetilde{W}\end{bmatrix}^{(n+1)} = \begin{bmatrix}\widetilde{V}\\ \widetilde{W}\end{bmatrix}^{(n)} - \left(\begin{bmatrix}\widetilde{L}_5 & \widetilde{L}_9\\ \widetilde{L}_7 & \widetilde{L}_{11}\end{bmatrix}^{-1}\right)^{(n)} \begin{bmatrix}\widetilde{L}_1\\ \widetilde{L}_3\end{bmatrix}^{(n)}$$

By differentiating the last system of four first-order ODEs with respect to $\widetilde{V}$ and $\widetilde{W}$, we obtain another system of ODEs, as shown below:

$$\widetilde{L}_5' = \widetilde{L}_6, \qquad \widetilde{L}_5(0) = 1,$$

$$\widetilde{L}_6' = -Pr\left[F\widetilde{L}_6 + Nb\big(\widetilde{L}_6\widetilde{L}_4 + \widetilde{L}_2\widetilde{L}_8\big) + 2Nt\widetilde{L}_2\widetilde{L}_6 + He\widetilde{L}_5 - \frac{\eta}{2}\epsilon\widetilde{L}_6\right]\frac{1}{1+N_R}, \quad \widetilde{L}_6(0) = -Bi\widetilde{L}_5,$$

$$\widetilde{L}_7' = \widetilde{L}_8, \qquad \widetilde{L}_7(0) = 0,$$

$$\widetilde{L}_8' = -(F - \frac{\eta}{2})Sc\widetilde{L}_8 - \frac{Nt}{Nb}\widetilde{L}_6', \qquad \widetilde{L}_8(0) = 0,$$

$$\widetilde{L}_9' = \widetilde{L}_{10}, \qquad \widetilde{L}_9(0) = 0,$$

$$\widetilde{L}_{10}' = -Pr\left[F\widetilde{L}_{10} + Nb\big(\widetilde{L}_{10}\widetilde{L}_4 + \widetilde{L}_2\widetilde{L}_{12}\big) + 2Nt\widetilde{L}_2\widetilde{L}_{10} + He\widetilde{L}_9 - \frac{\eta}{2}\epsilon\widetilde{L}_{10}\right]\frac{1}{1+N_R}, \qquad \widetilde{L}_{10}(0) = -Bi\widetilde{L}_9,$$

$$\widetilde{L}_{11}' = \widetilde{L}_{12}, \qquad \widetilde{L}_{11}(0) = 0,$$

$$\widetilde{L}_{12}' = -(F - \frac{\eta}{2}\epsilon)Sc\widetilde{L}_{12} - \frac{Nt}{Nb}\widetilde{L}_{10}', \qquad \widetilde{L}_{12}(0) = 1.$$

The stopping criterion for Newton's method is set as:

$$max\left\{\left|\widetilde{L}_1\big(\eta_\infty, \widetilde{V^n}, \widetilde{W^n}\big)\right|, \left|\widetilde{L}_3\big(\eta_\infty, \widetilde{V^n}, \widetilde{W^n}\big)\right|\right\} < \epsilon_1,$$

The numerical computation of the motile microorganism equation (4.5) was performed using the shooting method in Chapter 3, and the same approach is adopted here.

4.5 Results Interpretation

After converting the partial differential equations into a system of ordinary differential equations, the effects of various physical parameters become more apparent.

This section presents a detailed discussion of the effect of key dimensionless parameters on $C_f\sqrt{Re_x}$, $\frac{Nu_x}{\sqrt{Re_x}}$, $\frac{Sh_x}{\sqrt{Re_x}}$ and $\frac{Nn_x}{\sqrt{Re_x}}$. The numerical results are reported using suitable graphical representations and tabulated data.

4.5.1 Analysis of Computational Results

Table 4.1 illustrates the effect of β, M, and S on $C_f\sqrt{Re_x}$. Increasing β from 0.3 to 0.9 significantly enhances $C_f\sqrt{Re_x}$, with the coefficient increasing from about 7.2% to 17.7%. Similarly, rising the M varies from 0.2 to 0.8 reduces $C_f\sqrt{Re_x}$ from about 6.8% to 5.3%, revealing that stronger magnetic effects decrease the resistive drag along the surface. Furthermore, increasing the porous medium parameter S from 0.1 to 0.9 leads to a reduction in $C_f\sqrt{Re_x}$ from approximately 8.8% to 6.8%, showing that the presence of the porous medium enhances the fluid's resistance but overall decreases the wall shear stress due to reduced fluid velocity near the surface.

Table 4.2 elaborates the behavior of the $\frac{Nu_x}{\sqrt{Re_x}}$ and $\frac{Sh_x}{\sqrt{Re_x}}$ under the influence of various dimensionless parameters in the presence of the porous medium. Increasing the heat source parameter He raises heat transfer by 27.3% and mass transfer by 8.5%. Similarly, higher thermal radiation Nt enhances energy transport, increasing the Nusselt and Sherwood numbers by 12.3% and 27.5%, respectively. An increase in the porous medium parameter S restricts fluid motion, resulting in a 16.5% rise in the $\frac{Nu_x}{\sqrt{Re_x}}$ and 2.1% in the $\frac{Sh_x}{\sqrt{Re_x}}$.

Table 4.3 indicates that a rise in Sb reduces the motile microorganism density, reducing it from approximately 12.4% to 8.5%. Similarly, the motile microorganism number declines with higher values of the Pe. An increase in the motile density parameter Ω also reduces the motile microorganism density, from 11.2% to 5.0%, while an enhancement in the unsteady parameter ϵ results in a small enhancement reaching 4.1

Table 4.4 shows the impact of various parameters on $C_f\sqrt{Re_x}$ in the absence of the porous medium. Enhancing the casson parameter β increases the skin friction

$C_f\sqrt{Re_x}$ from 28.6% to 66.6%. Similarly, higher magnetic parameter M reduces it from 7.5% to 5.6%, and increasing the unsteady parameter ϵ lowers it by up to 7.9%. These decreases occur because higher β weakens the yield stress, larger M slows down the fluid via Lorentz forces, and greater ϵ reduces the momentum transfer at the surface. Table 4.5 shows the effect of different parameters on the $\frac{Nu_x}{\sqrt{Re_x}}$ and $\frac{Sh_x}{\sqrt{Re_x}}$ without the porous medium. Increasing He raises the Nusselt number from 10.8% to 20.5% and Sherwood from 3.5% to 4.7%. Higher Nt increases the Nusselt number by 6.4–10.1% and Sherwood by 20.1–25.8%. Increasing Nb raises Nusselt number up to 10.9% but slightly lowers the Sherwood number by 0.5%. Table 4.6 illustrates the effect of various parameters on the motile microorganism in the absence of a porous medium. Increasing Sb decreases the motile number from 12.5% to 8%, while higher Peclet number Pe reduces it from 18.8% to 13.8%. The motile density parameter Ω lowers the motile number by 5.0%, whereas an increase in ϵ slightly raises it from 2.9% to 3.6%.

TABLE 4.1: The computed $C_f\sqrt{Re_x}$ for multiple values of β, S, M, γ_1, ϵ and ξ_1.

β	M	ϵ	S	γ_1	ξ_1	$C_f\sqrt{Re_x}$
0.3	0.2	0.1	0.1	0.1	0.4	-2.28112
0.5						-1.87561
0.7						-1.67497
0.9						-1.55346
	0.4					-2.43733
	0.6					-2.58314
	0.8					-2.72024
		0.4				-2.45182
		0.8				-2.66663
		1.2				-2.86675
			0.3			-2.43734
			0.6			-2.65265
			0.9			-2.84992
				0.3		-2.02333
				0.6		-1.73464
				0.8		-1.58601
					0.2	-2.27430
					0.6	-2.28712
					0.8	-2.29251

TABLE 4.2: The $\frac{Nu_x}{\sqrt{Re_x}}$ and $\frac{Sh_x}{\sqrt{Re_x}}$ for multiple values of S, N_R, He, Ec, Nb, Nt, Sc and β when $Pr = 6$, $Wi = 0.3$, $\gamma_1 = 0.1$, $\epsilon = 0.1$ and $\xi_1 = 0.4$.

ϵ	H_e	Nt	N_R	Nb	Ec	S	M	β	Sc	$\frac{Nu_x}{\sqrt{Re_x}}$	$\frac{Sh_x}{\sqrt{Re_x}}$
0.1	0.1	0.05	0.2	0.05	0.2	0.1	0.2	0.3	1.2	0.10878	0.75394
0.2										0.09254	0.72428
0.3										0.07184	0.68425
0.4										0.02756	0.59186
	0.5									0.12413	0.72581
	0.15									0.09016	0.78803
	0.2									0.06713	0.83024
		0.15								0.10068	0.93596
		0.25								0.09127	1.18100
		0.35								0.08007	1.50526
			0.3							0.11083	0.74698
			0.4							0.11259	0.74084
			0.5							0.11412	0.73541
				0.1						0.09933	0.72662
				0.15						0.08912	0.71792
				0.2						0.07807	0.71387
					0.05					0.20909	0.57595
					0.1					0.17584	0.63499
					0.15					0.14241	0.69432
						0.2				0.09466	0.77019
						0.3				0.08094	0.78572
						0.4				0.06756	0.80056
							0.4			0.08094	0.78572
							0.6			0.05449	0.81478
							0.8			0.02919	0.84148
								0.5		0.10916	0.69735
								0.7		0.11665	0.65251
								0.9		0.12124	0.62141
									1.4	0.09382	0.84728
									1.6	0.09308	0.91808
									1.8	0.09246	0.98382

TABLE 4.3: The Motile number $\frac{Nn_x}{\sqrt{Re_x}}$ for distinct values of Sb, ϵ, Pe and ω when $M = Nr = 0.2$, $Wi = \gamma_1 = Ec = Bi = 0.3$, $Nb = Nt = 0.05$, $He = 0.1$, $Sc = 1.2$, $Pr = 6.$ and $\xi_1 = 0.4$.

Sb	ϵ	Pe	Ω	$\frac{Nn_x}{\sqrt{Re_x}}$
0.3	0.1	0.2	0.3	0.45014
0.4				0.50634
0.5				0.55825
0.6				0.60616
	0.15			0.43532
	0.2			0.41943
	0.25			0.40221
		0.3		0.53570
		0.4		0.62176
		0.5		0.70828
			0.5	0.47546
			0.7	0.50077
			0.9	0.52609

TABLE 4.4: The computed skin friction coefficients $C_f\sqrt{Re_x}$ for distinct values of β, M, γ_1, ϵ and ξ_1 in the absence of porous medium ($S = 0$).

β	M	ϵ	γ_1	ξ_1	$C_f\sqrt{Re_x}$
0.3	0.2	0.1	0.1	0.4	-2.19847
0.5					-1.80758
0.7					-1.61427
0.9					-1.49721
	0.4				-2.36065
	0.6				-2.51142
	0.8				-2.65269
		0.4			-2.37526
		0.8			-2.59727
		1.2			-2.80325
			0.3		-1.95306
			0.6		-1.67761
			0.9		-1.60324
				0.2	-2.19223
				0.6	-2.20420
				0.8	-2.20901

TABLE 4.5: The results of $\frac{Nu_x}{\sqrt{Re_x}}$ and $\frac{Sh_x}{\sqrt{Re_x}}$ for various values of S, N_R, He, Ec, Nb, Nt, Sc and β in the lack of porous medium ($S = 0$), when $Pr = 6$, $Wi = 0.3$, $\gamma_1 = 0.1$, $\epsilon = 0.1$ and $\xi_1 = 0.4$.

ϵ	H_e	Nt	N_R	Nb	Ec	M	β	Sc	$\frac{Nu_x}{\sqrt{Re_x}}$	$\frac{Sh_x}{\sqrt{Re_x}}$
0.1	0.1	0.05	0.2	0.05	0.2	0.2	0.3	1.2	0.11559	0.77427
0.2									0.10042	0.74832
0.3									0.08172	0.71522
0.4									0.06152	0.65328
	0.5								0.12954	0.74812
	0.15								0.09891	0.80556
	0.2								0.07862	0.84366
		0.15							0.10819	0.94323
		0.25							0.09964	1.17090
		0.35							0.08956	1.47149
			0.3						0.11751	0.76756
			0.4						0.11916	0.76166
			0.5						0.12058	0.75643
				0.1					0.10658	0.74946
				0.15					0.09684	0.74157
				0.2					0.08630	0.73794
					0.05				0.21213	0.59974
					0.1				0.18013	0.65764
					0.15				0.14795	0.71582
						0.4			0.08503	0.81382
						0.6			0.05590	0.85052
						0.8			0.02795	0.88474
							0.5		0.12719	0.11531
							0.7		0.13322	0.67869
							0.9		0.13695	0.65315
								1.4	0.11487	0.85220
								1.6	0.11426	0.92389
								1.8	0.11372	0.99055

TABLE 4.6: The results of the Motile number $\frac{Nn_x}{\sqrt{Re_x}}$ for values of Sb, ϵ, Pe and ω in the absence of porous medium ($S = 0$), when $M = Nr = 0.2$, $Wi = \gamma_1 = Ec = 0.3$, $Nb = Nt = 0.05$, $He = 0.1$, $Sc = 1.2$, $Pr = 6$. $Bi = 0.3$ and $\xi_1 = 0.4$.

Sb	ϵ	Pe	Ω	$\frac{Nn_x}{\sqrt{Re_x}}$
0.3	0.1	0.2	0.3	0.46881
0.4				0.52739
0.5				0.58107
0.6				0.63041
	0.15			0.45501
	0.2			0.44026
	0.25			0.42439
		0.3		0.55717
		0.4		0.64607
		0.5		0.73546
			0.5	0.49491
			0.7	0.52101
			0.9	0.54711

4.5.2 Velocity Profile

Analyzing the velocity distributions is fundamental for understanding the behavior and characteristics of the fluid flow, as it provides insight into how the fluid responds to various forces and boundary conditions.Figure 4.2 depicts the effects of the M on the velocity profile of the unsteady Casson fluid flowing over a stretching sheet in a porous medium. It is seen that as the value of M increases, the fluid velocity decreases throughout the boundary layer. This reduction is owing to the Lorentz force generated by the applied magnetic field, which acts opposite to the fluid motion and resists the stretching of the sheet. Consequently, the momentum

boundary layer thickness is reduced. Additionally, a combination of the porous medium and magnetic field enhances the resistive forces, further slowing down the fluid near the wall.

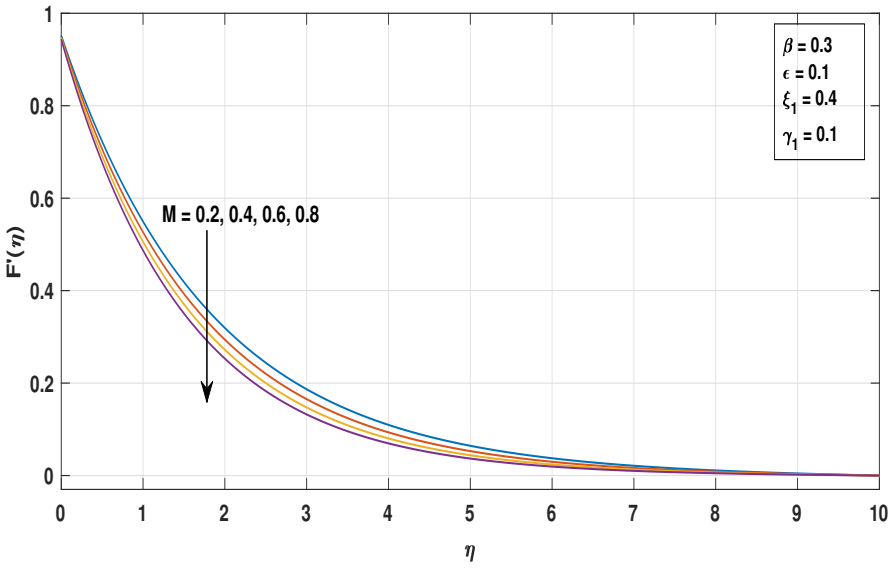

FIGURE 4.2: Impact of M on velocity profile $f'(\eta)$

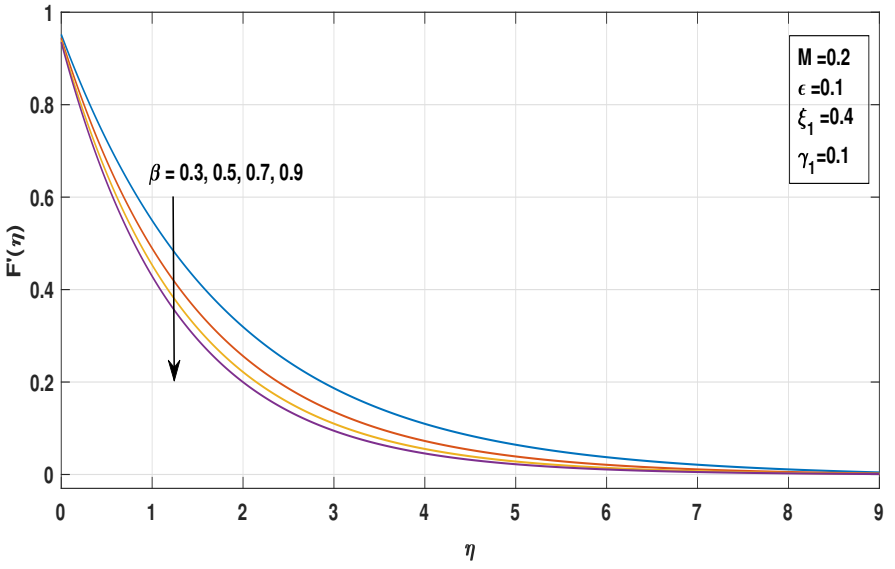

FIGURE 4.3: Impact of β on velocity profile $f'(\eta)$

The contribution of the Casson parameter β on the velocity profile is illustrated in Figure 4.3. Higher values of β represent a stronger non-Newtonian behavior, causing the fluid to resist the motion more effectively. Consequently, the velocity

near the stretching sheet decreases and the momentum boundary layer becomes thinner, highlighting the role of yield stress in controlling the flow characteristics.

Similarly, Figure 4.4 illustrates the effect of the unsteady parameter ϵ on the velocity of the Casson fluid. As ϵ increases, the velocity decreases because unsteady flow introduces additional resistance, slowing down the fluid near the stretching surface.

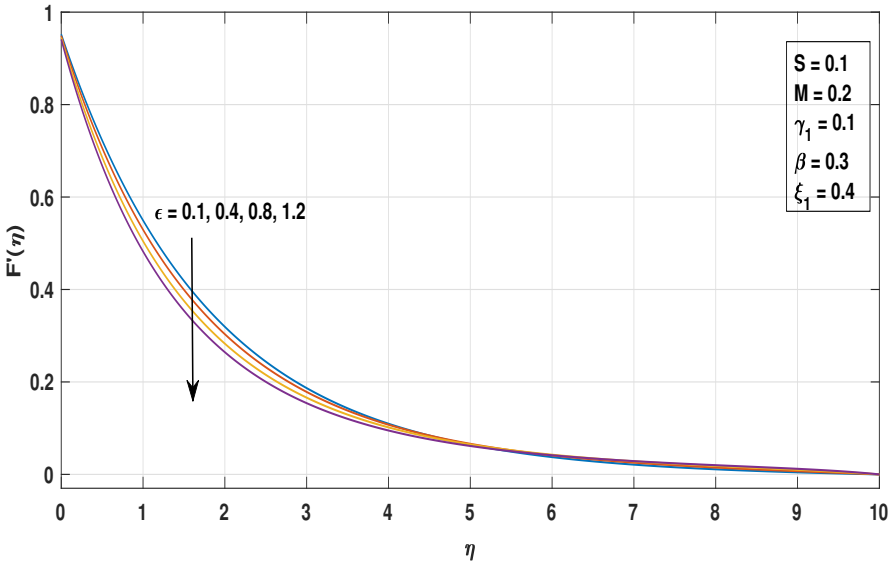

FIGURE 4.4: Impact of ϵ on velocity profile $f'(\eta)$

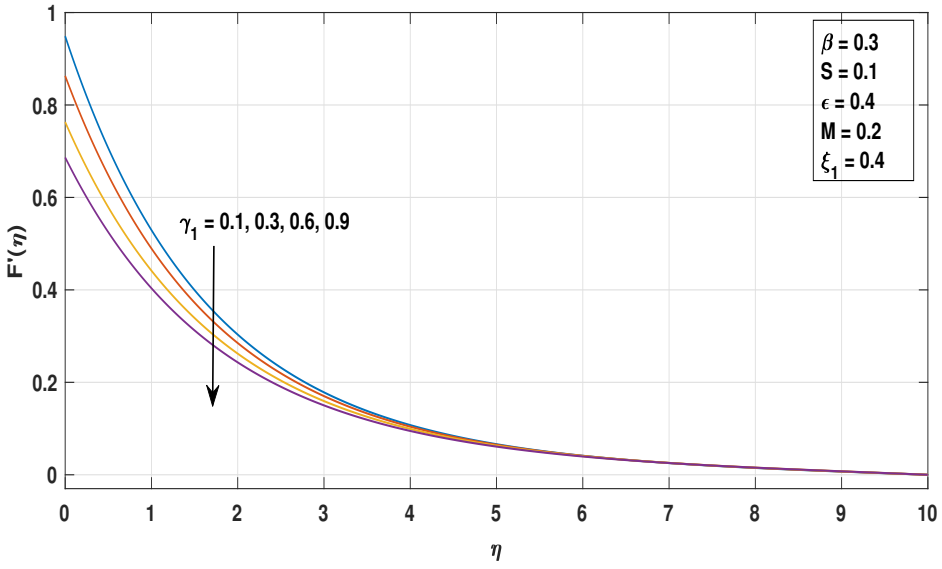

FIGURE 4.5: Impact of γ_1 on velocity profile $f'(\eta)$

The effect of the slip parameter γ_1 on the velocity profile is illustrated in Figure 4.5. In the case of unsteady Casson fluid flow over a stretching sheet in a porous medium, increasing γ_1 enhances the slip at the boundary, which reduces the transfer of momentum from sheet to the fluid. As a result, the velocity near the sheet decreases, and the overall velocity profile within the boundary layer diminishes. This demonstrates that higher slip reduces the effectiveness of the stretching surface in driving the fluid motion. The outcome of the porous medium parameter S on the velocity profile is illustrate in Figure 4.6. An increase in S causes stronger resistance offered by the porous medium to the fluid motion. As a result, the velocity profile decreases throughout the boundary layer, indicating that higher porous medium effects suppress the flow.

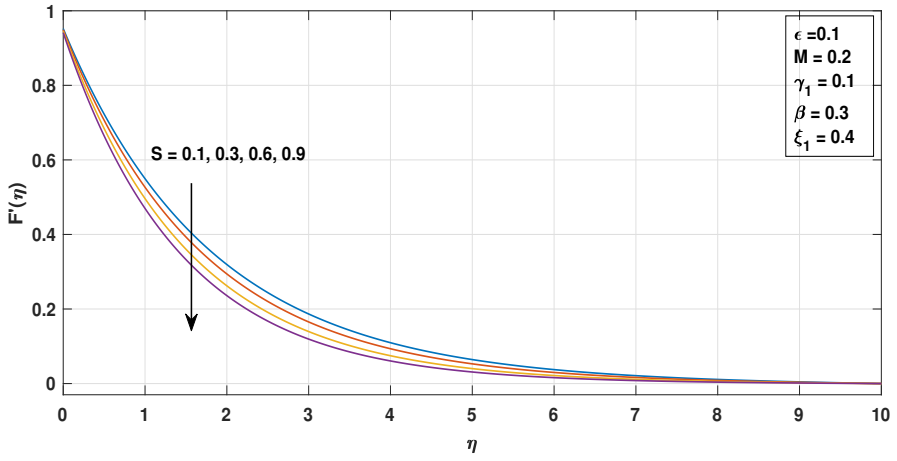

FIGURE 4.6: Outcome of S on velocity profile $f'(\eta)$

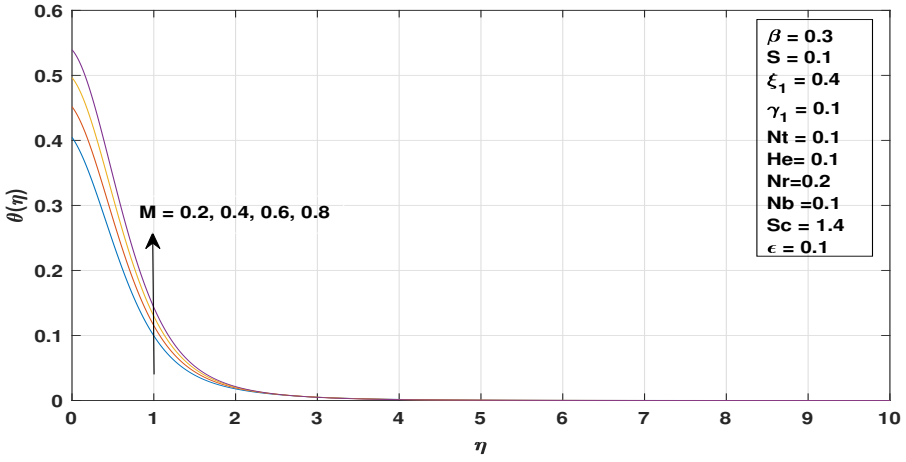

FIGURE 4.7: Outcome of M on Temperature profile $\theta(\eta)$

4.5.3 Temperature Profile

The temperature distribution shows down the heat transfer characteristics of the unsteady Casson fluid over a stretching sheet in a porous medium.As shown in Figure 4.7, increasing the magnetic parameter M leads to a rise in the temperature profile. This occurs because a stronger magnetic field generates additional resistive forces (Lorentz force) in the fluid, which converts part of the kinetic energy into heat, thereby increasing the fluid temperature throughout the boundary layer.

In Figure 4.8, it is evident that increasing the heat source parameter He raises the temperature profile. This happens because a higher He represents additional energy being added directly to the fluid, which increases the thermal energy and results in a higher temperature throughout the boundary layer. As shown in Figure 4.9, a hike in the thermal radiation parameter Nr raises the temperature profile. This occurs because thermal radiation adds energy to the fluid in the form of radiative heat flux. A higher Nr means more energy is radiated into the fluid, which increases the thermal energy inside the boundary layer. Hence, the fluid temperature rises, and the temperature gradients near the stretching sheet becomes stronger, reflecting enhanced heat transfer due to radiation.

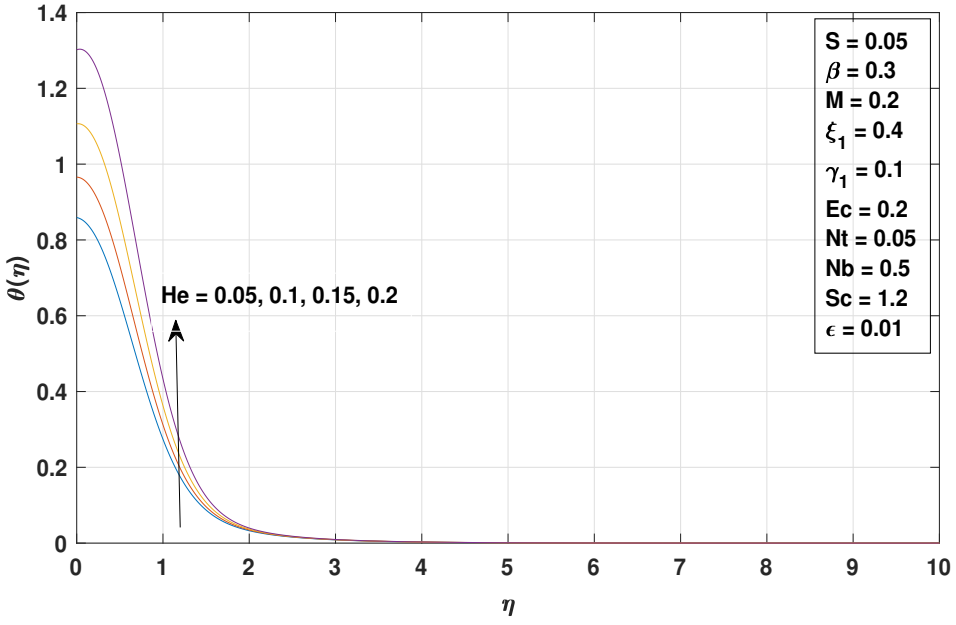

FIGURE 4.8: Outcome of He on Temperature profile $\theta(\eta)$

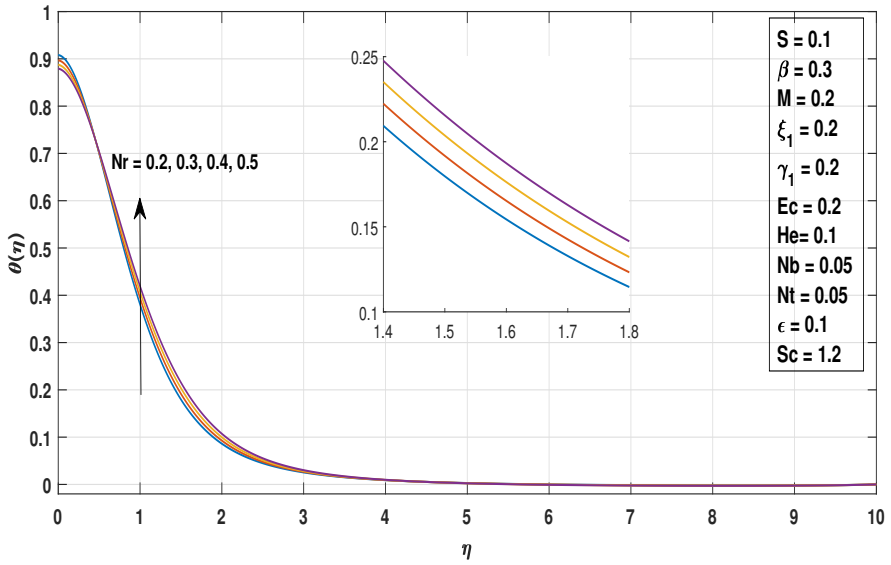

FIGURE 4.9: Outcome of Nr on Temperature profile $\theta(\eta)$

Figure 4.10 illustrates that increasing the Brownian motion parameter Nb raises the temperature profile. Stronger Brownian motion increases the random movement of nanoparticles, which transfers more energy to the fluid and increases its thermal energy throughout the boundary layer. This enhanced energy exchange not only raises the fluid temperature near the stretching sheet but also affects the temperature distribution across the entire boundary layer. Consequently, higher Nb values result in a thicker thermal boundary layer and stronger heat transfer within the fluid. Similarly, Figure 4.11 shows that increasing the Nt raises the Figure 4.10 illustrates that increasing the Brownian motion parameter Nb raises the temperature profile. Stronger Brownian motion increases the random movement of nanoparticles, which transfers more energy to the fluid and increases its thermal energy throughout the boundary layer. This enhanced energy exchange not only raises the fluid temperature near the stretching sheet but also affects the temperature distribution across the entire boundary layer. Consequently, higher Nb values result in a thicker thermal boundary layer and stronger heat transfer within the fluid. Similarly, Figure 4.11 shows that increasing the Nt raises the temperature profile. Higher Nt enhances the movement of nanoparticles from hotter to cooler regions, which increases energy transfer within the fluid. Hence, the fluid temperature rises throughout the boundary layer, resulting in a thicker thermal boundary layer and stronger heat transfer.

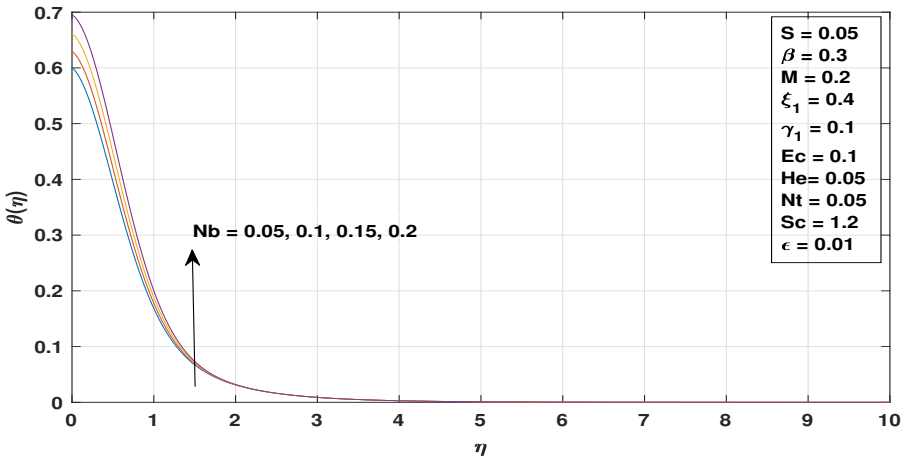

FIGURE 4.10: Outcome of Nb on Temperature profile $\theta(\eta)$

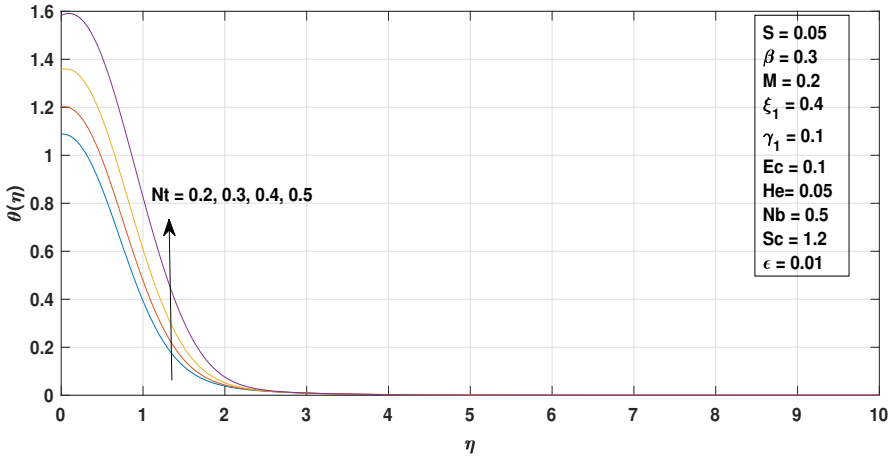

FIGURE 4.11: Outcome of Nt on Temperature profile $\theta(\eta)$

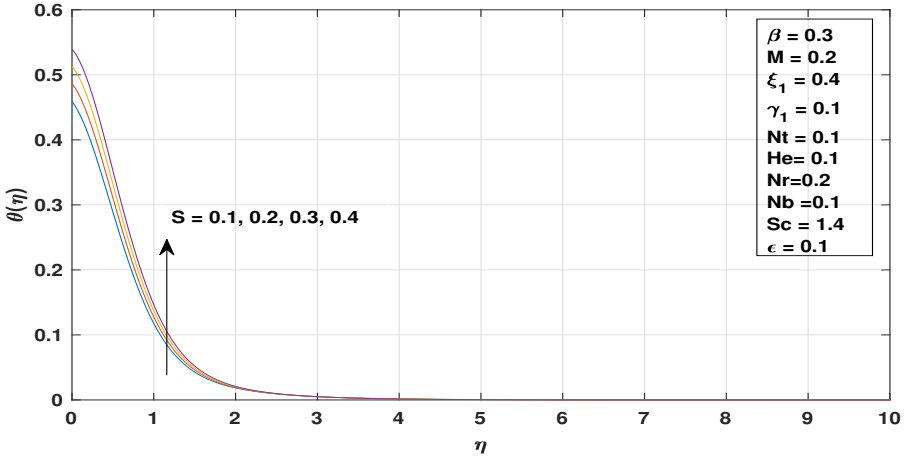

FIGURE 4.12: Outcome of S on Temperature profile $\theta(\eta)$

Figure 4.12 reveals that growth in the porous medium parameter S raises the

temperature profile. This happens because a higher S increases the resistance to fluid flow within the porous medium, which decrease the fluid motion. Slower fluid motion reduces convective heat transfer away from the sheet, so more heat stays in the fluid, leading to higher temperatures throughout the boundary layer.

In the same way, Figure 4.13 illustrates that increasing the Sc increases the temperature profile. Higher Sc reduces the rate of mass diffusion, which allows more energy to remain in the fluid as thermal energy, raising the fluid temperature across the boundary layer.

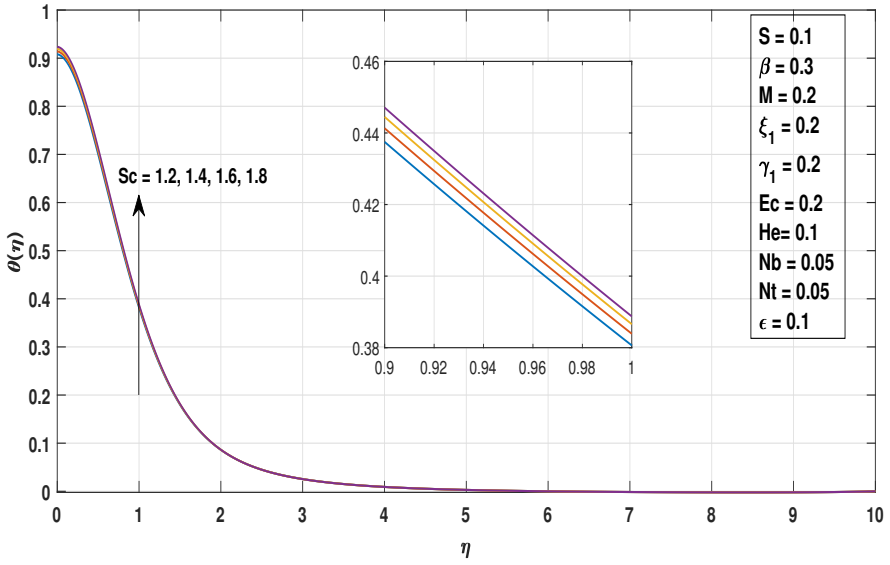

FIGURE 4.13: Outcome of Sc on Temperature profile $\theta(\eta)$

Figure 4.14 shows that enhancing the Casson fluid parameter β decreases the temperature profile. Higher β strengthens the non-Newtonian nature of the fluid, increasing its resistance to motion.

This increased resistance reduces the fluid velocity, which in turn weakens viscous dissipation within the boundary layer. As a result, less thermal energy is generated, lowering the fluid temperature.

Additionally, the reduction in momentum near the stretching sheet decreases convective heat transfer, leading to a narrower thermal boundary layer and an overall drop in temperature across the flow.

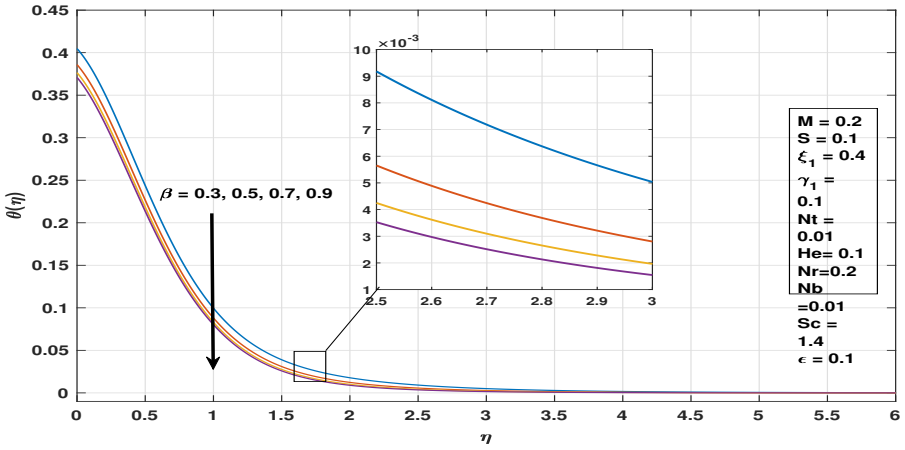

FIGURE 4.14: Outcome of β on Temperature profile $\theta(\eta)$

4.5.4 Concentration Profile

The concentration distribution provides insight into the mass transfer behavior of the unsteady Casson fluid over a stretching sheet in a porous medium. Figure 4.15 shows that increasing the Casson parameter β increases the concentration profile. Higher β strengthens the non-Newtonian behavior of the fluid, increasing resistance to flow within the porous medium. This slows down the fluid motion near the stretching sheet, which reduces the transport of concentration away from the surface. As a result, the concentration remains higher throughout the boundary layer, leading to a thicker concentration boundary layer. Consequently, higher β values allow more accumulation in the fluid close to the surface.

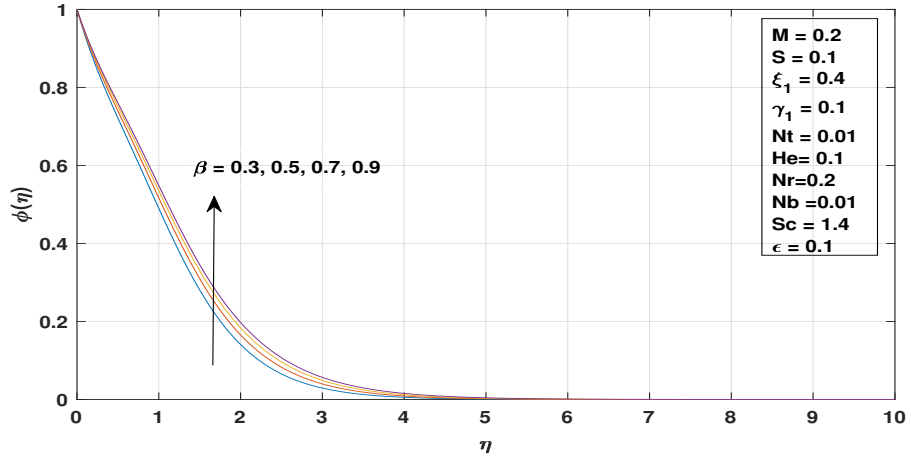

FIGURE 4.15: Influence of β on Concentration profile $\phi(\eta)$

Figure 4.16 illustrates the influence of the Eckert number Ec on the concentration profile of the unsteady Casson fluid over a stretching sheet in a porous medium. It is observed that increasing Ec leads to a rise in the concentration profile. Higher viscous dissipation adds energy to the fluid, which enhances the concentration throughout the boundary layer. The increased energy also slows down the relative motion near the surface, allowing the concentration to remain higher across the boundary layer.

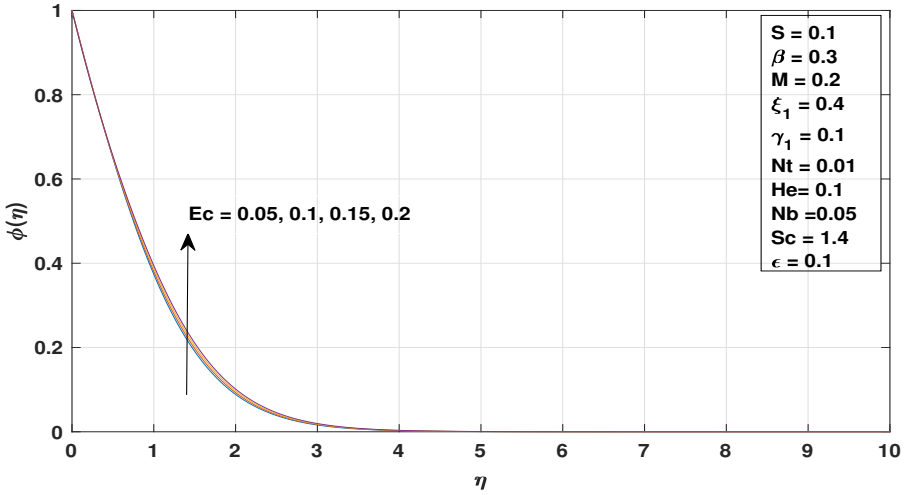

FIGURE 4.16: Effect of Ec on Concentration profile $\phi(\eta)$

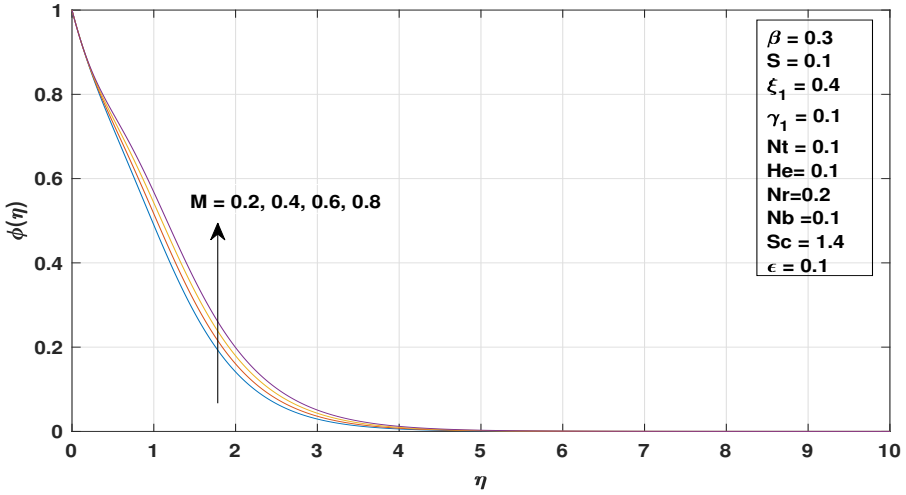

FIGURE 4.17: Influence of M on Concentration profile $\phi(\eta)$

Similarly, Figure 4.17 shows the effect of the magnetic parameter M on the concentration profile. Increasing M introduces more resistance to fluid motion, which

reduces the fluid velocity near the stretching sheet. As a result, the concentration stays higher close to the surface and throughout the boundary layer. Both parameters, Ec and M, therefore contribute to increasing the concentration, reflecting the combined influence of viscous dissipation and magnetic resistance on the flow behavior. Figure 4.18 shows the effect of the parameter He on the concentration profile of the unsteady Casson fluid over a stretching sheet in a porous medium. It is observed that increasing He leads to a rise in the concentration profile. Higher values of He add more energy to the fluid, which enhances the accumulation of concentration within the boundary layer. This additional energy slows down the relative movement of the fluid near the surface, allowing the concentration to remain higher across the boundary layer. Consequently, higher He values result in a thicker concentration boundary layer, indicating stronger retention of concentration close to the stretching sheet.

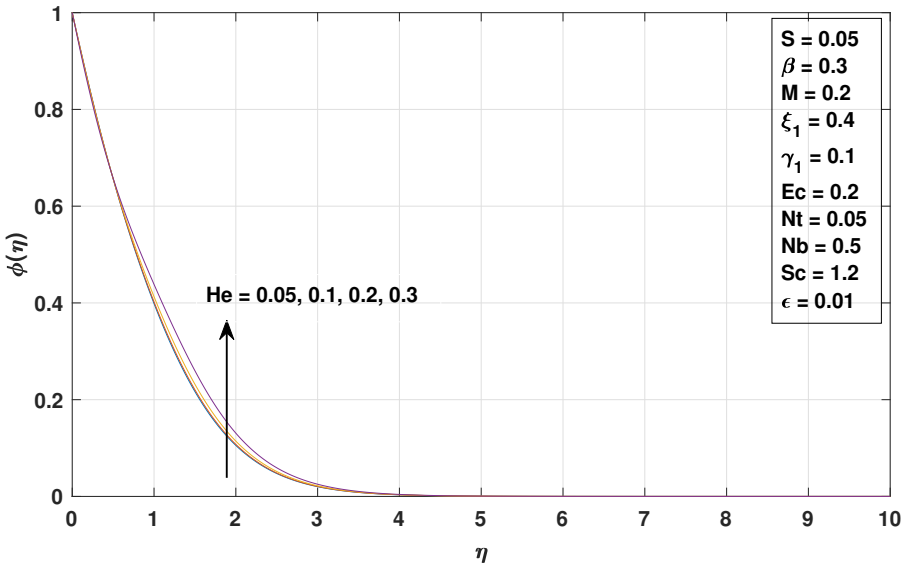

FIGURE 4.18: Outcome of He on Concentration profile $\phi(\eta)$

Figure 4.19 shows the outcome of the Brownian motion parameter Nb on the concentration profile of the unsteady Casson fluid over a stretching sheet in a porous medium. It is observed that increasing Nb decreases the concentration profile. Higher Brownian motion enhances the random movement of particles in the fluid, which spreads the concentration more evenly and reduces its accumulation near the surface.

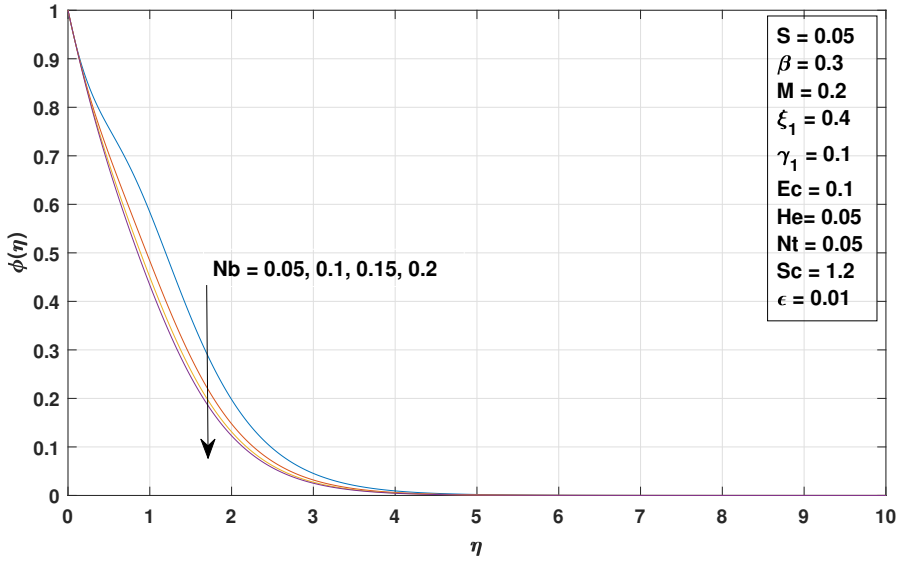

FIGURE 4.19: Outcome of Nb on Concentration profile $\phi(\eta)$

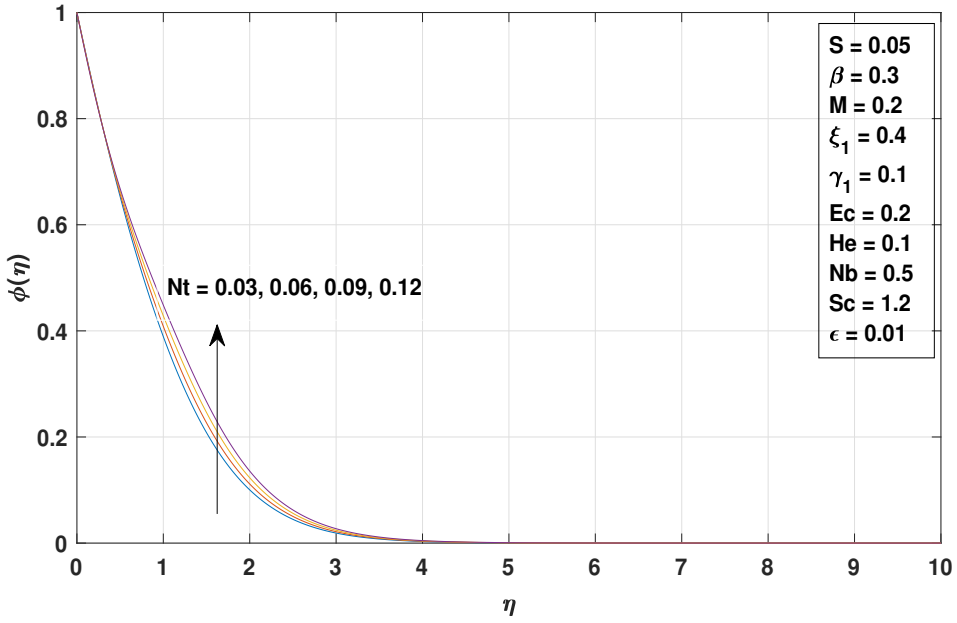

FIGURE 4.20: Impact of Nt on Concentration profile $\phi(\eta)$

This increased dispersion lowers the overall concentration within the boundary layer, resulting in a thinner concentration layer as Nb increases. Similarly, Figure 4.20 illustrates the effect of the Nt on the concentration profile. Increasing Nt leads to a rise in the concentration throughout the boundary layer. Stronger thermophoretic effects cause particles to move from hotter to cooler regions more

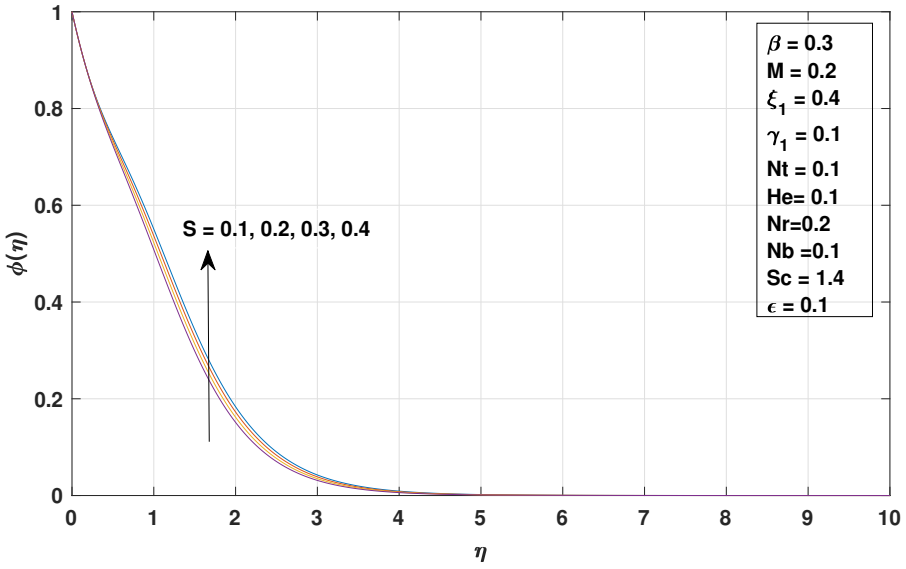

FIGURE 4.21: Impact of S on Concentration profile $\phi(\eta)$

effectively, slowing their overall diffusion away from the surface. As a result, more concentration is retained near the stretching sheet, and the concentration boundary layer becomes thicker with increasing Nt. Figure 4.21 shows that increasing the S raises the concentration profile. Higher S slows down the fluid flow near the stretching sheet, reducing the transport of concentration away from the surface. As a result, the concentration remains higher throughout the boundary layer. Figure 4.22 shows that increasing the Schmidt number Sc decreases the concentration profile of the unsteady Casson fluid over a stretching sheet in a porous medium. A higher Sc corresponds to lower mass diffusivity, meaning the concentration spreads more slowly in the fluid. This reduced diffusion limits the accumulation of concentration near the surface, resulting in a lower concentration throughout the boundary layer. As a result, the concentration boundary layer becomes thinner as Sc increases, indicating that higher Schmidt numbers restrict the transport of concentration away from the surface.

4.5.5 Motile Density Profile

The motile density profile represents the distribution of swimming microorganisms in the fluid. Examining this profile provides insight into how the fluid flow and

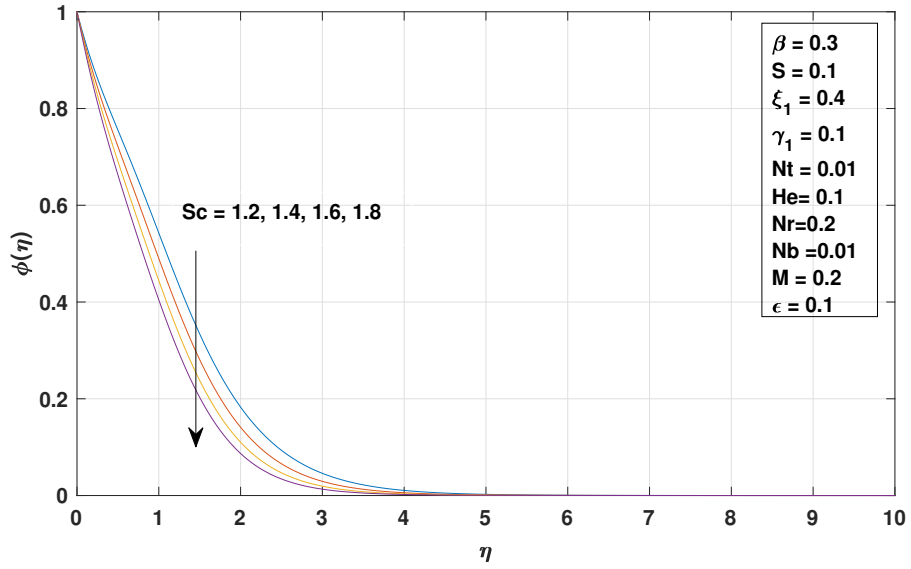

FIGURE 4.22: Impact of Sc on Concentration profile $\phi(\eta)$

boundary conditions affect the movement of microorganisms.Figure 4.23 represents that an increase in the bioconvection Schmidt number Sb causes a reduction in the motile density profile. This occurs because larger Sb values indicate weaker microorganism diffusion, limiting their movement within the flow region. Figure 4.24 illustrates that increasing the Peclet number Pe decreases the motile density profile. Higher Pe represents stronger advection relative to diffusion, which enhances the transport of motile microorganisms away from the surface. As a result, fewer microorganisms remain near the stretching sheet, leading to a thinner motile density layer throughout the boundary layer.

Figure 4.25 shows that as the motile density parameter Ω increases, the motile number decreases. This happens because a higher Ω reduces the difference in microorganism concentration between the wall and the fluid, so fewer microorganisms gather near the surface.

Figure 4.26 illustrates that increasing the unsteady parameter ϵ leads to a rise in the motile density profile. Higher ϵ represents stronger unsteady effects in the flow, which reduce the relative movement of the fluid near the surface. This slower fluid motion allows more motile microorganisms to remain close to the stretching sheet, resulting in a thicker motile density layer throughout the boundary layer.

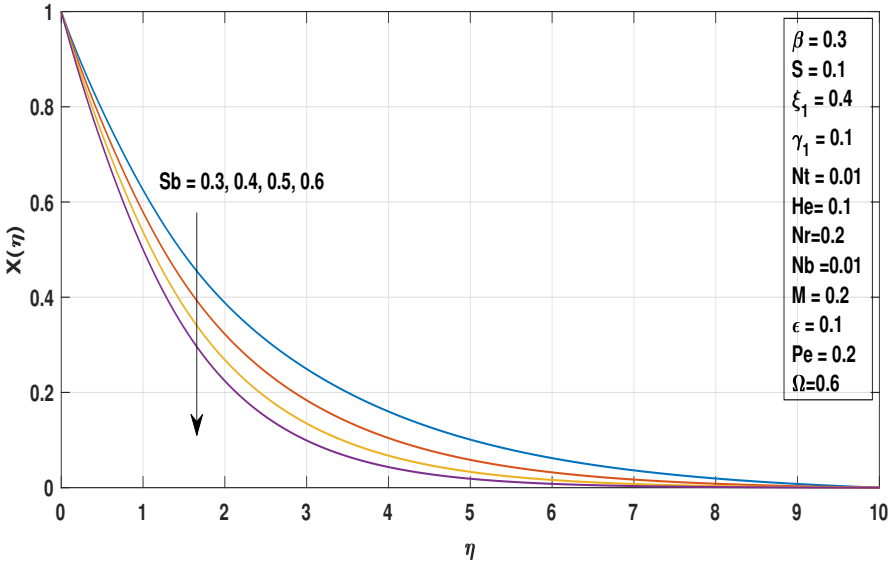

FIGURE 4.23: Result of Sb on Motile density profile $\phi(\eta)$

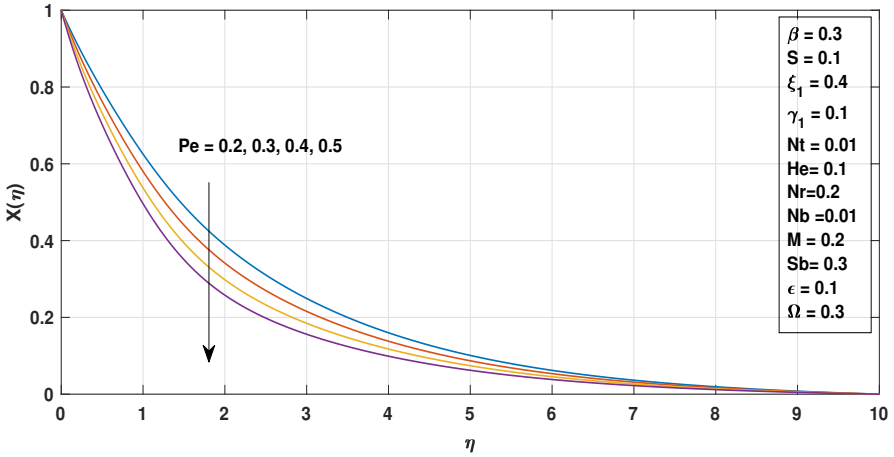

FIGURE 4.24: Outcome of Pe on Motile density profile $\phi(\eta)$

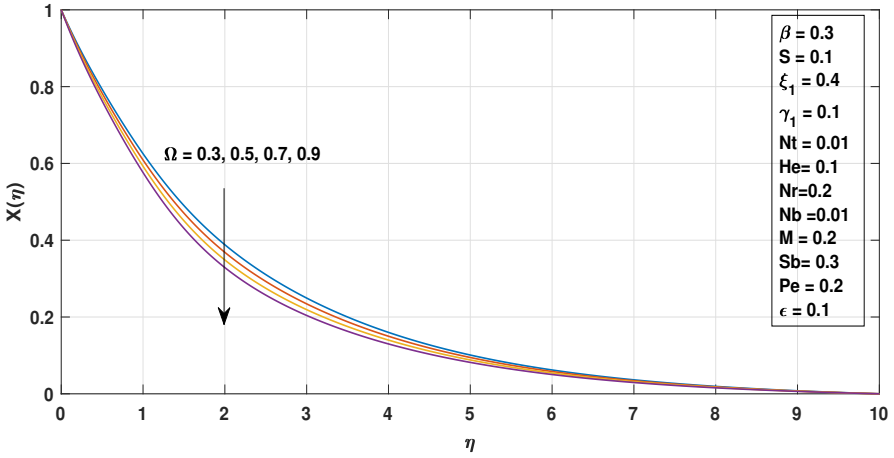

FIGURE 4.25: Impact of Ω on Motile density profile $\phi(\eta)$

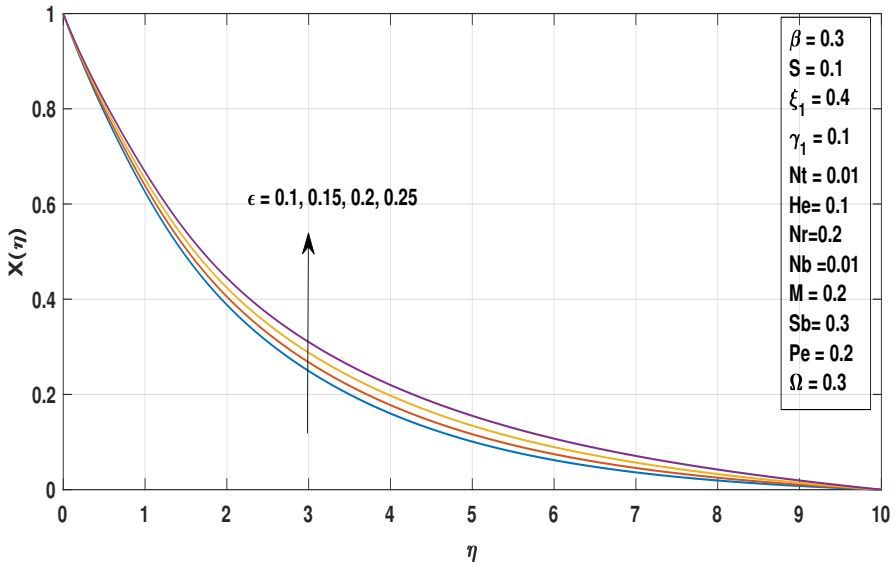

FIGURE 4.26: Impact of ϵ on Motile density profile $\phi(\eta)$

Chapter 5

Conclusion

An in-depth analysis is carried out to examine the behavior of Williamson and Casson non-Newtonian fluids over stretching sheets, including the effects of Prandtl number (Pr), Brownian parameter (Nb), Eckert number (Ec), Williamson parameter (Wi), thermophoresis parameter (Nt), magnetic parameter (M), Peclet number (Pe) and Biot number (Bi).

5.1 Key Findings on the Flow Behavior of Casson Fluid with Porous Medium

i. For Williamson fluid, higher Pe and Ω reduce the motile profile by limiting the transport of microorganisms. In Casson fluid with a porous medium, both Pe and Ω also decrease the motile profile.

ii. Increasing the Casson parameter β reduces the fluid velocity due to higher resistance to flow. As a result, the concentration increases because the slower fluid allows more accumulation of nanoparticles.

5.2 Key Findings on the Flow Behavior of Williamson Fluid

i. Increasing the Sc reduces the concentration distribution in Williamson fluid due to lower mass diffusivity, which limits the nanoparticles movement.

ii. The temperature distribution is showing decreasing trend by rising heat generation and radiation effect in Williamson fluid.

5.3 Comparative Analysis of Williamson and Casson Fluid Models

i. Increasing the magnetic field strength reduces the skin friction coefficient in both fluids. For the Williamson fluid, it decreases from 6.5% to 2.6%, while for the Casson fluid it declines from 7.5% to 5.6%, due to the opposing Lorentz force that resists the fluid motion.

ii. $C_f\sqrt{Re_x}$ decreases with higher values of ϵ in both fluids. Williamson fluid experiences a reduction of up to 2.5%, while Casson fluid shows a decrease of up to 7.9%, as stronger unsteady effects reduce the fluid velocity.

iii. Higher values of He significantly enhance heat transfer in both fluids. The Nusselt number rises up to 53.9% for Williamson fluid and reaches 20.5% for Casson fluid reflecting the stronger thermal energy supplied to the system.

iv. Increasing Nt raises Sherwood number in both Williamson and Casson fluids by enhancing mass transfer. In contrast, higher Nb slightly lowers Sherwood numbers by reducing the concentration near the surface. Thus, Nt improves mass transfer, while Nb slightly limits it.

5.4 Effect of Porous and Non-Porous Medium on Casson Fluid Flow

i. Increasing the Ec enhances the temperature profile in the Casson fluid, increasing by 23.6% in the presence of a porous medium and by 21.9% in its absence. Conversely, the concentration profile decreases from 10.2% to 8.5% with a porous medium and from 9.7% to 8.2% without a porous medium.

ii. Increasing thermophoresis parameter enhances the concentration profile in the Casson fluid, rising by 27.5% with a porous medium and 25.7% without, indicating stronger mass transfer when porous resistance is present.

Bibliography

[1] R. V. Williamson, "The flow of pseudoplastic materials," *Industrial & Engineering Chemistry*, vol. 21, no. 11, pp. 1108–1111, 1929.

[2] T. Salahuddin, S. Tariq, M. Khan, M. Awais, and M. Afzal, "Electro-osmotic analysis of Williamson fluid model with viscous dissipation and enthalpy," *Results in Engineering*, vol. 25, p. 103635, 2025.

[3] N. Shashikumar, M. Madhu, S. Sindhu, B. Gireesha, and N. Kishan, "Thermal analysis of MHD Williamson fluid flow through a microchannel," *International Communications in Heat and Mass Transfer*, vol. 127, p. 105582, 2021.

[4] Y. B. Kho, A. Hussanan, M. K. A. Mohamed, and M. Z. Salleh, "Heat and mass transfer analysis on flow of Williamson nanofluid with thermal and velocity slips: Buongiorno model," *Propulsion and Power Research*, vol. 8, no. 3, pp. 243–252, 2019.

[5] M. Hamid, M. Usman, Z. Khan, R. U. Haq, and W. Wang, "Numerical study of unsteady MHD flow of Williamson nanofluid in a permeable channel with heat source/sink and thermal radiation," *The European Physical Journal Plus*, vol. 133, no. 12, p. 527, 2018.

[6] M. Bibi, M. Malik, and M. Tahir, "Numerical study of unsteady Williamson fluid flow and heat transfer in the presence of MHD through a permeable stretching surface," *The European Physical Journal Plus*, vol. 133, no. 4, p. 154, 2018.

[7] B.V.Kumar, T. Poornima, P. Sreenivasulu, and A. Subba Rao, "Effect of inclined Lorentzian force on radiated nanoflow Williamson model under asymmetric energy source/sink: Keller box method," *Apl. Mater*, vol. 12, p. 041106, 2024.

[8] T. H. Al-Arabi, N. S. Elgazery, and A. F. Elelamy, "Transient MHD darcy-forchheimer of Williamson-Casson flow with ccs: Application of wastewater treatment," *Advances in Mechanical Engineering*, vol. 16, no. 4, p. 16878132241245832, 2024.

[9] P. Supriya and B. Pullepu, "Numerical investigation of unsteady Casson–Williamson nanofluids in a non-isothermal radiated vertical cone with joule and chemical effects," *Numerical Heat Transfer, Part A: Applications*, pp. 1–19, 2025.

[10] N. Casson, "Flow equation for pigment-oil suspensions of the printing ink-type," *Rheology of disperse systems*, pp. 84–104, 1959.

[11] I. S. Oyelakin, S. Mondal, and P. Sibanda, "Unsteady Casson nanofluid flow over a stretching sheet with thermal radiation, convective and slip boundary conditions," *Alexandria engineering journal*, vol. 55, no. 2, pp. 1025–1035, 2016.

[12] M. Hamid, M. Usman, Z. Khan, R. Ahmad, and W. Wang, "Dual solutions and stability analysis of flow and heat transfer of Casson fluid over a stretching sheet," *Physics Letters A*, vol. 383, no. 20, pp. 2400–2408, 2019.

[13] M. Das, G. Mahanta, and S. Shaw, "Heat and mass transfer effect on an unsteady MHD radiative chemically reactive Casson fluid over a stretching sheet in porous medium," *Heat Transfer*, vol. 49, no. 8, pp. 4350–4369, 2020.

[14] S. Reza-E-Rabbi, S. Arifuzzaman, T. Sarkar, M. S. Khan, and S. F. Ahmmed, "Explicit finite difference analysis of an unsteady MHD flow of a chemically reacting Casson fluid past a stretching sheet with Brownian motion and thermophoresis effects," *Journal of King Saud University-Science*, vol. 32, no. 1, pp. 690–701, 2020.

[15] F. Faraz, S. M. Imran, B. Ali, and S. Haider, "Thermo-diffusion and multi-slip effect on an axisymmetric casson flow over a unsteady radially stretching sheet in the presence of chemical reaction," *Processes*, vol. 7, no. 11, p. 851, 2019.

[16] D. Srinivasacharya and R. S. Kumar, "Artificial neural network modeling of the Casson fluid flow over unsteady radially stretching sheet with Soret and Dufour effects.," *Journal of Thermal Analysis & Calorimetry*, vol. 147, no. 24, 2022.

[17] H. Abdel-Gawad, "Dynamics of steady, unsteady flows and heat transfer in Casson fluid over a free stretching surface: stability analysis," *Waves in Random and Complex Media*, pp. 1–19, 2023.

[18] A. Megahed, "Effect of slip velocity on Casson thin film flow and heat transfer due to unsteady stretching sheet in presence of variable heat flux and viscous dissipation," *Applied Mathematics and Mechanics*, vol. 36, no. 10, pp. 1273–1284, 2015.

[19] C. Raju and N. Sandeep, "Unsteady three-dimensional flow of Casson–Carreau fluids past a stretching surface," *Alexandria Engineering Journal*, vol. 55, no. 2, pp. 1115–1126, 2016.

[20] S. Rehman, M. Idrees, R. A. Shah, and Z. Khan, "Suction/injection effects on an unsteady MHD Casson thin film flow with slip and uniform thickness over a stretching sheet along variable flow properties," *Boundary Value Problems*, vol. 2019, no. 1, p. 26, 2019.

[21] K. G. Kumar, N. Rudraswamy, B. Gireesha, and S. Manjunatha, "Non linear thermal radiation effect on Williamson fluid with particle-liquid suspension past a stretching surface," *Results in Physics*, vol. 7, pp. 3196–3202, 2017.

[22] T. Hayat, A. Shafiq, and A. Alsaedi, "Hydromagnetic boundary layer flow of Williamson fluid in the presence of thermal radiation and ohmic dissipation," *Alexandria Engineering Journal*, vol. 55, no. 3, pp. 2229–2240, 2016.

[23] A. M. Megahed, "Williamson fluid flow due to a nonlinearly stretching sheet with viscous dissipation and thermal radiation," *Journal of the Egyptian Mathematical Society*, vol. 27, no. 1, p. 12, 2019.

[24] Hashim, M. Khan, and A. Hamid, "Convective heat transfer during the flow of Williamson nanofluid with thermal radiation and magnetic effects," *The European Physical Journal Plus*, vol. 134, no. 2, p. 50, 2019.

[25] M. Rashidi, M. Ali, N. Freidoonimehr, B. Rostami, and M. A. Hossain, "Mixed convective heat transfer for MHD viscoelastic fluid flow over a porous wedge with thermal radiation," *Advances in Mechanical Engineering*, vol. 6, p. 735939, 2014.

[26] O. S. Balogun, M. Aslam, M. Z. Iqbal, and M. Z. Arshad, "Investigation of gold and silver based hybrid nanofluid with effects of thermal radiation over a stretching sheet," *Alexandria Engineering Journal*, vol. 117, pp. 352–363, 2025.

[27] H. Waqas, M. Hussain, M. Alqarni, M. R. Eid, and T. Muhammad, "Numerical simulation for magnetic dipole in bioconvection flow of Jeffrey nanofluid with swimming motile microorganisms," *Waves in Random and Complex Media*, vol. 34, no. 3, pp. 1958–1975, 2024.

[28] U. Farooq and M. Imran, "Analysis of bio-convection in Casson hybrid nanofluid flow with motile microorganisms and heat transfer using Cattaneo-Christov heat and mass flux theory over a cylinder," *Case Studies in Thermal Engineering*, vol. 69, p. 105960, 2025.

[29] G. M. Moatimid, M. A. Mohamed, and K. Elagamy, "A pulsatile Williamson nanofluid flow with motile microorganisms between two permeable walls: Effect of modified darcy's law," *Journal of Porous Media*, vol. 26, no. 12, 2023.

[30] E. A. Algehyne and A. Saeed, "Numerical study of motile microorganism in Williamson mhd nanofluid flow over an elastic slender surface of an irregular thickness," *Waves in Random and Complex Media*, pp. 1–16, 2022.

[31] M. S. Nadeem, S. Riaz, H. S. Abid, Q. Ali, and U. Younas, "Bioconvection in Williamson hybrid nanofluid with thermal radiation, chemical reactions, and motile microorganisms on stretched surface," *Modern Physics Letters B*, vol. 39, no. 08, p. 2450429, 2025.

[32] T. Muhammad, H. Waqas, U. Manzoor, U. Farooq, and Z. F. Rizvi, "On doubly stratified bioconvective transport of Jeffrey nanofluid with gyrotactic motile microorganisms," *Alexandria Engineering Journal*, vol. 61, no. 2, pp. 1571–1583, 2022.

[33] K. Gangadhar, P. M. Seshakumari, M. Venkata Subba Rao, and A. J. Chamkha, "Mhd flow analysis of a williamson nanofluid due to thomson and troian slip condition," *International Journal of Applied and Computational Mathematics*, vol. 8, no. 1, p. 6, 2022.

[34] C. Amanulla, N. Nagendra, and M. Suryanarayana Reddy, "Numerical simulation of slip influence on the flow of a MHD Williamson fluid over a vertical convective surface," *Nonlinear Engineering*, vol. 7, no. 4, pp. 309–321, 2018.

[35] N. Nagendra, C. Amanulla, and M. Sudhakar Reddy, "Slip effects on MHD flow of a Williamson fluid from an isothermal sphere: A numerical study," *Modelling, Measurement and Control B*, vol. 86, no. 3, pp. 782–80, 2017.

[36] M. Ramzan, M. Shahryar, S. Abbas, M. Amir, S. R. Saydaxmetova, R. Jan, A. Al Agha, and H. A. Garalleh, "Heat transfer with magnetic force and slip velocity on non-Newtonian fluid flow through a porous medium," *Partial Differential Equations in Applied Mathematics*, vol. 13, p. 101033, 2025.

[37] T. Abbas, "Magnetohydrodynamic flow of a hybrid nanofluid over an exponentially stretching sheet with Joule heating and slip conditions using spectral collocation method with legendre wavelets," *Multiscale and Multidisciplinary Modeling, Experiments and Design*, vol. 8, no. 1, p. 125, 2025.

[38] X. Xin, A. M. Saeed, F. A. M. Al-Yarimi, V. Puneeth, and S. S. Narayan, "The flow analysis of Williamson nanofluid considering the Thompson and

Troian slip conditions at the boundary," *Numerical Heat Transfer, Part A: Applications*, vol. 85, no. 12, pp. 1937–1953, 2024.